



Czech Technical University in Prague
Faculty of Nuclear Sciences and
Physical Engineering

Neural network-based generative models for anomaly detection

Dissertation



Author: Ing. Vít škvára
Academic year: Year

Poděkování:

Děkuji.

Čestné prohlášení:

Prohlašuji na tomto místě, že jsem předloženou práci vypracoval samostatně, a že jsem uvedl veškerou použitou literaturu.

V Praze dne Date

.....
Ing. Vít škvára

Název: Generativní neuronové sítě pro detekci anomálií

Autor: Ing. Vít škvára

Obor: Matematické inženýrství

Druh práce: Disertační práce

Školitel: doc. Ing. Václav Šmíd, Ph.D.

Školitel specialisty: Ing. Jakub Seidl, Ph.D.

Abstrakt: Tématem této práce je detekce anomálií pomocí hlubokých generativních modelů. Čtenář je nejprve seznámen se základními koncepty a technikami, které se používají k řešení problémů detekce anomálií. Poté je představen podrobný přehled generativních modelů a jejich aplikace v detekci anomálií. Vybrané generativní modely jsou spolu srovnány v rozsáhlé experimentální části, která si klade za cíl identifikovat jejich síly a slabiny. Na základě teoretických a praktických poznatků, získaných v předchozích kapitolách, je poté představen vlastní generativní model určený pro detekci sémantických anomálií v komplexních obrazových datech. Hlavní motivací určující architekturu modelu je skutečnost, že anomálie mohou pocházet z různých zdrojů a může být více důvodů, proč je vzorek považován za anomální. Tím se navrhovaný přístup liší od podobných modelů, které tuto skutečnost nezohledňují. Model rozkládá obraz na tři nezávislé složky - tvar objektu a texturu jeho popředí a pozadí - a poskytuje pro každou z těchto složek anomální skóre. Tyto skóre lze použít k identifikaci zdroje anomálie v obraze přímo, nebo mohou být kombinována pomocí vah získaných z několika označených vzorků anomálií.

Klíčová slova: neuronové sítě, generativní modely, detekce anomálií

Title: **Neural-network-based generative models for anomaly detection**

Abstract: The topic of this thesis is anomaly detection with deep generative models. The reader is first introduced to basic concepts and techniques that are used to solve anomaly detection problems. Then, a comprehensive overview of generative models and their application in anomaly detection is presented together with a large-scale experimental survey that aims to identify their strengths and weaknesses. Armed with the obtained theoretical and practical knowledge, a novel generative model is introduced whose application domain is detection of semantic anomalies in complex image data. The motivation for the model comes from the fact that anomalies might come from multiple sources and there might be many reasons for a sample to be deemed anomalous, while most novel anomaly detection methods do not consider this. The proposed model decomposes the image into three independent components—the shape of an object and its foreground and background textures—and provides anomaly scores for each of those components separately. The scores are used to identify the source of anomaly in an image in a completely unsupervised manner or they can be combined using weights obtained from a few labeled samples of anomalies.

Keywords: neural networks, generative models, anomaly detection

Contents

1	Introduction	1
1.1	What is anomaly detection?	2
1.2	Anomaly types	3
1.3	Objectives	4
2	State-of-the-art overview	7
2.1	Comparing anomaly detectors	7
2.2	Anomaly detectors taxonomy	10
2.2.1	Probabilistic methods	10
2.2.2	Distance-based methods	13
2.2.3	Domain-based methods	15
2.2.4	Reconstruction-based methods	18
3	Generative models in anomaly detection	21
3.1	GAN-based models	22
3.1.1	Basic GAN model	22
3.1.2	GANs in anomaly detection	24
3.2	VAE-based models	25
3.2.1	Basic VAE	26
3.2.2	Wasserstein and adversarial autoencoders	32
3.2.3	Generative autoencoders in anomaly detection	35
3.3	Normalizing flows	38
3.4	Anomaly detection with generative models: practical example	40
3.4.1	The application problem	40
3.4.2	The experimental setup	42
3.4.3	Results	43
4	Empirical comparison of anomaly detectors	47
4.1	Anomaly Detection Contexts	48
4.2	Experimental setup	49
4.2.1	Data	49
4.2.2	Models and their hyperparameters	50
4.3	Experimental results	51
4.3.1	Dataset context	51
4.3.2	Hyperparameter selection context	53
4.3.3	Economic context	57
4.4	Conclusion	59

Contents

5 Anomaly detection in multi-factor data	61
5.1 Introduction	61
5.2 Decomposing the anomaly score	62
5.2.1 Orthogonal generative model	62
5.2.2 Anomaly in the latent space	63
5.3 Shape-guided decomposition	64
5.3.1 Shape-guided VAEGAN model	66
5.3.2 Detecting anomalies with SGVAEGAN	69
5.3.3 Anomaly factor identification	73
5.4 Experiments	74
5.4.1 Baseline methods	74
5.4.2 The contribution of the Jacobian	75
5.4.3 Detection of semantic anomalies	75
5.4.4 Anomaly factor identification	77
5.4.5 Large scale study	78
5.5 Conclusion	81
6 Conclusion	83
6.1 Contributions	83
6.2 Future work	84
Apendices	85
A Mathematical formulations	87
A.1 Multivariate normal distribution	87
A.2 The Kullback-Leibler divergence	87
A.3 Kullback–Leibler divergence of two normal distributions	88
B Datasets	89
B.1 Tabular datasets	89
B.2 Image datasets	89
C Additional resources	95
Bibliography	97

Introduction

Anomaly detection is an important task in environments where we have a good knowledge of what normal behaviour is, but we know very little about the behaviour of yet unseen or otherwise abnormal events – anomalies. The reasons for this can be numerous: either there is no common generating principle behind anomalies and each new anomaly may be very different from those that we have yet seen, or the acquisition of anomalous data is too expensive or downright impossible. An example of this might be an industrial process, where an anomaly incurs a high operational cost. Usually, there is a disbalance in the number of labeled normal and anomalous data samples that are available, and sometimes no anomalies are available at all. While it might be tempting to solve anomaly detection as supervised binary classification, for the reasons listed above, a supervised classifier is likely to be unrobust to actual anomalies that it will encounter in a production environment. Together with an ever-increasing volume of collected data and available computing power, this motivates the development of specialized methods for automatic anomaly detection. What these methods have in common is that they learn a model of normal data, and detect anomalies as deviations from this model.

The actions taken after an anomaly is detected might be varied. Sometimes, the anomaly might be considered to be an erroneous measurement and, as such, is ignored, which is the case of some of the earliest scientific essays [1, 2] on the topic of anomaly detection. In other cases, a preventive measure must be taken in order to mitigate unwanted behaviour, such as the case of cybersecurity [3, 4, 5], fraud detection [6, 7, 8], medical diagnosis [9, 10, 11, 12] or industrial process monitoring [13, 14, 15]. Finally, detected anomalies might drive forward scientific discovery in astronomy [16], plasma physics [17], chemistry [18] or particle physics [19].

There are countless models and algorithms for anomaly detection, tackling the problem from different angles based on the basic principle of the algorithm, the expected nature of the data, and the application domain. There are methods based on random forests [20], the k-nearest neighbors algorithm [21], Gaussian mixture models [22], clustering neural networks [23], histogram estimation [24], kernel density estimates [25] or support vector machines [26]. A comprehensive overview of anomaly detection methods is presented in studies such as [27, 28, 29, 30, 31] where the methods and their performance are usually compared on a set of benchmark datasets. Our own overview of some classical anomaly detectors follows in Chapter 2.

Deep generative models have recently attracted a lot of attention due to their ability to produce (generate) very high-quality artificial images that resemble those from the training dataset. Since the seminal papers [32, 33, 34] on the main types of gener-

1.1 What is anomaly detection?

ative models have been published, a myriad of improvements and tweaks have been proposed. While the original purpose of generative models was not aimed towards anomaly detection, some of them were redesigned for it. Most of the comparative studies of anomaly detectors however do not include methods based on (deep) neural networks and especially not generative models. The probably most recent and complete overview of deep generative models can be found at [35]. This text intends to collect some (but certainly not all) of the relevant information on deep generative models in one place and assess the potential suitability of the different generative models to the task of anomaly detection, mainly in Chapter 3. This is followed by a comprehensive experimental comparison in Chapter 4. Finally, in Chapter 5 we introduce our own anomaly detector based on generative models.

1.1 What is anomaly detection?

Anomaly detection has been extensively studied under many different names: outlier detection [36, 37], novelty detection [27], one-class classification [38] or out-of-distribution detection [39]. There is a small distinction between these terms based on the application domain, but the methods used to solve the problems they present are in principle the same. In the same vein, the terms outlier, novelty, and anomaly may have slightly different meanings in some publications, but they are often used interchangeably. In this text, we will resort to the use of the last term. An often cited definition of what constitutes an anomaly is “an observation which deviates so much from other observations as to arouse suspicion that it was generated by a different mechanism” [40]. This broad statement highlights the fact that anomalies may have very different sources of origin, and their anomality depends on the context in which they are considered.

The probabilistic definition assumes a probability distribution P^+ of normal data, operating on a data space \mathcal{X} , which is defined by a given problem, and which is most of the time only known through a set of normal samples. We call a sample $\mathbf{x} \in \mathcal{X}$ to be an **anomaly** if it lies in a region where P^+ has very low density. In other words, we can define a **set of anomalies** [35] as

$$\mathcal{A} = \{\mathbf{x} \in \mathcal{X} | p^+(\mathbf{x}) \leq \tau\}, \tau \geq 0, \quad (1.1)$$

where p^+ is the probability density function corresponding to P^+ and τ is a **threshold** which defines the line between normal and anomalous samples.

It is also often assumed that the region of data space that is occupied by normal data is concentrated, that is, there exists a threshold $\tau \geq 0$ such that

$$\mathcal{X}/\mathcal{A} = \{\mathbf{x} \in \mathcal{X} | p^+(\mathbf{x}) > \tau\} \quad (1.2)$$

is not empty, which however does not imply that the support of p^+ is bounded. On the other hand, \mathcal{A} is not required to be concentrated and can be unbounded. Notice that we do not explicitly define any sort of anomalous distribution P^- . This is because most anomaly detection methods only model P^+ . When P^- is considered, such as in KDE [41] or OCSVM [26] detectors, it is assumed that it is uniform over \mathcal{X} .

Since the full form of P^+ is usually unknown, one has to estimate it from data. The most straightforward way of expressing the anomaly detection objective is the estimation of low-density regions of the data space \mathcal{X} under P^+ . This is formalized as

density level set estimation [42], where a density set is $C = \{\mathbf{x} \in \mathcal{X} | p^+(\mathbf{x}) > \tau\}$ for some threshold $\tau \geq 0$. Then, the α -level density set C_α is (for $\alpha \in [0, 1]$) defined [35] as

$$\begin{aligned} C_\alpha &= \arg \inf_C \{\lambda(C) | P^+(C) \geq 1 - \alpha\} \\ &= \{\mathbf{x} \in \mathcal{X} | p^+(\mathbf{x}) > \tau_\alpha\}, \end{aligned} \quad (1.3)$$

which is the smallest density level set with probability at least $1 - \alpha$ under P^+ , where $\tau_\alpha \geq 0$ is the corresponding threshold and λ is a Lebesgue measure. If the concentration assumption (1.2) holds, then C_α exists for any admissible α and is bounded. For density-based sets, the task of finding (1.3) is equal to the minimum volume set estimation [43], which is a concept native to many anomaly detectors, mainly domain-based, which are described in Sec. 2.2.3.

We define the **contamination rate** of a dataset $X = \{\mathbf{x}_1, \mathbf{x}_2, \dots, \mathbf{x}_n\} \subset \mathcal{X}$, which is a finite collection of samples from data space \mathcal{X} as

$$c_r(\mathcal{X}) = \frac{|\{\mathbf{x}_i | \mathbf{x}_i \in \mathcal{A} \wedge \mathbf{x}_i \in X\}_{i=1}^n|}{|X|}, \quad (1.4)$$

i.e. the ratio of the number of anomalies to the total size of the dataset. This will be useful in later parts of this text.

We can think of any anomaly detection model as providing a function that produces a ranking of the individual data points with respect to their anomalousness. This is called an **anomaly score** $s : \mathcal{X} \rightarrow \mathbb{R}$ of a model. In certain contexts [44], anomaly score might be called *decision* or *scoring function*. In this text, we will assume that a higher anomaly score is attributed to a point more likely to be anomalous. To be able to use an anomaly score for decision-making, one must choose the threshold $\tau \in \mathbb{R}$. From (1.1), a sample \mathbf{x} is considered to be an anomaly if $s(\mathbf{x}) \geq \tau$ and normal otherwise. The selection of τ can sometimes be a process more complicated than the fitting of the actual model [45]. Its value is typically determined based on the tolerated false positive rate and an estimate of the true contamination rate of a dataset (1.4).

1.2 Anomaly types

Different types of anomalies that require different approaches have been identified in literature [30, 35]. Examples for each type are presented in Fig. 1.1.

- **Point anomaly** is a single observation from \mathcal{A} , for example, an outlying measurement or a photograph of a cat among other images of dogs. This is the most often studied type of anomaly in the research literature. Note that a point anomaly can become an anomaly of the two following types if the observations in a dataset are somehow dependent (e.g. through time) or if some additional context about the data can be extracted.
- **Group anomaly** is a collection of correlated observations that are only anomalous together. Only a large number of malicious requests is enough to shut down a server in a DDoS attack [46]. Other research [47, 48] focuses on finding anomalies under the multiple-instance learning (MIL) [49] paradigm, where individual observations (called bags) are comprised of a variable number of multivariate measurements (called instances). This calls for an aggregation method, on top of which an anomaly detector can operate.

1.3 Objectives

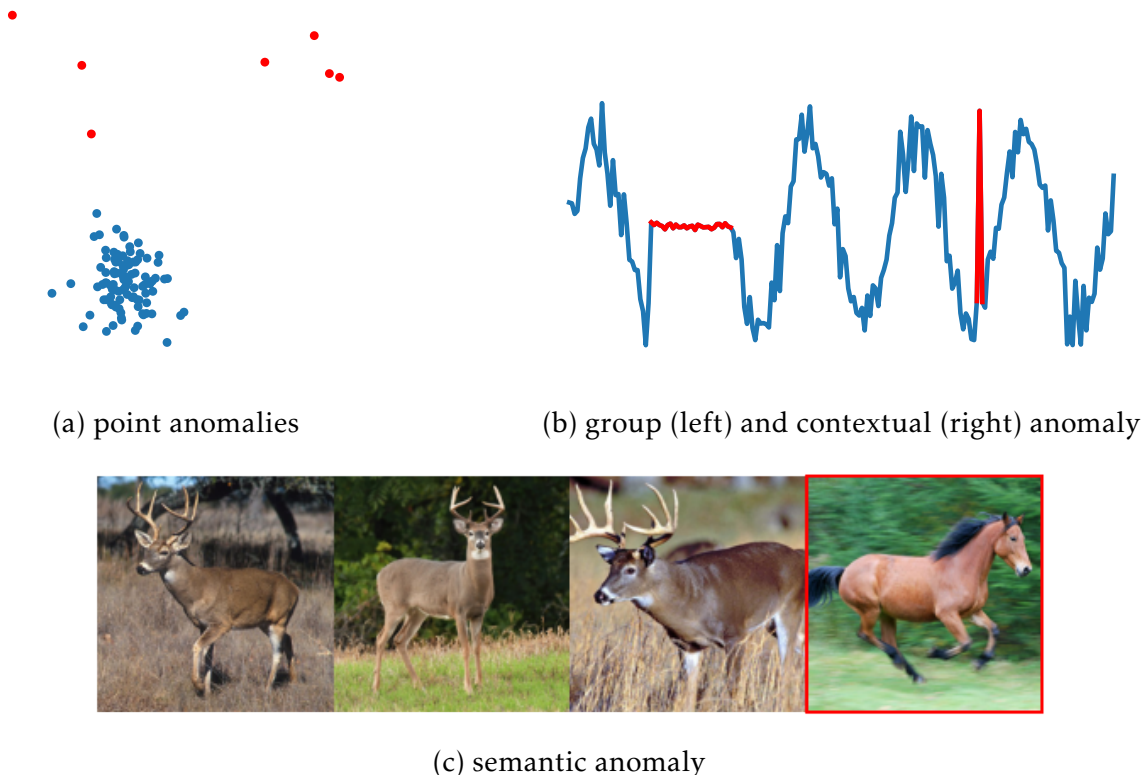


Figure 1.1: Examples of different types of anomalies.

- **Contextual** anomaly is a kind of anomaly that is only anomalous in a certain context. A person measuring over 195 cm is an outlier in almost any place except a locker room of a basketball team. If a target dataset consists of pictures of birds photographed mid-flight – is a bird sitting on grass an anomaly? Or a different flying object, such as an airplane? The answers to those questions depend on what problem is actually being solved. Contextual anomalies often arise in time series [50] or in spatial data [51].
 - **Semantic** anomalies arise in image data and are opposed to **sensory** anomalies. While sensory anomalies appear in low-level image features such as edges or textures (e.g. breaks or defects), semantic anomalies can be detected in the high-level information of an image (e.g. an object of a different category than what appears in the training dataset). Semantic anomalies can be hard to detect, as they can be very similar to normal data [52]. We will cover their detection in chapters 4 and 5.

1.3 Objectives

In this short section, we summarize the objectives and goals of this thesis. The logical structure of the text follows them, as each objective is covered by one or more chapters. The main objectives are the following:

1. Providing a compilation of the current state-of-the-art for both classical (shallow) models and (deep) generative models for anomaly detection. This is important

in order to understand the theoretical properties of current shallow and deep methods. Also, by compiling all this information in one place (Chapters 2 and 3), this work can then serve as an introduction to the topic of anomaly detection as well as to generative modelling, while at the same time providing deeper insights into the behaviour of generative models in anomaly detection, which most of the current surveys are lacking.

2. Conducting an extensive experimental comparison of selected methods under different operating conditions. This is done in Chapter 4, and it is meant to test the strengths and weaknesses of the individual methods in a broad range of conditions, such as varying data type, anomaly type, and amount of anomalies in the validation set. The desired outcome of such an analysis is providing a direction in which deep generative models can bring added value, either in performance, explainability, or other areas.
3. Finally, based on the knowledge gained in the course of the work, the main goal is to propose a novel anomaly detector based on deep generative models. To validate that it solves the specific anomaly detection problem for which it is designed, an experimental comparison needs to be conducted again, see Chapter 5.

2

State-of-the-art overview

In this chapter, we first introduce basic measures that are used for comparison of anomaly detectors. Then, we describe the current stat-of-the-art of anomaly detectors that are not based on generative models, since those are described in Chapter 3.

2.1 Comparing anomaly detectors

Comparing different models on the same set of data is a basic requirement in practical and research problems. As already mentioned at the beginning of the previous chapter, anomaly detection has some common ground with binary classification tasks. Therefore, we can readily apply the evaluation metrics that are used to evaluate these tasks in comparisons of anomaly detectors. However, there are specifics of anomaly detection problems, mainly the often encountered large imbalance of labeled normal and anomalous samples, that we have to keep in mind. Also, with one exception, all the metrics that will be described here require at least some labeled anomalous samples, no matter how difficult it might be to obtain them. A more complete overview with some experimental results can be found in [53].

Table 2.1 displays a confusion table that introduces the basic concepts and notation needed below. It summarizes the performance of an algorithm with a particular threshold. In the context of anomaly detection, positive samples are anomalies, while normal samples are considered negative.

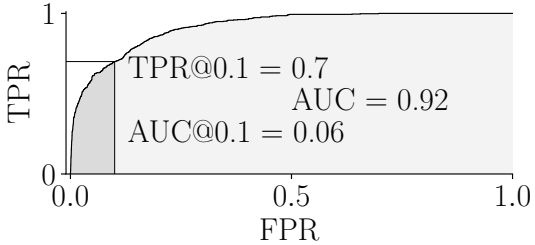
AUC

The most widely used measure in the field of anomaly detection is the area under the ROC (receiver operating characteristic) curve. The acronym AUC will be used in this text for the sake of brevity. The ROC curve is a parametric curve describing the trade-off between **true positive rate** (sometimes also called **recall**) $TPR(\tau) = \frac{tp}{tp+fn}(\tau)$ and

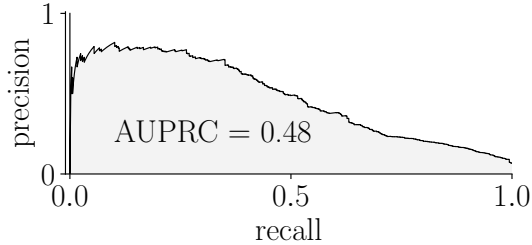
true label/estimated label	normal	anomalous
normal	tn	fp
anomalous	fn	tp

Table 2.1: A confusion matrix of a model which captures its performance by showing the total number of correctly (tp = true positives and tn = true negative) and incorrectly (fp = false positives and fn = false negatives) identified samples.

2.1 Comparing anomaly detectors



(a) ROC curve



(b) PR curve

Figure 2.1: An example of a ROC curve and the derived measures captured at FPR=0.1. AUC is the whole shaded area under the ROC curve. The darker shading corresponds to AUC@0.1. On the left, the PR curve of the same detector is shown.

false positive rate $\text{FPR}(\tau) = \frac{\text{fp}}{\text{fp} + \text{tn}}(\tau)$ for different values of the decision threshold τ .

Then, the area under the curve is calculated as the following integral

$$\text{AUC} = \int_{\mathbb{R}} \text{TPR}(\tau) d\text{FPR}'(\tau) d\tau = \int_0^1 \text{TPR}(\text{FPR}) d\text{FPR}. \quad (2.1)$$

The last integral that uses $\text{TPR}(\cdot)$ as a function of the corresponding FPR shows the simple concept behind the AUC that can be easily discerned from a ROC curve drawn in a graph, see Fig. 2.1. An AUC value of 1.0 is equal to perfect classification/ordering of the data, while a value of 0.5 is equal to classifying by random guessing. In practice, the corresponding AUC is estimated from an empirical ROC curve using some numerical integration scheme, e.g. the trapezoidal rule.

As mentioned above, the main advantage of AUC is that it does not depend on the choice of a particular decision threshold. Also, the measure has a straightforward interpretation – it is an estimate of the probability that a randomly chosen positive sample is ranked higher than a randomly chosen negative sample [54]. However, a lot of information is lost when the whole ROC curve is summarized into a single number. This is especially concerning for some applications, where the region of low false positive rates is of the principal interest. For example, in cybersecurity applications, it is usual to draw a ROC curve in logarithmic scale on the x-axis, which accentuates the low-FPR section of the ROC curve.

AUPRC

The Area Under the Precision-Recall Curve is very similar to AUC, as it is given by computing the **precision** $\text{PREC}(\tau) = \frac{\text{tp}}{\text{tp} + \text{fp}}(\tau)$ and recall for different values of classification threshold τ and then integrating the area under the resulting curve. Although popular in some contexts, it has its drawbacks. A PR curve has at most as many unique recall values as positive samples in the dataset. This is problematic for anomaly detection, where the number of anomalies is low, which leads to a very sparse estimate of the true PR curve. In fact, using the same trained anomaly detector and changing the contamination rate of a testing dataset produces highly varied AUPRC results, which then makes any analysis based on AUPRC useless when the true contamination rate is unknown. Furthermore, a correct PR curve lacks a universal starting point, unlike a ROC curve, because precision is undefined for zero recall, making the computation and normalization of the area under the PR curve and the comparison between datasets

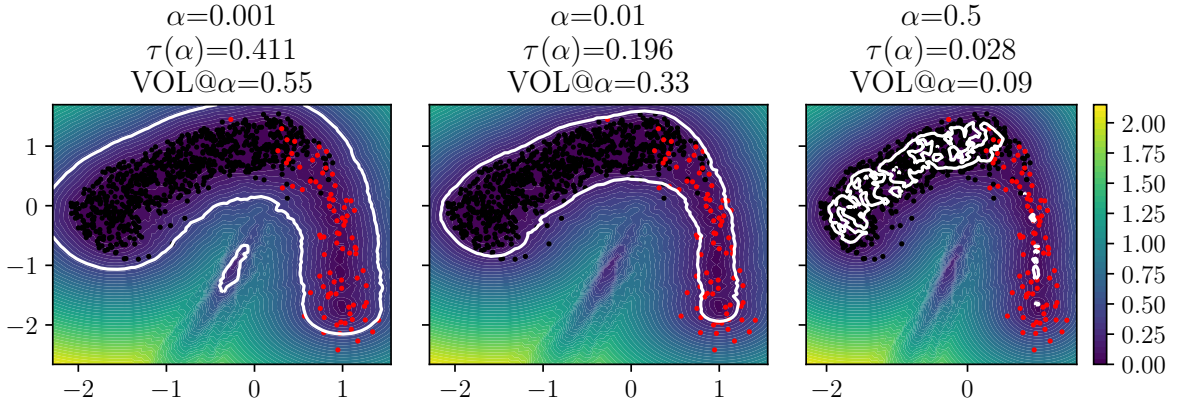


Figure 2.2: An example of a detector and the decision region for differing values of FPR α . The decision boundary is drawn as a white isoline at level $\tau(\alpha)$ with the estimated enclosed volume $\text{VOL}@\alpha$, black and red dots represent normal and anomalous samples in the training set. Clearly, a smaller tolerance of false positives forces us to set a higher threshold which results in higher decision region volume.

even more complicated. Nevertheless, it is a metric that is reported very often besides the AUC.

Areas of low TPR

The two already mentioned metrics put the same weight on all areas on the x-axis. This might not be always ideal for the purpose of anomaly detection, as low FPR areas might be more interesting – after all, when reporting detected anomalies for a manual check, there is always a limit on how many samples can be realistically processed. A performance measure popular among practitioners is **TPR@ α** , which is simply the true positive rate evaluated at a given false positive rate $\alpha \in [0, 1]$. This measure can be easily read from an ROC curve. In practice, it is necessary to interpolate the ROC curve since it has discrete values, especially for datasets with a small number of samples.

Another alternative to AUC is the partial AUC, or **AUC@ α** , which is the area under the ROC curve calculated only up to some value of false positive rate $\alpha \in [0, 1]$

$$\text{AUC}@\alpha = \int_0^\alpha \text{TPR}(\text{FPR}) d\text{FPR}. \quad (2.2)$$

Numerically, it is again important to interpolate the ROC curve for a given α before computing the integral. In Fig. 2.1, AUC@0.1 corresponds to the darker gray region. AUC@ α can be easily normalized by dividing by the chosen α , in which case the best detector has $\text{AUC}@\alpha = 1$ similarly to AUC.

Volume of decision region

All of the previous measures originate from the evaluation of the performance of binary classifiers. Since labeled anomalies are often difficult to obtain, a measure that does not require labels for its evaluation might be more useful and better describe behaviour on unknown samples. If the goal is to compare two models supposed to

2.2 Anomaly detectors taxonomy

characterize the normal class, and with no other assumptions about the distribution of the anomalous class, it makes sense to choose the model enclosing the training data more tightly. This corresponds to calculating the volume inside the model's decision boundary in a similar fashion to [55], where a theoretical justification is given. This decision boundary can be chosen to correspond to a certain level of false positive rate. We define the **volume of decision region** as

$$\text{VOL}(\alpha) = \int_{\mathcal{X}} \mathbb{1}_{\{\mathbf{x} \in \mathcal{X} | s(\mathbf{x}) \leq \tau\}}(\mathbf{x}) d\mathbf{x} \text{ s.t. } \text{FPR}(\tau) = \alpha, \quad (2.3)$$

where \mathcal{X} is the input space, $s(\mathbf{x})$ is an anomaly score, and $\alpha \in [0, 1]$ is a given false positive rate. In other words, $\text{VOL}(\alpha)$ is the volume of the subspace where the classifier returns "normal" answer with a false positive rate α . An example of a model and its decision region for different values of α is shown in Fig. 2.2. It should be noted that the idea of minimizing the enclosed volume is native to some models, e.g. the SVDD model described in Sec. 2.2.3.

Computing the empirical $\text{VOL}(\alpha)$ in data space \mathcal{X} requires first finding the threshold τ corresponding to the chosen FPR α and then integrating the volume which corresponds to the space enclosed by the isosurface where the anomaly score is equal to τ . It is numerically estimated by Monte Carlo sampling [56]. This comes with its downsides. Mainly, the number of samples required to cover d -dimensional sample space grows exponentially with d . This issue has been addressed in [57], where the volume is computed multiple times for different subsamplings of input features, however, this does not seem to be optimal as it requires training a new model for each subset of features. A comprehensive description of the practical use of this measure is presented in the original publication [53].

2.2 Anomaly detectors taxonomy

Anomaly detection methods are based on a wide range of paradigms. In this section, we will follow the taxonomy outlined in publications [27, 35], which divide shallow (not based on neural networks) and deep (based on neural networks) detectors into groups based on their common traits. Note that this taxonomy is tentative, and some methods have traits common to multiple groups. A few examples of the most prominent methods will be given for each category, since their knowledge will be useful in the later chapters of this text, but the list is far from complete. For a complete overview of the landscape of anomaly detection methods, see the surveys [27, 31, 28, 58, 59, 60, 61, 62, 35].

2.2.1 Probabilistic methods

Since we have defined anomaly detection as detecting samples that deviate from the normal distribution P^+ , it is straightforward to try to model the distribution by modeling its probability distribution function (pdf). One of the simplest such methods is the Grubbs' test [63], which assumes a Gaussian distribution of normal one-dimensional data and declares a sample to be anomalous if its distance from the mean is larger than some threshold (e.g. three standard deviations). Many such methods based on statistical tests have been proposed [64], but we will focus on advanced modeling probabilistic techniques.

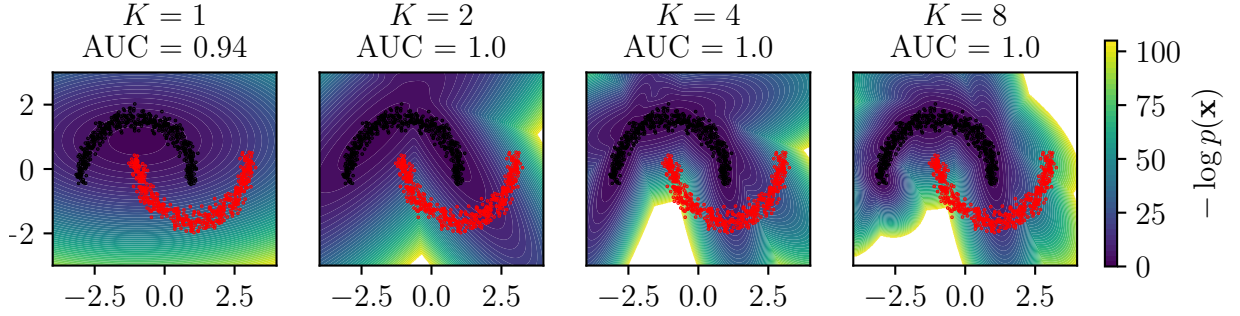


Figure 2.3: The *two bananas* dataset consists of two clusters of points. The black points are considered to be normal and the red are considered to be anomalies. The dataset is useful for introducing behaviour of anomaly detectors because as an anomaly detection problem, it cannot be solved by a linear separation of the two groups of points. Here, GMM models with a varying number of components K are fitted to the normal observations. The contours of the anomaly score based on (2.5) are shown together with the AUC computed with respect to the anomalous observations.

Shallow methods

A **Mahalanobis distance** anomaly detector [65] is a step-up from the naive Grubbs' test as it assumes that the normal data have a multivariate Gaussian distribution. Therefore, it builds a simple parametric estimate of the normal distribution by computing the mean $\boldsymbol{\mu} \in \mathbb{R}^d$ and covariance matrix $\Sigma \in \mathbb{R}^{d \times d}$ of the training data. The anomaly score of a test point $\mathbf{x} \in \mathbb{R}^d$ is then

$$s(\mathbf{x}) = (\mathbf{x} - \boldsymbol{\mu})^T \Sigma^{-1} (\mathbf{x} - \boldsymbol{\mu}), \quad (2.4)$$

which is equivalent to the evaluation of the negative log-likelihood under the Gaussian distribution. Even though this is one of the simplest and most non-robust methods, we include it here since terms similar to (2.4) will be encountered in the remainder of this text.

Instead of limiting the model to a single-mode distribution, a mixture of K distributions

$$p(\mathbf{x}) = \sum_{k=1}^K p(k)p(\mathbf{x}|k), p(k) \in [0, 1], \sum_{k=1}^K p(k) = 1, \quad (2.5)$$

can be estimated instead, where $p(k)$ is the prior probability of the k -th component. **Gaussian Mixture Models** (GMMs) have been used for anomaly detection in [66, 22]. There, we assume that $p(\mathbf{x}|k)$ are Gaussian distribution densities, and their parameters are estimated using the EM algorithm [67] or via Variational Bayes [68]. The expression $-\log p(\mathbf{x})$ is usually used as the anomaly score, although sometimes the maximum of the Mahalanobis distance (2.4) over the K components is used instead. However, the viable usecases for a GMM anomaly detector are limited, mainly due to the need to compute and invert the covariance matrix, which is $O(d^3)$ in the size of the input space d (when the full covariance matrix is estimated). See Fig. 2.3, where the same anomaly detection problem is solved by GMMs with a different number of components. Even

2.2 Anomaly detectors taxonomy

though the AUC score is already perfect for two components, the difficult shape of the normal data requires more components than that to be fully covered.

Time series data anomaly detection was approached with the use of **Autoregressive Integrated Moving Average** (ARIMA) models in [66, 69], or using a **Hidden Markov Model** (HMM) in [70, 71]. Both approaches offer predictions for future states of an observed system, and the anomaly score is the difference between the prediction and the actual state of the system. The problems to which these methods can be applied are encountered in medicine or computer network intrusion detection.

All the previous were examples of parametric models, where a set of parameters θ is directly estimated. Opposed to these are non-parametric models, which are less restricting – e.g. they do not assume any (normal, Poisson, ...) distribution – instead, they build a parameter-free model of the normal data. **Kernel density estimation** (KDE) method [41], which estimates an unknown univariate probability density function by an empirical estimate

$$\hat{p}(x) = \frac{1}{hn} \sum_{i=1}^n k_f\left(\frac{x-x_i}{h}\right), x_i \in X \quad (2.6)$$

where $X = \{x_1, x_2, \dots, x_n\} \subset \mathbb{R}$ is the training dataset of n univariate samples, $h \in \mathbb{R}^+$ is a bandwidth parameter, and $k_f : \mathbb{R} \rightarrow \mathbb{R}^+$ is a **kernel** – uniform, triangular, normal (which is the most often used), etc., see [72]. Note that this is different from kernel functions used and described in Sec. 2.2.3. KDE has been used under the name Parzen window estimate e.g. in [9, 73], where $-\ln \hat{p}(x)$ is used to score anomalies. **Histogram-based Outlier Score** (HBOS) is a method [74] for anomaly detection on multivariate data $\mathbf{x} \in \mathbb{R}^d$. It computes normalized histograms for each feature $x_j, j \in \{1, \dots, d\}$ independently. Then the anomaly score for an unlabeled sample \mathbf{x} is

$$s(\mathbf{x}) = - \sum_{j=1}^d \ln \tilde{p}_j(\mathbf{x}) \quad (2.7)$$

where $\tilde{p}_j(\mathbf{x})$ is the height of the bin in which x_j is located. The main advantage of this method in comparison with e.g. distance-based is the relative computational simplicity. In the **Lightweight Online Detector of Anomalies** (LODA) [24], an ensemble of one-dimensional histograms is used in the space of diversified projection vectors. The anomaly score is then an average of the logarithm of probabilities estimated from the histograms on individual projection vectors. Due to its simplicity and computational efficiency, it is popular in settings with high volumes of data and potentially missing input values.

Deep methods

The recent advent of neural networks has given rise to many novel methods that are more capable of handling high-dimensional datasets that would be otherwise extremely difficult to handle. A mixture model was used in the **DAGMM** method [75], where a neural network creates a low-dimensional latent representation \mathbf{z} from an input \mathbf{x} . The GMM and its parameters are then estimated in the latent space, again via a neural network, which enables online learning of the whole model together.

Energy based models (EBMs) use the energy function $E_\theta(\mathbf{x})$ to approximate the density as

$$p_\theta(\mathbf{x}) = \frac{1}{Z(\theta)} \exp(-E_\theta(\mathbf{x})), \quad (2.8)$$

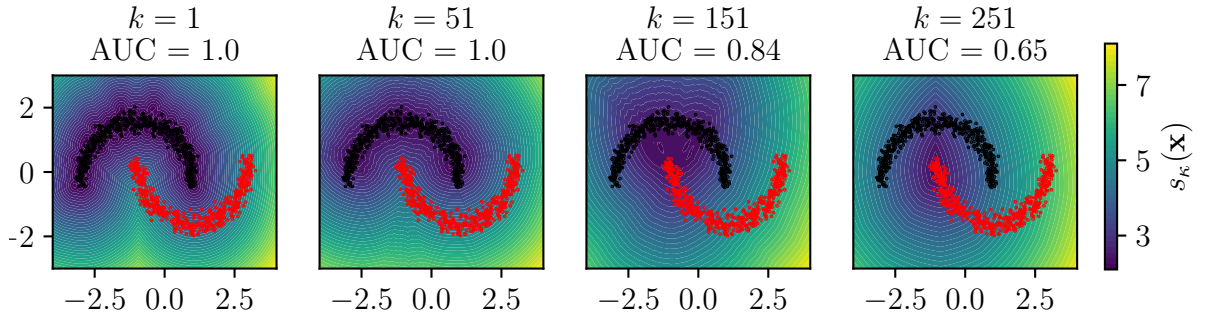


Figure 2.4: K-nearest neighbor detectors on the *two bananas dataset*. The contours of the score (2.9) are shown for different values of k together with the resulting AUC.

where $Z(\boldsymbol{\theta})$ is the partition function parametrized by $\boldsymbol{\theta}$ to ensure proper normalization of $p_{\boldsymbol{\theta}}(\mathbf{x})$. Although the partition function usually cannot be directly computed, an EBM can still be trained via gradient descent coupled with Markov Chain Monte Carlo estimation [76], which is however also the reason for its ineffectiveness relative to more novel approaches, as the MCMC is computationally costly. The anomaly score is then the energy function $E_{\boldsymbol{\theta}}(\mathbf{x})$. Although the direct use of the early examples of EBMs such as **Deep Belief Networks** [77] and **Deep Boltzmann Machines** [78] was impractical for anomaly detection, they were eventually refined and successfully used on anomaly detection benchmarks in [79].

Finally, the most recent advancements in anomaly detection were achieved with the use of deep generative models that model the distribution of the data via a generative process, where it is assumed that the data is generated from a hidden latent variable. **Flow models** [34], **Variational autoencoders** [33] and **Generative Adversarial Networks** [32] are described in greater detail in Chapter 3.

2.2.2 Distance-based methods

Instead of modeling the probability distribution of the normal data, distance-based anomaly detectors use heuristics that compute a similarity measure between two data points. One of the simplest such models is the **k-Nearest Neighbor** (kNN) [80] model where the anomaly score of a sample is based on its proximity to its k -nearest neighbours from the training dataset. Consider set $X_k(\mathbf{x})$ of the k -nearest neighbors of \mathbf{x} from a training dataset $X = \{\mathbf{x}_1, \mathbf{x}_2, \dots, \mathbf{x}_n\} \subset \mathbb{R}^d$. Different anomaly scores are then described in [21], where the Euclidean distance is used as the similarity measure:

- $s_k(\mathbf{x})$, where the anomaly score is the distance between \mathbf{x} and its k th-nearest neighbor,

$$s_k(\mathbf{x}) = \max_{\mathbf{x}_i \in X_k(\mathbf{x})} \|\mathbf{x} - \mathbf{x}_i\|_2, \quad (2.9)$$

- $s_\gamma(\mathbf{x})$, where the anomaly score is the average distance of \mathbf{x} to its k -nearest neighbors,

$$s_\gamma(\mathbf{x}) = \frac{1}{k} \sum_{\mathbf{x}_i \in X_k(\mathbf{x})} \|\mathbf{x} - \mathbf{x}_i\|_2, \quad (2.10)$$

2.2 Anomaly detectors taxonomy

- $s_\delta(\mathbf{x})$, where the anomaly score is the length of the mean of the vectors pointing from \mathbf{x} to its k -nearest neighbours,

$$s_\delta(\mathbf{x}) = \left\| \frac{1}{k} \sum_{\mathbf{x}_i \in X_k(\mathbf{x})} (\mathbf{x}_i - \mathbf{x}) \right\|_2. \quad (2.11)$$

All these definitions presume that normal data lie in concentrated regions of the data space \mathcal{X} , according to (1.2), while anomalies lie outside of them. The kNN anomaly detector is very popular thanks to its simplicity and good performance [31]. See Fig. 2.4, where low values of k result in a very local behaviour of the model, which is suitable for this problem. The biggest disadvantage of the model is the computational cost. Even though there is no actual training procedure, the prediction complexity is $O(ndk)$. This can be ameliorated by the construction of a k -d tree [81], which partitions the space of the training data to speed-up prediction, or using GPU-based similarity search techniques such as [82]. Other methods, such as REPEN [83], use the kNN detector trained on low-dimensional representations of otherwise high-dimensional data produced by a deep neural network. We will make use of this approach in models in Sec. 3.4 and Chapter 5.

The **Local Outlier Factor** (LOF) algorithm [84] is based on comparing the local density of a sample \mathbf{x} with the local density of its k -nearest neighbours. To correctly describe the way in which the density is defined and the anomaly score is computed, we use the formula (2.9). Then we define the *local reachability density* as

$$\text{LRD}_k(\mathbf{x}) = \frac{|X_k(\mathbf{x})|}{\sum_{\mathbf{x}_i \in X_k(\mathbf{x})} \max\{s_\kappa(\mathbf{x}), \|\mathbf{x} - \mathbf{x}_i\|_2\}}. \quad (2.12)$$

Since this is practically the inverse of an average distance between \mathbf{x} and its neighbours, the closer the neighbours are to \mathbf{x} , the higher this approximation of local density is. Finally, anomaly score of \mathbf{x} is given by comparing the LRD_k of \mathbf{x} and its neighbours

$$s_{\text{LOF}}(\mathbf{x}) = \frac{\sum_{\mathbf{x}_i \in X_k(\mathbf{x})} \text{LRD}_k(\mathbf{x}_i)}{\text{LRD}_k(\mathbf{x}) |X_k(\mathbf{x})|}. \quad (2.13)$$

The rationale behind the formula is that if the local density of the neighbours is higher or the local density of \mathbf{x} is lower then it is more likely for \mathbf{x} to be an anomaly. This method however does not scale well in number of training samples, as its complexity is even greater than that of a simple kNN detector. Methods that are similar to LOF are the **connectivity-based outlier factor** (COF) [85] or **clustering-based local outlier factor** (CBLOF) [86].

A different approach is taken by the **isolation forest** (IF) model [20] where an ensemble of $N_t \in \mathbb{N}$ isolation trees is constructed from the training dataset. The individual trees are constructed in such a way as to isolate each individual observation from the rest of the dataset using consecutive splits on different features. Although this procedure is stochastic (each tree splits the data differently), it is presumed that an anomaly can be generally isolated using a smaller number of splits and therefore it usually lies on a branch closer to the root of the tree. The anomaly score is then based on the depth in which a sample is represented in the tree, averaged over all trees in the ensemble. A method similar to IF is the **Partial Identification Forest** (PIDForest) [87],

which uses a more informed way of choosing the data features for split, favouring more informative features.

In **Angle-Based Outlier Detection** (ABOD) [88] presumes that outliers lie far from clusters of normal data, therefore the viewing angle that covers a cluster of normal observations when "looking" at it from a sample \mathbf{x} is smaller when \mathbf{x} is anomalous. More concretely, the method computes the angles between \mathbf{x} and all pairs of points in the training dataset, and the anomaly score is inversely proportional to the variance of these angles – the more varied the angles are, the more likely \mathbf{x} is close to some cluster of normal data and the anomaly score is thus lower. In the original paper, the method is lauded for the lack of hyperparameters that need to be tuned and the ability to operate in high-dimensional data spaces. However, in the experiments in Chapter 4, it proves to be the method with one of the slowest prediction times.

2.2.3 Domain-based methods

Some anomaly detectors divide the data space into a normal and anomalous subspace (domain). In [35], these are labeled as domain-based, and we will follow that distinction here.

Shallow methods

In domain-based models, the data space is partitioned into subspaces by a decision boundary. Instead of estimating the density of the whole training dataset, they only consider a few samples from it, which are called **support vectors**, and which are used to define the decision boundary. A very simple example is an anomaly detector which, for a training set $X = \{\mathbf{x}_1, \mathbf{x}_2, \dots, \mathbf{x}_n\} \subset \mathbb{R}^d$, constructs a hypersphere with center $\mathbf{c} \in \mathbb{R}^d$ and radius $R > 0$ that encloses the training data. It is found by solving the objective

$$\begin{aligned} \min_{R, \mathbf{c}, \xi} & R^2 + \frac{1}{vn} \sum_{i=1}^n \xi_i \\ \text{s.t.} & \|\mathbf{x}_i - \mathbf{c}\|_2^2 \leq R^2 + \xi_i, \quad \xi_i \geq 0, \forall i \end{aligned} \quad (2.14)$$

where ξ_i are slack variables that allow some data points to lie outside of the hypersphere. The ratio of the maximum number of outliers is controlled by the variable $v \in (0, 1]$, which is at the same time a lower bound on the number of support vectors, which are samples \mathbf{x}_i that lie exactly on the boundary of the hypersphere. The solution to (2.14) is given by solving the dual problem. Notice that a simple criterion $\|\mathbf{x} - \mathbf{c}\|_2^2 \leq R^2$ already gives a decision whether the point \mathbf{x} is already inside the sphere. To convert this to a continuous anomaly score, we can compute the distance of \mathbf{x} from the boundary

$$s(\mathbf{x}) = \|\mathbf{x} - \mathbf{c}\|_2^2 - R^2 \quad (2.15)$$

which is negative for points inside and positive for points outside the hypersphere.

Abstracting the above, one can use **kernel functions** [89] to move the problem (2.14) from the original input space to a transformed kernel space. The kernel is a function $k_f : \mathbb{R}^d \times \mathbb{R}^d \rightarrow \mathbb{R}$, with which we associate a **feature map** $\Phi : \mathbb{R}^d \rightarrow \mathcal{F}_k$ such that the relation defined by the inner product $k_f(\mathbf{x}, \mathbf{y}) = \langle \Phi(\mathbf{x}), \Phi(\mathbf{y}) \rangle$ is true for all \mathbf{x}, \mathbf{y} . The space \mathcal{F}_k is a reproducing kernel Hilbert space and we choose the kernel in such a way that

2.2 Anomaly detectors taxonomy

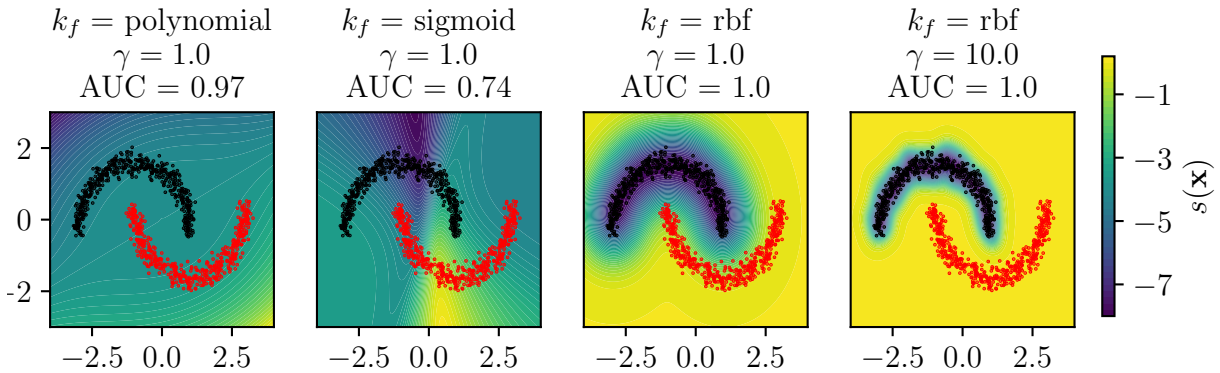


Figure 2.5: OCSVM detectors with different kernel functions and kernel width parameter γ values on the *two bananas* dataset. The contours of the score (2.15) together with the resulting AUC are depicted. Although the use of both the polynomial and sigmoid kernels results in a relatively good AUC value, the anomaly score contours reveal that the model would fail if the anomalies were placed slightly differently. Furthermore, the tight fit of the training data with the *radial basis function* (rbf) is proportional to the kernel width.

its dimensionality is higher than d . This is the basis for the **Support Vector Data Descriptor** (SVDD) anomaly detector, where the inequality condition in (2.15) is replaced by $\|\Phi(\mathbf{x}_i) - \mathbf{c}\|_2^2 \leq R^2 + \xi_i$. By solving the problem in a space of higher dimensionality, it is possible to find a decision boundary (hypersphere) for observations that would otherwise not be separable in the original space. In comparison, the **One-Class Support Vector Machine** (OCSVM) [26] does not construct a hypersphere, but instead aims to find a separating hyperplane in the kernel space. See Fig. 2.5 for a demonstration of the OCSVM model on our toy dataset. Unlike in traditional SVM [90], which is used to separate two classes in a binary classification problem, OCSVM instead aims to find a hyperplane that maximizes the separation of the majority of the training data from the origin in the kernel space. The anomaly score of an OCSVM detector is, similarly to (2.15), the distance from the separating hyperplane. Apart from ν , a very important hyperparameter of the model is the kernel scale parameter γ_{OCSVM} . Many variants of both of the presented approaches were introduced over the years, such as **Minimum Volume Ellipsoid** [91], **Multi-sphere SVDD** [92] or **Bayesian Data Description** [93].

Deep methods

Instead of choosing a kernel and its parameters manually, one can instead parametrize the feature maps Φ using neural networks and train them using standard gradient descent techniques, or use pre-trained networks from related tasks. This is the basis for deep OCSVM methods such as **One-class Neural Network** (OCNN) [94] or [95], or methods based on the SVDD formulation [96]. In **Deep SVDD** (DSVDD) [38], the objective (2.14) is reformulated without the slack variables ξ_i , which means that the hypersphere is expected to enclose all observations in the training dataset. This simplification leads to faster convergence and yet still proves to be an effective anomaly detector. However, all the deep methods have a basic flaw. Without any further restrictions,

the solution $\Phi(\mathbf{x}) = \mathbf{c}$ is valid but does not provide a useful detector. This behaviour is called the *feature map collapse*. In order to prevent this, many techniques such as freezing the neural networks that provide the feature map, architectural choices or using adversarial learning are used (for an extensive list of possibilities, see [35]).

Training with negative examples

Although we have stated in Sec. 1.1 that anomaly detection methods do not usually consider the distribution of anomalies P^- , some approaches do. These still fall under the domain-based category of anomaly detectors, as they are mostly constructed as binary classifiers that divide the input space into subspaces where either the anomalous or normal class is expected. In the simplest case [97], P^- is assumed to be uniform and a supervised classifier is trained using anomalies sampled from a hypercube centered around the normal data. This approach, however, suffers from the curse of dimensionality and saturating the hypercube in high-dimensional spaces is computationally infeasible, especially for image data. Some attempts for a more efficient sampling have been proposed, such as sampling based on local density estimation [98]. In **outlier exposure** [99] techniques, a large auxiliary dataset, that is somehow related to normal data, is used to improve the generalization properties of a deep anomaly detector. For example, if the normal class consists of images of birds, it might be useful to train the detector to recognize normal data from images containing other animals, even though this auxiliary dataset may contain animal classes that will not be encountered as anomalies in a test/production environment. It has been shown to be an effective technique in [100].

Outlier exposure is a form of **weak supervision** [101], which is a more general term covering the approach to learning with imperfectly labeled anomaly samples. In [102, 103] it is shown that using even a few labeled examples of anomalies can dramatically improve the detection performance. It is however important to robustify the model in order to be able to generalize to the types of anomalies not present in the labeled training dataset. These techniques can help in **active learning** in anomaly detection [104], where the anomaly detector sends queries to its operator, asking for the most informative/relevant samples to be manually labeled. It is stated in [35] that weak supervision is essential for potential breakthroughs in anomaly detection, which is the motivation for the method proposed in Chapter 5.

Another paradigm where the model is trained in the presence of additional data is **self-supervision** [105], where the model solves an auxiliary task, such as prediction of transformations applied to the image [106]. The important distinction between this approach and outlier exposure is that the transformed data is obtained from the normal training dataset by applying random translations, scalings, rotations, etc. Transforming the data in a controlled manner, the anomaly detector is then a multiclass classifier that predicts the correct transformation applied to the data. The anomaly score of such a model is then based on the softmax activations in the output layer – if the prediction uncertainty is high, the scored sample is more likely to be an anomaly. This was very successfully used in the **Geometric Transformations** (GT) [107] anomaly detector. Furthermore, the **GOAD** method [108] extends this approach to non-image data.

2.2.4 Reconstruction-based methods

One of the most popular approaches to anomaly detection is to build a model that learns to reconstruct input samples. When this model is trained on normal data and learns to reconstruct them well, it is expected that it will be able to identify anomalies by failing to reconstruct them properly since they have properties unseen by the model at training time. To formalize this, a reconstruction-based anomaly detector consists of an *encoder*, which is a mapping $e_{\phi} : \mathcal{X} \rightarrow \mathcal{Z}$, and a *decoder* $g_{\theta} : \mathcal{Z} \rightarrow \mathcal{X}$. Here, $\mathcal{X} \subset \mathbb{R}^d$ is the input space, $\mathcal{Z} \subset \mathbb{R}^h$ is a so called *latent space* and ϕ, θ are parameters. A *latent representation* or *encoding* of a sample \mathbf{x} is $\mathbf{z} = e_{\phi}(\mathbf{x})$. Reconstruction-based methods then try to match the original sample \mathbf{x} with its reconstruction $\mathbf{x}' = g_{\theta}(\mathbf{z}) = g_{\theta}(e_{\phi}(\mathbf{x}))$. This is done by finding such parameters ϕ, θ as to minimize the reconstruction objective

$$\min_{\phi, \theta} \|\mathbf{x} - g_{\theta}(e_{\phi}(\mathbf{x}))\|_2^2 + \mathcal{R}, \quad (2.16)$$

where \mathcal{R} is a regularization term. Some sort of regularization is needed in order to prevent the decoding function $(g_{\theta} \circ e_{\phi})(\mathbf{x})$ to become an identity function, in which case the detector would be useless. The anomaly score of reconstruction-based methods is the *reconstruction error*

$$s(\mathbf{x}) = \|\mathbf{x} - g_{\theta}(e_{\phi}(\mathbf{x}))\|_2^2. \quad (2.17)$$

The **Principal Component Analysis** (PCA) [109, 110], although not originally developed for this purpose, is an example of a reconstruction anomaly detection method. It is assumed that the normal data lie on a lower-dimensional manifold in the data space, which is an assumption also used in other methods. This means that theoretically, they can be represented by a transformation into a lower dimensional latent space, and the eventual differences between the reconstructions from the latent back to the data space and the original samples are only due to noise that is present in the data, and therefore the latent representation contains all the relevant information of a sample. PCA seeks to represent the data by finding an orthonormal basis $W \in \mathbb{R}^{h,d}$ that maximizes the empirical variance of the data $X = \{\mathbf{x}_1, \mathbf{x}_2, \dots, \mathbf{x}_n\} \subset \mathbb{R}^d$. The original objective of PCA can be reformulated with (2.16) in mind, which yields

$$\max_W \sum_{i=1}^n \|\mathbf{x}_i - W^T W \mathbf{x}_i\|_2^2, \text{s.t. } W W^T = I. \quad (2.18)$$

Thus, this means $\mathbf{z} = e_{\phi}(\mathbf{x}) = W \mathbf{x} \in \mathbb{R}^h$ is the encoding represented by the first h *principal components*, while the decoder is $g_{\theta}(\mathbf{z}) = W^T \mathbf{z}$. The solution to (2.18) is obtained by collecting the first h eigenvectors of the covariance matrix of the training data, e.g. through its eigendecomposition, or by computing the *singular value decomposition* of the data matrix. Like in the domain-based methods in Sec. 2.2.3, some of the restrictions imposed by the linear formulation of classical PCA are circumvented by using a **kernel PCA** (kPCA) [111], where \mathbf{x} is replaced by its nonlinear transformation $\Phi(\mathbf{x})$. This was used for anomaly detection e.g. in [112].

An **autoencoder** (AE) [113] is in its basic principle a nonlinear PCA, where the encoder e_{ϕ} and decoder g_{θ} are neural networks and the parameters ϕ, θ are the trainable weights of these networks. The nonlinearity comes from the use of nonlinear activation functions between the individual layers of the neural networks. An example of an AE

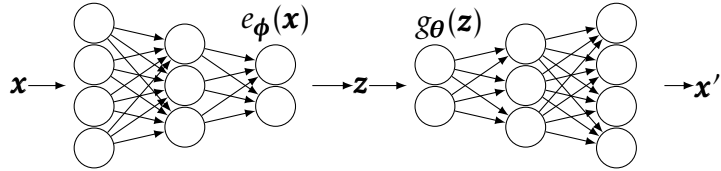


Figure 2.6: An example of an autoencoder consisting of fully connected layers. The latent code $\mathbf{z} \in \mathbb{R}^2$ is computed by propagating the input $\mathbf{x} \in \mathbb{R}^4$ through the encoder $e_\phi(\mathbf{x})$ and then used to produce the reconstruction $\mathbf{x}' \in \mathbb{R}^4$ via the decoder $g_\theta(\mathbf{z})$.

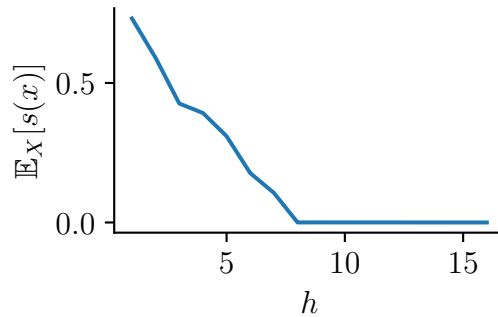


Figure 2.7: The figure demonstrates the ability of an autoencoder to reconstruct data. The dimension h of the latent space \mathcal{Z} is on the x-axis, while the average reconstruction error (2.17) over the whole dataset is on the y-axis. Note that although the artificial dataset is 16-dimensional, it only contains 8 non-correlated dimensions while the remaining are a linear combination of them, which makes the data lie on an 8-dimensional manifold. This results in the error dropping to zero for $h \geq 8$ where the model is able to disentangle the correlations and learn the identity function.

2.2 Anomaly detectors taxonomy

network is in Fig. 2.6. To find the weights of the neural networks, the reconstruction error (2.17) is minimized

$$\mathcal{L}_{\text{AE}}(\mathbf{x}, \boldsymbol{\phi}, \boldsymbol{\theta}) = \|\mathbf{x} - g_{\boldsymbol{\theta}}(e_{\boldsymbol{\phi}}(\mathbf{x}))\|_2^2 \quad (2.19)$$

with respect to $\boldsymbol{\phi}, \boldsymbol{\theta}$ using a gradient descent technique, such as ADAM [114] or AMSGrad [115], which use backpropagation [116]. Note that the explicit regularization term \mathcal{R} from (2.16) here is omitted and instead, the regularization is enforced by creating a *bottleneck* $h < d$, which again forces the model to find the optimal representation of data on a manifold of the data space, as is demonstrated in Fig. 2.6. Other types of regularizations include sparse autoencoders [117], where sparsity of encodings is enforced, or denoising autoencoders [118], which reconstruct samples with added artificial noise. The process of training an autoencoder is described in Alg. 1. Note that the space if inputs \mathcal{X} might be an Euclidean space \mathbb{R}^d for tabular data, while RGB images are usually represented by three-dimensional tensors of width W and height H , therefore $\mathcal{X} = \mathbb{R}^{H \times W \times 3}$. In that case, the computation of loss (2.19) on samples remains the same as if the inputs were vectorized because the operation is element-wise. The main difference when working with image data is the architecture of a neural network, where convolutional layers are usually used instead of dense layers, as they have some favourable properties, such as translational invariance [119].

Autoencoders were used for anomaly detection e.g. in [120, 121], where the reconstruction error (2.17) is used as the anomaly score, and also as a powerful nonlinear dimensionality reduction technique coupled with traditional method in a two-stage approach, as in [95, 122]. They are also the basis for the Variational autoencoder, which will be discussed in depth in the next chapter.

Algorithm 1 Autoencoder training procedure.

Require: Autoencoder ($g_{\boldsymbol{\theta}}, e_{\boldsymbol{\phi}}$), a training set $X = \{\mathbf{x}_1, \mathbf{x}_2, \dots, \mathbf{x}_n\} \subset \mathcal{X}$, maximum number of iterations $I \in \mathbb{N}$, batchsize $B \in \mathbb{N}$.

- 1: $\boldsymbol{\phi}, \boldsymbol{\theta} \leftarrow$ Initialize weights
 - 2: $i \leftarrow$ Iteration counter
 - 3: **while** $i < I$ or $\boldsymbol{\phi}, \boldsymbol{\theta}$ are not converged **do**
 - 4: $X_B \leftarrow$ A random batch of B samples from X
 - 5: $l \leftarrow \frac{1}{B} \sum_{i=1}^B \mathcal{L}_{\text{AE}}(\mathbf{x}_i, \boldsymbol{\phi}, \boldsymbol{\theta}), \mathbf{x}_i \in X_B$
 - 6: $\boldsymbol{\phi} \leftarrow -\nabla_{\boldsymbol{\phi}} l$, update of encoder weights
 - 7: $\boldsymbol{\theta} \leftarrow -\nabla_{\boldsymbol{\theta}} l$, update of decoder weights
 - 8: $i \leftarrow i + 1$
 - 9: **end while**
 - 10: **return** encoder $e_{\boldsymbol{\phi}}(\mathbf{x})$, decoder $g_{\boldsymbol{\theta}}(\mathbf{z})$
-

3

Generative models in anomaly detection

Suppose that a given problem (e.g. classification) requires us to model some directly observable data, denoted by \mathbf{x} , which is somehow connected with a second variable \mathbf{z} , which might not be directly observable, or we only have a finite set of observed pairs (\mathbf{x}, \mathbf{z}) . When \mathbf{z} is discrete, it has the interpretation of a **label** which denotes an affiliation with one of a finite number of classes (in that case, it is often denoted by \mathbf{y} instead). When it is continuous, we use the term **hidden** or **latent** variable, see Sec. 2.2.1, where it was already discussed. In that case, we assume that there is some mechanism that connects \mathbf{x} and \mathbf{z} that can be modeled e.g. by a decoder $g_\theta(\mathbf{z})$ from Sec. 2.2.4. The term **generative model** denotes an approach when the joint probability distribution of $p(\mathbf{x}, \mathbf{z})$ is modeled, as opposed to a **discriminative model**, which tries to estimate $p(\mathbf{z}|\mathbf{x})$. An example of a discriminative model is a logistic classifier, which in fact estimates $p(\mathbf{z}|\mathbf{x})$ as a function $f : \mathcal{X} \rightarrow \mathcal{Z}$ where $\mathcal{Z} = [0, 1]$, i.e. it produces a guess for binary label based on input data. While it seems that a generative model is more flexible, as it can provide $p(\mathbf{z}|\mathbf{x}) = p(\mathbf{x}, \mathbf{z})/p(\mathbf{x})$, it is usually subpar in classification tasks [123, 124]. The advantage of using a generative model is that it can generate artificial samples \mathbf{x} , and most importantly, it can be trained in an unsupervised manner (without observed labels/latent variables) and provide an estimate of the data distribution $p(\mathbf{x})$. This is the reason generative models are interesting for anomaly detection, together with the advent of deep generative models that can model large quantities of high-dimensional data.

Some generative models were already introduced in Sec. 2.2.1, such as the Gaussian Mixture Model, autoregressive models, or various energy-based models. Recently, very large deep generative models with billions of parameters were introduced. They are pushing the boundaries in many domains and produce human-like outputs, such as the BigGAN [125] for images, GPT-3 [126] for text, the Jukebox model [127] for music generation, or diffusion models [128] for text-to-image translation [129]. In the previous chapter, we have already mentioned the three main types of deep generative models that will be discussed in greater depth in this chapter – the **Generative Adversarial Network** (GAN) [32], the **Variational Autoencoder** (VAE) [33] and various **flow models** [34]. They present the basic paradigms on which most of the novel anomaly detectors are built [130, 131, 132, 133, 134, 135].

3.1 GAN-based models

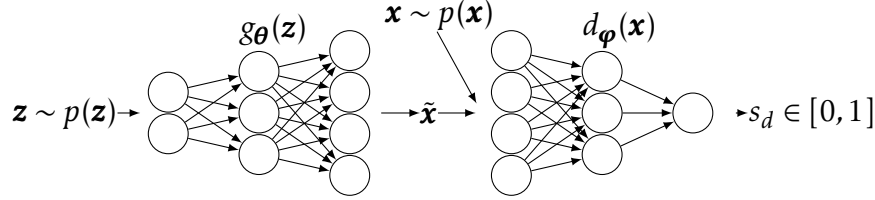


Figure 3.1: A schematic of a GAN consisting of fully connected layers. A latent noise sample $z \sim p(z)$ is fed to the generator $g_{\theta}(z)$ which then produces an artificial sample \tilde{x} . Alternatively, a sample x is sampled from the data distribution $p(x)$. Both are passed to the discriminator $d_{\varphi}(x)$ that produces a score s_d – the probability that \tilde{x} or x come from the true data distribution.

3.1 GAN-based models

The **Generative Adversarial Network** (GAN) was introduced in [32] where it was successfully used to generate MNIST digits, faces, and CIFAR-10 images. Since then, GAN-based models were used in a multitude of different areas, such as next frame prediction in videos [136], semi-supervised learning [137], image-to-image translation [138], semantic manipulation of high-resolution images [139] or for generating realistic artificial image [140] and audio data [141]. In comparison with VAE-based generative models, it is believed that GAN-based models produce pictures that are more realistic (less blurry), at the cost of difficult and highly unstable training [137]. In the following text, the basics of GANs will be introduced together with their applications in anomaly detection.

3.1.1 Basic GAN model

Suppose that there is a true data distribution $p(\mathbf{x}), \mathbf{x} \in \mathcal{X}$, which we are trying to imitate. We don't know the true form of $p(\mathbf{x})$, since it is usually high-dimensional and not representable directly by a function, but instead, it is available to us through a finite set of samples that comprise the training dataset $X = \{\mathbf{x}_1, \mathbf{x}_2, \dots, \mathbf{x}_n\} \subset \mathcal{X}$. The goal is to build a proxy for $p(\mathbf{x})$ so that we can draw new, yet unseen samples from it. The GAN tackles this problem by constructing a model with two principal parts. First is the **generator**, which is a neural network that represents a mapping $g_{\theta}(\mathbf{z}) : \mathcal{Z} \rightarrow \mathcal{X}$, where θ are its weights, and \mathcal{Z} is the latent space. Note that we use the same notation for the generator that was already used for a decoder in the AE model – this is because they fulfill the same role in both models. We will denote a generated sample by $\tilde{\mathbf{x}} = g_{\theta}(\mathbf{z})$. Since the generator, as we have defined it so far, is deterministic and we need to cover a random distribution, the inputs to the generator come from a **prior** noise distribution $p(\mathbf{z})$. The prior is usually chosen such that it is easy to generate samples from it, e.g. $p(\mathbf{z}) = \mathcal{N}(0, I)$, in which case $\mathcal{Z} = \mathbb{R}^h$ with h being the dimension of the latent space. Then, the task is to train the generator in such a fashion that it learns the potentially highly non-linear mapping from $p(\mathbf{z})$ to $p(\mathbf{x})$. This is stimulated by the adversary of the generator – the **discriminator**. We define it as a neural network with weights φ , i.e. a mapping $d_{\varphi}(\mathbf{x}) : \mathcal{X} \rightarrow [0, 1]$. The output of the discriminator has the interpretation of the probability that its input comes from $p(\mathbf{x})$ rather than being generated by the

generator, in other words, true samples \mathbf{x} should be given a higher value than the generated samples $\tilde{\mathbf{x}}$.

Both parts of a GAN are trained (their weights are updated) in tandem, so each of them iteratively improves in its task. The discriminator is trained both with true and generated samples to maximize the probability of assigning the correct label to them, while the generator is minimizing the probability of the discriminator recognizing the generated sample. This can be written down as a two-player minimax [142] game

$$\min_{\boldsymbol{\theta}} \max_{\boldsymbol{\varphi}} \mathbb{E}_{\mathbf{x} \sim p(\mathbf{x})} [\ln d_{\boldsymbol{\varphi}}(\mathbf{x})] + \mathbb{E}_{\mathbf{z} \sim p(\mathbf{z})} [\ln(1 - d_{\boldsymbol{\varphi}}(g_{\boldsymbol{\theta}}(\mathbf{z})))]. \quad (3.1)$$

It can be shown [32] that this objective has a saddle point at $-\ln 4$. In practice, (3.1) is not used directly. That is because the term $\ln(1 - d_{\boldsymbol{\varphi}}(g_{\boldsymbol{\theta}}(\mathbf{z})))$ suffers from vanishing gradients – when the generated samples do not resemble the real data at the beginning of the training, this term is almost zero and the generator is not trained. Therefore, instead of minimizing this, we can maximize $\ln d_{\boldsymbol{\varphi}}(g_{\boldsymbol{\theta}}(\mathbf{z}))$ to train the generator, which has much stronger gradients [32]. During the training, we sample \mathbf{x} from the training dataset and \mathbf{z} from the prior distribution and update the generator and discriminator weights by minimizing

$$\mathcal{L}_g(\mathbf{z}, \boldsymbol{\theta}) = -\ln d_{\boldsymbol{\varphi}}(g_{\boldsymbol{\theta}}(\mathbf{z})), \quad (3.2)$$

$$\mathcal{L}_d(\mathbf{x}, \mathbf{z}, \boldsymbol{\varphi}) = -\ln d_{\boldsymbol{\varphi}}(\mathbf{x}) - \ln(1 - d_{\boldsymbol{\varphi}}(g_{\boldsymbol{\theta}}(\mathbf{z}))). \quad (3.3)$$

Note that we explicitly remove the dependency of the loss functions on the weights that are not being optimized through them. A detailed training procedure of a GAN is described in Alg. 2. Interestingly, during training, the generator never encounters any sample coming from $p(\mathbf{x})$ but is still able to eventually learn the shape of $p(\mathbf{x})$. The choice of $p(\mathbf{z})$ can be rather arbitrary as far as sampling from it is possible and the generator and discriminator have sufficient capacity to process it. In practice, uniform or normal distribution is usually used.

Algorithm 2 GAN training procedure.

Require: Generator $g_{\boldsymbol{\theta}}$, discriminator $d_{\boldsymbol{\varphi}}$, a training set $X = \{\mathbf{x}_1, \mathbf{x}_2, \dots, \mathbf{x}_n\} \subset \mathcal{X}$, maximum number of iterations $I \in \mathbb{N}$, batchsize $B \in \mathbb{N}$.

- 1: $\boldsymbol{\theta}, \boldsymbol{\varphi} \leftarrow$ Initialize weights
 - 2: $i \leftarrow$ Iteration counter
 - 3: **while** $i < I$ or $\boldsymbol{\theta}, \boldsymbol{\varphi}$ are not converged **do**
 - 4: $X_B \leftarrow$ A random batch of B samples from X
 - 5: $Z_B \leftarrow$ A random batch of B samples from $p(\mathbf{z})$
 - 6: $l_d \leftarrow \frac{1}{B} \sum_{j=1}^N \mathcal{L}_d(\mathbf{x}_j, \mathbf{z}_j, \boldsymbol{\varphi}), \mathbf{x}_j \in X_B, \mathbf{z}_j \in Z_B$
 - 7: $\boldsymbol{\varphi} \leftarrow -\nabla_{\boldsymbol{\varphi}} l_d$, update of discriminator weights
 - 8: $l_g \leftarrow \frac{1}{L} \sum_{j=1}^L \mathcal{L}_g(\mathbf{z}_j, \boldsymbol{\theta}), \mathbf{z}_j \in Z_L$
 - 9: $\boldsymbol{\theta} \leftarrow -\nabla_{\boldsymbol{\theta}} l_g$, update of generator weights
 - 10: $i \leftarrow i + 1$
 - 11: **end while**
 - 12: **return** generator $g_{\boldsymbol{\theta}}(\mathbf{z})$, discriminator $d_{\boldsymbol{\varphi}}(\mathbf{x})$
-

3.1 GAN-based models

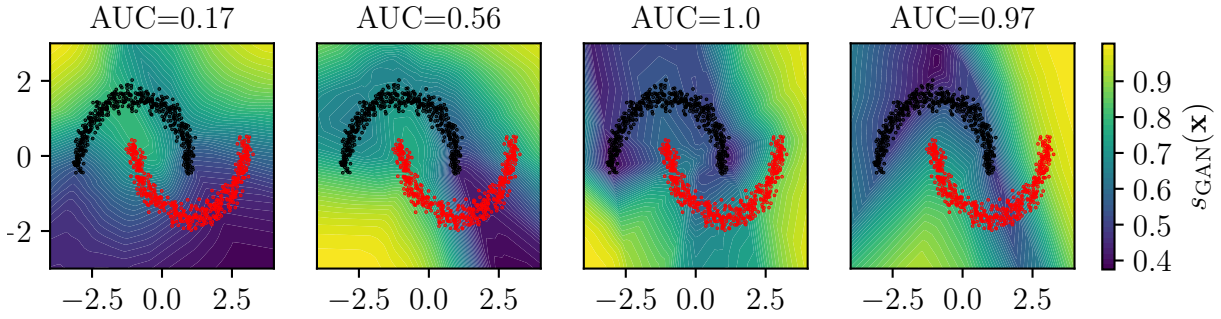


Figure 3.2: Four different GAN models trained on the normal (black) data of the *two bananas* dataset, the contours of the respective anomaly scores (3.6) and the AUC of the model with respect to the anomalous (red) data. The models differ only in the initial values of their weights, yet they converged to very different states. Most importantly, it is evident that the discriminator can output arbitrary values in the areas where training data is not present.

Achieving convergence such that the generated samples $\tilde{\mathbf{x}}$ resemble the training data might be difficult and require multiple random initializations of the model weights, see Fig. 3.2. Details on stable training of GANs can be found e.g. in [143]. A phenomenon called **mode collapse** has been described [144], which happens when $p(\mathbf{x})$ is multimodal, but the generator distribution collapses to a single mode. A generator that has collapsed to a single mode of an MNIST dataset will produce only a single digit, e.g. "1", no matter where the code is sampled from. To mitigate this issue, several practices have been proposed [137, 145]. One of them is the use of an enhanced generator loss

$$\mathcal{L}_{\text{gfm}}(\mathbf{z}, \mathbf{x}, \boldsymbol{\theta}) = \alpha \mathcal{L}_g(\mathbf{z}, \boldsymbol{\theta}) + \mathcal{L}_{fm}(\mathbf{z}, \mathbf{x}, \boldsymbol{\theta}), \quad (3.4)$$

where $\alpha > 0$ is a tunable weight and the second term is the so-called **feature-matching** loss

$$\mathcal{L}_{fm}(\mathbf{z}, \mathbf{x}, \boldsymbol{\theta}) = \|d_{n, \boldsymbol{\varphi}}(\mathbf{x}) - d_{n, \boldsymbol{\varphi}}(g_{\boldsymbol{\theta}}(\mathbf{z}))\|_2^2. \quad (3.5)$$

Here, $d_{n, \boldsymbol{\varphi}}(\mathbf{x})$ is the intermediate representation of \mathbf{x} after propagation through $n \in \mathbb{N}$ layers of the discriminator. This loss is supposed to provide improved gradients for the generator to stabilize the training. In the following text, a GAN model with the loss (3.4) will be referred to as the **feature-matching GAN** (fmGAN).

3.1.2 GANs in anomaly detection

The idea of using a GAN for anomaly detection comes from the ability of the generator to learn the true data distribution $p(\mathbf{x})$ and especially the ability of the discriminator to recognize samples coming from $p(\mathbf{x})$. When the training dataset consists of normal samples, the discriminator output can be converted into an anomaly score

$$s_{\text{GAN}}(\mathbf{x}) = 1 - d_{\boldsymbol{\varphi}}(\mathbf{x}), \quad (3.6)$$

which is higher for suspected anomalies and lower for normal data. The common critique is that the discriminator was not trained to recognize an arbitrary distribution

of the anomalies but only that of the latent transformed by the generator. Thus it may fail to recognize anomalous samples of interest. Also, the training procedure of a GAN model has very high variance in the sense that two models with the same architecture and hyperparameters and trained on the same data might converge to very different states, see Fig. 3.2. This implies that more models need to be created and trained in order to find a good anomaly detector. This is further discussed in Chapter 4.

The authors of the **AnoGAN** model [23] recognize some of these flaws. Their convolutional GAN model is trained with the feature-matching loss (3.4). For identification of anomalies in medical images, instead of using (3.6), they propose an iterative procedure that searches for the latent code \mathbf{z} most likely to generate the tested sample to identify anomalous images. However, this procedure is computationally expensive. Therefore, an update to this model was published, the **f(ast)AnoGAN** [146]. It uses a Wasserstein GAN [147, 148] (more on Wasserstein optimization objective in the next section) with gradient penalization [147] to improve training stability and adds an encoder distribution $q_\phi(\mathbf{z}|\mathbf{x})$ to find \mathbf{z} closest to given \mathbf{x} faster. The anomaly score of fAnoGAN is a combination of the discriminator score (3.6) and the feature-matching loss (3.5).

The fmGAN model is used in the publication [149], where it is tested on benchmark datasets such as MNIST and CIFAR-10. In [132], a GAN model was used to detect anomalies in time series data coming from industrial processes, whereas in [150], network intrusions were detected. In the **Multiple-Objective Generative Adversarial Active Learning** (MOGAAL) [151], $k \in \mathbb{N}$ generators are trained against a single discriminator on input data divided into k subsets. The discriminator score Eq. (3.6) is used to test new samples. The authors of the OCGAN model [133] claim to have achieved state-of-the-art results in one-class classification by severely restricting the latent space of the GAN combined with an autoencoder and employing an adversarial data augmentation strategy.

The use of GAN with an encoder [152] or an autoencoder with a discriminator [153] for anomaly detection is often and somehow blurs the line between GAN and VAE-based models, but we believe that presenting both concepts separately is useful. True GAN-like models for anomaly detection are however far less prevalent than models that use some autoencoding structure, which will be the focus of the next section. An experimental comparison of both approaches is presented in Chapter 4.

3.2 VAE-based models

The **Variational Autoencoder** (VAE) is a generative model that has enjoyed great success in a number of fields since its introduction in [33]. Its basic architecture [154] is very similar to that of an AE model described in Sec. 2.2.4, but that is where the similarities end, as VAE is more of a probabilistic anomaly detector, since it models the probability distribution of the normal data. Unlike in AE, where the encoding to latent space \mathcal{Z} is not constrained from taking any shape or form as far as the learning objective is minimized, in VAE a desired distribution of the encodings is explicitly prescribed in the form of a prior distribution $p(\mathbf{z})$. If the network is trained properly and the encodings follow the prior, we can feed samples from $p(\mathbf{z})$ to the decoder and expect to obtain random samples in the \mathcal{X} space that will resemble those from the training dataset. This is the simple principle of how VAE works — more details will be given in the following text.

3.2 VAE-based models

The VAE has been mainly used for generation of artificial images such as faces [155] or sentences [156], but also for other tasks such as semi-supervised learning [157], segmentation [158], static image forecasting [159] and of course for anomaly detection [130, 131, 160]. Since its popularity, a multitude of approaches enhancing the original VAE has been published, approaching the paradigm from different angles, with some of the more prominent examples published in [161, 162, 163, 164, 165]. In the following text, we will go through the basic theory, its implications for the basic VAE, and through some of the extensions.

3.2.1 Basic VAE

Let's begin by defining the VAE from a probabilistic perspective. Assume that there is a dataset X consisting of i.i.d samples. We want to obtain a tractable estimate of the true data distribution $p(\mathbf{x})$ in order to be able to sample from it. For that purpose, suppose that there is a hidden random process that generates the data and which involves a latent variable \mathbf{z} . Then, like in the case of the GAN model, we can redirect the sampling from the data space \mathcal{X} to the latent space \mathcal{Z} , in which it might be easier. Specifically, we want to sample from the latent prior distribution specified by a density $p(\mathbf{z})$, then pass this sample to the generative distribution with density $p_{\theta}(\mathbf{x}|\mathbf{z})$, where θ are its parameters, and obtain a sample \mathbf{x} that will be very similar to the samples coming from the true data distribution $p(\mathbf{x})$. In other words, we want to maximize the probability of each sample obtained through the generative process

$$p_{\theta}(\mathbf{x}) = \int_{\mathcal{Z}} p_{\theta}(\mathbf{x}|\mathbf{z})p(\mathbf{z})d\mathbf{z}. \quad (3.7)$$

Unfortunately, there are several issues with this. Firstly, we do not know the optimal value of parameters θ . Secondly, the integral (3.7) is usually intractable, e.g. in the case where $p_{\theta}(\mathbf{x}|\mathbf{z})$ is represented by a neural network. Finally, we want to avoid expensive sampling methods such as Monte Carlo Expectation Maximization [166]. A sampling procedure is eventually used, but we only want to pass such samples \mathbf{z} to the generative model that will already be very likely under $p_{\theta}(\mathbf{x}|\mathbf{z})$. To this end, we introduce a discriminative distribution $q_{\phi}(\mathbf{z}|\mathbf{x})$ which is an approximation of the true intractable posterior $p(\mathbf{z}|\mathbf{x})$, with parameters ϕ .

The ELBO objective

Now, we would like to relate the generative and discriminative distributions together in a way that would enable us to optimize the model with respect to ϕ, θ . Continuing from (3.7),

$$\ln p_{\theta}(\mathbf{x}) = \mathbb{E}_{q_{\phi}(\mathbf{z}|\mathbf{x})}[\ln p_{\theta}(\mathbf{x})] = \mathbb{E}_{q_{\phi}(\mathbf{z}|\mathbf{x})}[\ln p_{\theta}(\mathbf{x}|\mathbf{z}) + \ln p(\mathbf{z}) - \ln p(\mathbf{z}|\mathbf{x})], \quad (3.8)$$

where we have used the Bayes' rule and the fact that $p_{\theta}(\mathbf{x})$ does not depend on \mathbf{z} . Now we use the KL divergence (A.5)

$$\ln p_{\theta}(\mathbf{x}) - D_{\text{KL}}(q_{\phi}(\mathbf{z}|\mathbf{x})||p(\mathbf{z}|\mathbf{x})) = \mathbb{E}_{q_{\phi}(\mathbf{z}|\mathbf{x})}[\ln p_{\theta}(\mathbf{x}|\mathbf{z}) + \ln p(\mathbf{z}) - \ln q_{\phi}(\mathbf{z}|\mathbf{x})] \quad (3.9)$$

$$= \mathbb{E}_{q_{\phi}(\mathbf{z}|\mathbf{x})}[\ln p_{\theta}(\mathbf{x}|\mathbf{z})] - D_{\text{KL}}(q_{\phi}(\mathbf{z}|\mathbf{x})||p(\mathbf{z})) \quad (3.10)$$

$$= -\mathcal{L}_{\text{VAE}}(\mathbf{x}, \phi, \theta) \quad (3.11)$$

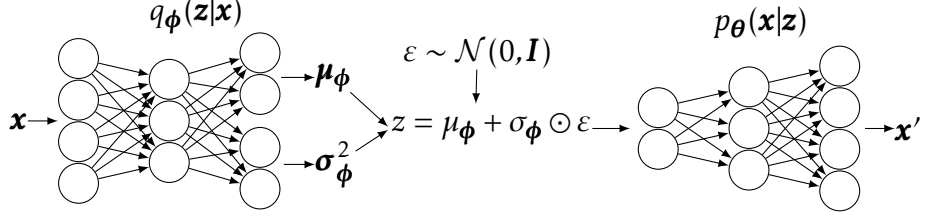


Figure 3.3: A schematic of a Variational Autoencoder consisting of fully connected layers with a Gaussian encoder $q_\phi(\mathbf{z}|\mathbf{x})$ with mean μ_ϕ and variance σ_ϕ^2 , which are extracted from the last layer of the encoder. They are used to sample an encoding \mathbf{z} through the reparametrization trick with a noise variable ϵ . The encoding is then passed forward and the reconstruction \mathbf{x}' is sampled from the decoder $p_\theta(\mathbf{x}|\mathbf{z})$.

This is the variational lower bound of the VAE model, sometimes called **ELBO** (evidence lower boundary) through which we can optimize the marginal likelihood $p_\theta(\mathbf{x})$. This is due to the fact that the analytically unsolvable term $D_{\text{KL}}(q_\phi(\mathbf{z}|\mathbf{x})||p(\mathbf{z}|\mathbf{x}))$ is always nonnegative, thus by maximization of ELBO (minimization of $\mathcal{L}_{\text{VAE}}(\mathbf{x}, \phi, \theta)$) we also maximize $p_\theta(\mathbf{x})$.

By looking at the individual parts of Eq. (3.10), we can see that by maximizing the ELBO, we simultaneously maximize the likelihood $p_\theta(\mathbf{x}|\mathbf{z})$ and minimize the distance between $q_\phi(\mathbf{z}|\mathbf{x})$ and $p(\mathbf{z})$. While looking at the left-hand side of (3.9) we can see that at the same time, the marginal likelihood $p_\theta(\mathbf{x})$ is maximized, and the error term $D_{\text{KL}}(q_\phi(\mathbf{z}|\mathbf{x})||p(\mathbf{z}|\mathbf{x}))$ is minimized, forcing the shape of $q_\phi(\mathbf{z}|\mathbf{x})$ to the true posterior. Also, (3.10) captures the autoencoding nature of the VAE model. We pass \mathbf{x} to the discriminative distribution, which acts as an encoder, sample latent encoding $\mathbf{z} \sim q_\phi(\mathbf{z}|\mathbf{x})$ and pass this back to generative distribution, which acts as a decoder, to obtain a reconstructed sample $\mathbf{x}' \sim p_\theta(\mathbf{x}|\mathbf{z})$. From this point on, we will use the term encoder and decoder to describe the discriminative and generative distributions.

Vanilla VAE

To be able to optimize (3.11), we must make some additional assumptions about the model. Here, we will describe those that were made by the authors of the original "vanilla" VAE model. Note that different assumptions are feasible, such as the choice of the prior or decoder distribution. First, suppose that $\mathcal{X} = \mathbb{R}^d$, although the following generally holds even for image data, where $\mathcal{X} = \mathbb{R}^{H \times W \times 3}$, see the comment at the end of Sec. 2.2.4. Additionally, the **prior** $p(\mathbf{z})$ is chosen to be an h -dimensional unit normal distribution $p(\mathbf{z}) = \mathcal{N}(\mathbf{z}|0, \mathbf{I})$. The encoded training data are expected to follow this distribution after optimization and it is used for the generation of new samples. In tandem with this, the encoder is assumed to model a normal distribution with a diagonal covariance matrix $q_\phi(\mathbf{z}|\mathbf{x}) = \mathcal{N}(\mathbf{z}|\mu_\phi(\mathbf{x}), \text{diag}(\sigma_\phi^2(\mathbf{x}))), \mu_\phi, \sigma_\phi^2 : \mathbb{R}^d \rightarrow \mathbb{R}^h$, where the mean and variance estimates are computed by neural networks with shared weights ϕ . These choices lead to an analytically solvable expression for the KL divergence

3.2 VAE-based models

in (3.10), see (A.10) in the Appendix

$$D_{\text{KL}}(q_{\phi}(z|x)||p(z)) = \frac{1}{2} \sum_{i=1}^d 1 - \sigma_{\phi,i}^2(x) + \ln \sigma_{\phi,i}^2(x) - \mu_{\phi,i}^2(x). \quad (3.12)$$

Second, the optimization of the ELBO (3.11) requires sampling from the encoder $q_{\phi}(z|x)$. This is however problematic for optimization by backpropagation because sampling is not a differentiable operation. Therefore, a **reparametrization trick** was introduced in [33]. Instead of directly drawing samples from $q_{\phi}(z|x)$, we first take a sample from an h -dimensional noise distribution $\epsilon \sim p(\epsilon) = \mathcal{N}(0, \mathbf{I})$ and then compute the encoding as $z = \mu_{\phi}(x) + \sigma_{\phi}(x) \odot \epsilon$, where \odot denotes element-wise multiplication. This changes the first term of the ELBO, which is called the **log-likelihood** to

$$\mathbb{E}_{q_{\phi}(z|x)}[\ln p_{\theta}(x|z)] = \mathbb{E}_{\epsilon \sim \mathcal{N}(0, \mathbf{I})}[\ln p_{\theta}(x|\mu_{\phi}(x) + \sigma_{\phi}(x) \odot \epsilon)]. \quad (3.13)$$

In the following text, whenever it can apply, we use the notation $z \sim q_{\phi}(z|x)$ as a shorthand for the reparametrization trick.

Finally, the decoder $p_{\theta}(x|z)$ is also assumed to model a normal distribution $\mathcal{N}(x|\mu_{\theta}(z), \sigma^2 I)$, $\mu_{\theta} : \mathbb{R}^h \rightarrow \mathbb{R}^d$, $\sigma^2 \in \mathbb{R}^+$, although a Bernoulli distribution is sometimes used for data scaled to the interval $[0,1]$. The mean of the decoder distribution is again represented by a neural network with weights θ . The variance parameter σ^2 is either fixed, or it can be estimated from data during training. Therefore, the log-likelihood takes on the form

$$\ln p_{\theta}(x|z) = -\frac{1}{2\sigma^2} \|x - \mu_{\theta}(z)\|_2^2 - \frac{d}{2} \ln 2\pi - d \ln \sigma. \quad (3.14)$$

Note that the last two terms can be left out of the optimization since they are not dependent on any inputs or weights. Again, we see the connection with an autoencoding model, where the log-likelihood (3.14) has a very similar form to the objective (2.19). Here, the reconstruction takes the form of $x' = \mu_{\theta}(z)$. A notable property of the VAE model is that the reconstruction is stochastic, which is due to the sampling used in the reparametrization trick (3.13).

Now, we combine the assumptions and equations (3.12)–(3.14) to derive the final analytic form of the ELBO objective. The expectation in (3.13) is replaced by a mean of $L \in \mathbb{N}$ samples of z through the reparametrization trick. The VAE loss function, which is minimized with respect to ϕ, θ , and which is equal to negative ELBO (3.11), has the form

$$\mathcal{L}_{\text{VAE}}(x, \phi, \theta) = \frac{1}{2\sigma^2 L} \sum_{l=1}^L \|x - \mu_{\theta}(z^l)\|_2^2 - \frac{1}{2} \sum_{i=1}^d 1 - \sigma_{\phi,i}^2(x) + \ln \sigma_{\phi,i}^2(x) - \mu_{\phi,i}^2(x), \quad (3.15)$$

$$z^l = \mu_{\phi}(x) + \sigma_{\phi}(x) \odot \epsilon^l, \epsilon^l \sim \mathcal{N}(0, \mathbf{I}).$$

We set $L = 1$ in accordance with [33]. The objective (3.15) can be directly optimized via gradient descent techniques. Neural networks are used in place of the encoder and decoder, since they have been proven to be universal function approximators. Given enough capacity, data, and training time, the decoder can theoretically learn a mapping from the prior to an arbitrary function. See Fig. 3.3 for a schematic example of a VAE model. The training procedure of a VAE is described in Alg. 3. An example of the outputs of a VAE model trained on the MNIST hand-written digits dataset (see Appendix B.2) is in Fig. 3.4.

Algorithm 3 Variational Autoencoder training procedure.

Require: A VAE model with encoder $q_{\phi}(\mathbf{z}|\mathbf{x})$ and decoder $p_{\theta}(\mathbf{x}|\mathbf{z})$, training set $X = \{\mathbf{x}_1, \mathbf{x}_2, \dots, \mathbf{x}_n\} \subset \mathcal{X}$, maximum number of iterations $I \in \mathbb{N}$, batchsize $B \in \mathbb{N}$.

```

1:  $\phi, \theta \leftarrow$  Initialize parameters
2:  $i \leftarrow$  Iteration counter
3: while  $i < I$  or  $\phi, \theta$  are not converged do
4:    $X_B \leftarrow$  A random batch of  $B$  samples from  $X$ 
5:    $l \leftarrow \frac{1}{B} \sum_{j=1}^L \mathcal{L}_{\text{VAE}}(\mathbf{x}_j, \phi, \theta), \mathbf{x}_j \in X_B$ 
6:    $\phi \leftarrow \nabla_{\phi}^+ l$  update of encoder weights
7:    $\theta \leftarrow \nabla_{\theta}^+ l$  update of decoder weights
8:    $i \leftarrow i + 1$ 
9: end while
10: return encoder  $q_{\phi}(\mathbf{z}|\mathbf{x})$ , decoder  $p_{\theta}(\mathbf{x}|\mathbf{z})$ 
```

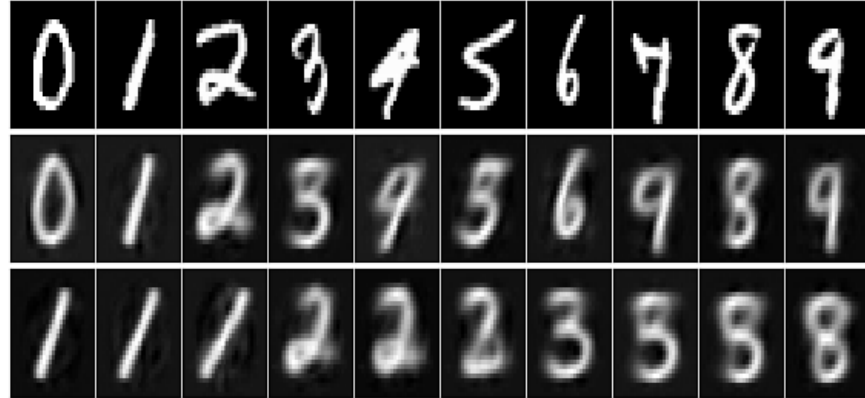


Figure 3.4: Example of a simple VAE trained on the MNIST dataset. Here, the neural networks modelling the encoder and decoder parameters contained two levels of convolutional blocks. Ground truth examples are in the top row, reconstructed samples are in the middle row, and artificially generated digits are in the bottom row. The reconstructions are blurry, which is a typical VAE behaviour. Also, the reconstruction is imperfect for digits that resemble each other, such as "9", "4" and "7", or "3" and "8". The artificial digits were created by linearly interpolating between two coordinates in the latent space and using this as an input to the decoder. The VAE then produces a smooth interpolation between digits "1" and "8" that contains the related digits "2" and "3".

3.2 VAE-based models

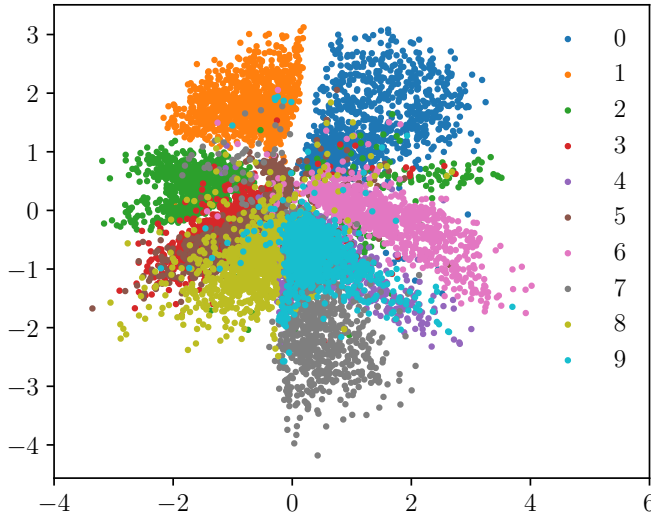


Figure 3.5: The latent space of the MNIST dataset produced by a VAE with a two-dimensional latent space. Note the overlapping of some digit encodings, e.g. "7" and "9".

Some VAE properties

If a VAE model is correctly trained, we can assume that the encoder $q_{\phi}(\mathbf{z}|\mathbf{x})$ and prior $p(\mathbf{z}) = \mathcal{N}(\mathbf{z}|0, \mathbf{I})$ are close to each other. Then, samples from the prior can be fed to the decoder and one can expect artificial samples that resemble the training data. A **generated sample** can therefore be described as

$$\tilde{\mathbf{x}} = \mu_{\theta}(\mathbf{z}), \mathbf{z} \sim p(\mathbf{z}). \quad (3.16)$$

Note that a **reconstructed sample** is instead obtained by sampling the encoding \mathbf{z} from the encoder through the reparametrization trick (3.13).

Fig. 3.5 shows the latent space of an example VAE model. Note that although the overall distribution of the encodings resembles the normal prior, in order to be able to reconstruct the samples from the encodings, the model has to learn to encode the samples from different digit classes to different parts of the latent space. It was shown in [161] that the reconstruction and regularization parts of the VAE loss (3.11) actually work against each other. A model with an encoder perfectly copying the randomness of the prior would not be able to reconstruct the inputs. On the other hand, a model without the latent regularization would not be able to generate new samples, as it would be practically identical to an AE model from Sec. 2.2.4, which is free to encode the different classes to arbitrary parts of the latent space. The basic loss (3.15) leads to a model that is usually in an equilibrium between both of these states. It is however possible to push the model in one of these directions by using a scaling parameter β

$$\mathcal{L}_{\beta \text{VAE}}(\mathbf{x}, \phi, \theta, \beta) = -\mathbb{E}_{q_{\phi}(\mathbf{z}|\mathbf{x})}[\ln p_{\theta}(\mathbf{x}|\mathbf{z})] + \beta D_{\text{KL}}(q_{\phi}(\mathbf{z}|\mathbf{x}) || p(\mathbf{z})), \beta > 0. \quad (3.17)$$

A VAE model trained with this loss is known as **BetaVAE** [161] and is one of the first VAE-based models that attempt some sort of **unsupervised disentanglement**. A disentangled model captures the possible factors of variation of a dataset in orthogonal

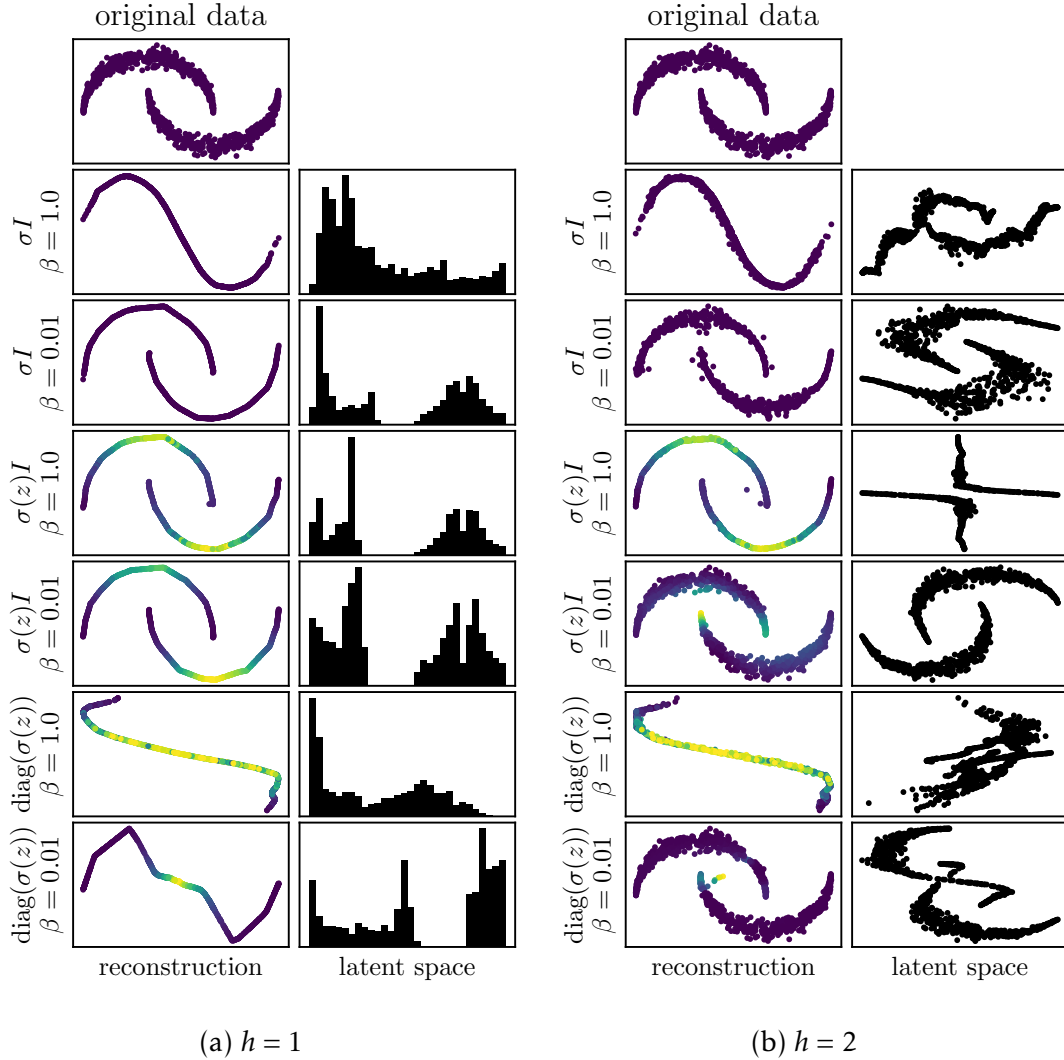


Figure 3.6: An overview of VAE behaviour with respect to the scaling parameter β of the objective (3.17) and to the way the covariance of the decoder $p_{\theta}(x|z)$ is estimated. The VAE model was trained on the *two moons* data, plotted in the plots at the very top. Variants with 1D (a) and 2D (b) latent spaces are compared, and means of the decoder $\mu_{\theta}(z)$ are plotted on the left and the latent representations on the right. Clearly, smaller values of β lead to better sample reconstruction, especially in the case of a two-dimensional latent space, as well as leading to a better separation of the encodings. This is understandable, since the prior $p(z) = \mathcal{N}(0, \mathbf{I})$ is unimodal. From the top: the covariance of the decoder is given either by a fixed scalar ($\sigma^2 I, \sigma = 1$), by a scalar estimated from the data ($\sigma^2(z) I$), or by an estimate of its diagonal terms ($\text{diag}(\sigma^2(z))$). The magnitude of the estimated variance in the two latter cases is denoted by color, where a brighter color corresponds to a higher value of variance. It is interesting that the second case ($\sigma^2(z) I$) seems to alleviate the reconstruction difficulties with higher β , while the estimation of the full covariance diagonal does not exhibit such property. Also, the third case seems to "exploit" the estimation of variance. Instead of pushing and optimizing the mean, it can instead simply output a higher variance in the direction in which the reconstruction is worse and still incur only a small loss. Due to this behaviour, the second case seems to be the most robust and stable way of estimating the reconstruction variance, at least on this simple dataset. Not surprisingly, the 2D case provides better reconstructions since it was provided with one more dimension to encode data to.

3.2 VAE-based models

dimensions of the latent space. Imagine a colored MNIST dataset, on which a disentangled model with a two-dimensional latent space is trained. If properly disentangled, one latent dimension would capture the identity of the digit, while the other one would capture its color. This concept will be again revisited in Chapter 5. The influence of the β parameter is discussed in Fig. 3.6.

Instead of setting a fixed variance parameter σ^2 in the decoder, one can optimize and extract it instead from the last layer of the decoder, either as a scalar $\sigma_\theta^2(\mathbf{z}) \in \mathbb{R}^+$ or even a full diagonal of the covariance $\text{diag}(\sigma_\theta^2(\mathbf{z}))$, $\sigma_\theta^2(\mathbf{z}) \in \mathbb{R}^{d+}$. From the experiment in Fig. 3.6, it seems (at least for tabular data) that the best results were surprisingly obtained not by the most complex variant, but the one with a scalar value σ_θ^2 optimized during training.

3.2.2 Wasserstein and adversarial autoencoders

The asymmetry of the KL divergence motivated the search for another feasible metric measuring the distance between the prior and the encoder. An alternative approach to VAE has been published in [167] and improved in [163], which proposes a general form of a generative autoencoder that uses a Wasserstein metric [168]. Unlike the KL divergence term in the VAE loss, which forces all the input data samples to zero (the mean of the standard prior), in **Wasserstein autoencoders** (WAE) the encoding is loosened, which reportedly leads to improved reconstruction [163]. A general form of the loss function of a WAE model is

$$\mathcal{L}_{\text{DW}}(\mathbf{x}, \boldsymbol{\theta}, \boldsymbol{\phi}) = -\mathbb{E}_{q_\phi(\mathbf{z}|\mathbf{x})}[\ln p_\theta(\mathbf{x}|\mathbf{z})] + \lambda D_W(q_\phi(\mathbf{z}|\mathbf{x})||p(\mathbf{z})), \quad (3.18)$$

where $\lambda > 0$ is a scalar hyperparameter, and D_W is a Wasserstein metric. The most commonly used form of the Wasserstein metric is the kernelized **maximum-mean-discrepancy** (MMD) with a kernel function $k_f : \mathbb{R}^h \times \mathbb{R}^h \rightarrow \mathbb{R}$, which was reported to perform well in matching high dimensional distributions [162]. From the theoretical point of view, KLD only matches the first and the second moment of the two distributions, while MMD can potentially match an infinite amount of moments with the right kernel. Some authors [163] argue that by minimizing KLD, the latent representation might become uninformative for the decoder to reconstruct the code. On the other hand, MMD maximizes the mutual information between \mathbf{x} and \mathbf{z} [162].

Under some mild assumptions about the kernel function k_f , which needs to be characteristic and positive-definite (see details in [163]), the MMD can be expressed in such a way that enables optimization of the model by backpropagation. Then, the MMD of the prior and the encoder can be approximated solely by comparing sets of samples from these distributions $Z = \{\mathbf{z}_1, \mathbf{z}_2, \dots, \mathbf{z}_n\}$, $\tilde{Z} = \{\tilde{\mathbf{z}}_1, \tilde{\mathbf{z}}_2, \dots, \tilde{\mathbf{z}}_n\}$, $\mathbf{z}_i \sim q_\phi(\mathbf{z}|\mathbf{x})$, $\tilde{\mathbf{z}}_i \sim p(\mathbf{z})$, $\forall i \in \hat{n}$ in a closed expression

$$\text{MMD}_k(Z, \tilde{Z}) = \frac{1}{n(n-1)} \sum_{i \neq j} k_f(\mathbf{z}_i, \mathbf{z}_j) + \frac{1}{n(n-1)} \sum_{i \neq j} k_f(\tilde{\mathbf{z}}_i, \tilde{\mathbf{z}}_j) - \frac{2}{n^2} \sum_{i,j} k_f(\mathbf{z}_i, \tilde{\mathbf{z}}_j). \quad (3.19)$$

The most notable characteristic of the MMD is that in practice, it only requires samples from the distributions in question, and it is therefore less restricting than the KLD, which required Gaussian prior and encoder in order to obtain the analytic expression (3.12). This offers the potential for the use of a variety of prior and encoder distributions, however, the reparametrization trick (3.13) or a similar technique must

Algorithm 4 Wasserstein autoencoder training procedure.

Require: A WAE model with encoder $q_{\phi}(\mathbf{z}|\mathbf{x})$, decoder $p_{\theta}(\mathbf{x}|\mathbf{z})$ and a prior $p(\mathbf{z})$, training set $X = \{\mathbf{x}_1, \mathbf{x}_2, \dots, \mathbf{x}_n\} \subset \mathcal{X}$, maximum number of iterations $I \in \mathbb{N}$, batchsize $B \in \mathbb{N}$, regularization coefficient $\lambda > 0$, characteristic positive definite kernel k_f , standard deviation parameter $\sigma > 0$.

- 1: $\phi, \theta \leftarrow$ Initialize parameters
- 2: $i \leftarrow$ Iteration counter
- 3: **while** $i < I$ or ϕ, θ are not converged **do**
- 4: $X_B \leftarrow$ A random batch of B samples from X
- 5: $Z \leftarrow \{\mathbf{z}_j \sim q_{\phi}(\mathbf{z}|\mathbf{x}_j), \mathbf{x}_j \in X_B\}$ samples from the encoder
- 6: $\tilde{Z} \leftarrow$ A random batch of B samples from prior $p(\mathbf{z})$
- 7: $l \leftarrow \frac{1}{\sigma^2 B} \sum_{j=1}^B \|\mathbf{x}_j - \mu_{\theta}(\mathbf{z}_j)\|_2^2 + \lambda \text{MMD}_k(Z, \tilde{Z}), \mathbf{x}_j \in X_B, \mathbf{z}_j \in Z$
- 8: $\phi \leftarrow \nabla_{\phi} l$ update of encoder weights
- 9: $\theta \leftarrow \nabla_{\theta} l$ update of decoder weights
- 10: $i \leftarrow i + 1$
- 11: **end while**
- 12: **return** encoder $q_{\phi}(\mathbf{z}|\mathbf{x})$, decoder $p_{\theta}(\mathbf{x}|\mathbf{z})$

be used in order to keep the sampling from $q_{\phi}(\mathbf{z}|\mathbf{x})$ a differentiable operation. The two most common choices of k_f are the RBF $k_f(\mathbf{z}, \tilde{\mathbf{z}}) = \exp(-\gamma \|\mathbf{z} - \tilde{\mathbf{z}}\|_2^2)$, $\gamma > 0$ and inverse multiquadratics (IMQ) $k_f(\mathbf{z}, \tilde{\mathbf{z}}) = (c^2 + \|\mathbf{z} - \tilde{\mathbf{z}}\|_2^2)^{\beta}$, $c > 0, \beta < 0$ kernels. The training algorithm for a WAE with the MMD is in Alg. 4. Note that although the parameters ϕ do not appear explicitly in the overall loss function, they are present through the samples in Z .

A different architecture arises when the **Jensen–Shannon divergence** D_{JS} [169] is used in place of D_W . Again, the JSD is a symmetrical measure of distance between two probability distributions. The use of JSD leads to a model that is called the **adversarial autoencoder** (AAE) and was originally proposed in [164]. The connection between an AAE model and the general formulation (3.18) was shown in [163]. To regularize the encoder, we add a discriminator $d_{\eta}(\mathbf{z}) : \mathcal{Z} \rightarrow [0, 1]$ represented by a neural network with parameters η . The discriminator has a similar function to the one in the GAN model from Sec. 3.1. It tries to recognize latent space samples produced by the encoder and those sampled from the prior $p(\mathbf{z})$. The difference is that here, the discriminator operates on the latent space \mathcal{Z} instead of the data space \mathcal{X} .

A modified loss (3.3) is used to train the discriminator, while the loss function (3.2) is used in place of the general Wasserstein distance in (3.18) for the training of the encoder and decoder. Explicitly,

$$\mathcal{L}_{\text{AAE}_d}(\mathbf{z}, \tilde{\mathbf{z}}, \eta) = -\ln d_{\eta}(\mathbf{z}) - \ln(1 - d_{\eta}(\tilde{\mathbf{z}})), \quad (3.20)$$

$$\mathcal{L}_{\text{AAE}}(\mathbf{x}, \mathbf{z}, \tilde{\mathbf{z}}, \theta, \phi) = \frac{1}{\sigma^2} \|\mathbf{x} - \mu_{\theta}(\mathbf{z})\|_2^2 - \lambda \ln d_{\eta}(\tilde{\mathbf{z}}), \quad (3.21)$$

where $\lambda > 0$, $\mathbf{z} \sim q_{\phi}(\mathbf{z}|\mathbf{x})$, $\tilde{\mathbf{z}} \sim p(\mathbf{z})$. Note that the loss (3.21) has implicit functional dependence on ϕ through the samples \mathbf{z} . A schematic of the AAE model is in Fig. 3.7 and the AAE training procedure is described in Alg. 5. Again, any prior $p(\mathbf{z})$ that we

3.2 VAE-based models

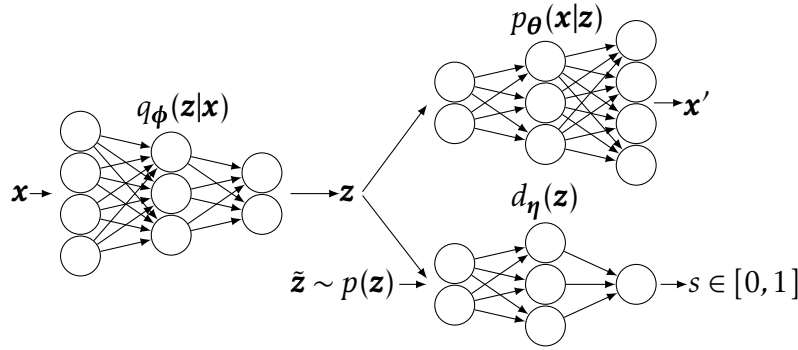


Figure 3.7: A schematic of an AAE model consisting of fully connected layers. A data sample \mathbf{x} is mapped to latent space representation $\tilde{\mathbf{z}}$ via the encoder $q_{\phi}(\mathbf{z}|\mathbf{x})$. Also, a sample \mathbf{z} is sampled from the latent prior $p(\mathbf{z})$. Both \mathbf{z} and $\tilde{\mathbf{z}}$ are passed to the discriminator $d_{\eta}(\mathbf{z})$ that produces a score s – the probability that the input sample comes from the prior. At the same time, the latent representation is passed to the decoder $p_{\theta}(\mathbf{x}|\mathbf{z})$ which maps it to a reconstruction \mathbf{x}' .

Algorithm 5 AAE training procedure.

Require: An AAE model with encoder $q_{\phi}(\mathbf{z}|\mathbf{x})$, decoder $p_{\theta}(\mathbf{x}|\mathbf{z})$, a prior $p(\mathbf{z})$ and a discriminator $d_{\eta}(\mathbf{z})$, training set $X = \{\mathbf{x}_1, \mathbf{x}_2, \dots, \mathbf{x}_n\} \subset \mathcal{X}$, maximum number of iterations $I \in \mathbb{N}$, batchsize $B \in \mathbb{N}$, regularization coefficient $\lambda > 0$, standard deviation parameter $\sigma > 0$.

- 1: $\phi, \theta, \eta \leftarrow$ Initialize parameters
 - 2: $i \leftarrow$ Iteration counter
 - 3: **while** $i < I$ or ϕ, θ, η are not converged **do**
 - 4: $X_B \leftarrow$ A random batch of B samples from X
 - 5: $Z \leftarrow \{\mathbf{z}_j \sim q_{\phi}(\mathbf{z}|\mathbf{x}_j), \mathbf{x}_j \in X_B\}$ samples from the encoder
 - 6: $\tilde{Z} \leftarrow$ A random batch of B samples from prior $p(\mathbf{z})$
 - 7: $\tilde{X} \leftarrow \{\tilde{\mathbf{x}}_j \sim p_{\theta}(\mathbf{x}|\tilde{\mathbf{z}}_j), \tilde{\mathbf{z}}_j \in \tilde{Z}\}$ generated samples
 - 8: $l_{ae} \leftarrow \frac{1}{B} \sum_{j=1}^B \mathcal{L}_{AAE}(\mathbf{x}_j, \mathbf{z}_j, \tilde{\mathbf{z}}_j, \theta, \phi)$, $\mathbf{x}_j \in X_B, \mathbf{z}_j \in Z, \tilde{\mathbf{z}}_j \in \tilde{Z}$
 - 9: $l_d \leftarrow \frac{1}{B} \sum_{j=1}^B \mathcal{L}_{AAE_d}(\mathbf{z}_j, \tilde{\mathbf{z}}_j, \eta)$, $\mathbf{z}_j \in Z, \tilde{\mathbf{z}}_j \in \tilde{Z}$
 - 10: $\phi \leftarrow -\nabla_{\phi} l_{ae}$ update of encoder weights
 - 11: $\theta \leftarrow -\nabla_{\theta} l_{ae}$ update of decoder weights
 - 12: $\eta \leftarrow -\nabla_{\eta} l_d$ update of discriminator weights
 - 13: $i \leftarrow i + 1$
 - 14: **end while**
 - 15: **return** encoder $q_{\phi}(\mathbf{z}|\mathbf{x})$, decoder $p_{\theta}(\mathbf{x}|\mathbf{z})$, discriminator $d_{\eta}(\mathbf{z})$
-

can sample from is suitable for the regularization of AAE, even a multimodal one. In practice, an AAE model compared to a WAE behaves similarly as a GAN compared to a VAE. The adversarial loss leads to less blurry reconstructions and generated samples at the cost of higher training instability [163]. One way to gain advantages of both is to use an AAE architecture as depicted in Fig. 3.7 and add the MMD regularization term (3.19) to the loss (3.21).

The single-mode prior $p(\mathbf{z})$ of the VAE model stimulates the distribution $q_\phi(\mathbf{z}|\mathbf{x})$ to have a single mode as well, and therefore it is hard to fit data with a multi-modal latent distribution. The publication [170] proposes a learnable multimodal **Vamp** prior realized as a mixture of $K \in \mathbb{N}$ independent Gaussian components. However, the Vamp prior is not compatible with the basic VAE model since its use does not lead to an analytical expression of the KLD (3.12). Fortunately, we have just described two alternatives that only require samples from the prior and which are viable with Vamp. The parameters of the components of the mixture can be then learned together with the parameters of the model. We will present some experiments with this prior in Chapter 4.

3.2.3 Generative autoencoders in anomaly detection

Anomaly scores

The likelihood function (3.7) constitutes the ideal anomaly score. Some training losses such as ELBO (3.11) were designed as approximations of the likelihood and can thus be used as anomaly scores. However, this interpretation is not so clear for other training losses, i.e. (3.18) or (3.21), hence these models were proposed for anomaly detection with separately defined anomaly scores. Nevertheless, many scores are interchangeable, giving rise to another degree of freedom (hyperparameter) for the use of autoencoders in anomaly detection. A common score is based on the first term in the loss (3.10) i.e. a Monte Carlo estimate of the expectation of conditional log-likelihood over the encoder $-\mathbb{E}_{q_\phi(\mathbf{z}|\mathbf{x})}[\ln p_\theta(\mathbf{x}|\mathbf{z})]$, which is in the case of an isotropic Gaussian decoder equal to

$$s_{\text{rs}}(\mathbf{x}) = \frac{1}{\sigma^2 L} \sum_{l=1}^L \|\mathbf{x} - \boldsymbol{\mu}_\theta(\mathbf{z}^l)\|_2^2. \quad (3.22)$$

This score, called the **sampled reconstruction error**, was shown in [131] to be more accurate than evaluating (3.7) by sampling \mathbf{z} from the prior $p(\mathbf{z})$, which is equal to computing $-\mathbb{E}_{p(\mathbf{z})}[\ln p_\theta(\mathbf{x}|\mathbf{z})]$. Further simplification is based on replacing samples from the encoder by its mean $-\ln p_\theta(\mathbf{x}|\boldsymbol{\mu}_\phi(\mathbf{x}))$ and therefore avoiding sampling, yielding the **common reconstruction error** score

$$s_{\text{rm}}(\mathbf{x}) = \|\mathbf{x} - \boldsymbol{\mu}_\theta(\boldsymbol{\mu}_\phi(\mathbf{x}))\|_2^2. \quad (3.23)$$

The usage of (3.23) is justified by the assumption that taking the mean at the encoder should approximate (3.22) while having lower computational demands. However, as we show in some of the experiments in Chapter 4, the score (3.22) performs generally better.

For adversarial autoencoders, these simplifications can be combined with the discriminator score [23, 150],

$$s_{\text{ad}}(\mathbf{x}) = \alpha s_{\text{rs}}(\mathbf{x}) + (1 - \alpha) d_\eta(\boldsymbol{\mu}_\phi(\mathbf{x})), \alpha \in [0, 1]. \quad (3.24)$$

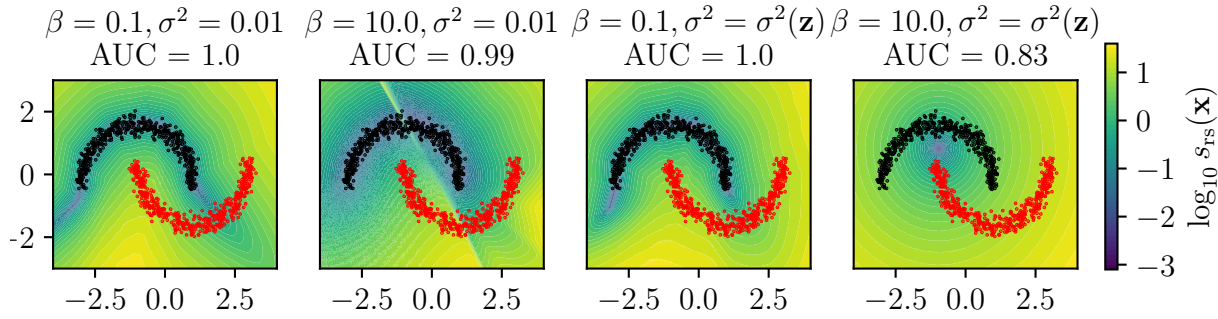


Figure 3.8: Anomaly detection with a VAE trained with the (3.17) objective on the *two bananas* dataset with a varying value of β and different way of treating the decoder variance σ^2 , where it is either considered fixed or it is subject to optimization and functionally dependent on the latent encoding \mathbf{z} . The contours of the anomaly score (3.22) are shown.

The use of the score (3.22) is demonstrated in Fig. 3.8. In the plot, the difference between a fixed and estimated decoder variance is explored again, similarly to Fig. 3.6. It is again shown that over-parametrizing the model might lead to undesired behaviour, as in the rightmost subplot, where the VAE collapsed into a single-modal Gaussian distribution.

The reconstruction error-based anomaly scores were criticized in [171] for not capturing the true data density $p(\mathbf{x})$. The proposed replacement is based on the orthogonal decomposition of the data into $\mathbf{x} = \mathbf{x}' + \mathbf{e}^\perp$ where the \mathbf{x}' lies in the tangent space of to the manifold defined by the decoder and \mathbf{e}^\perp is the orthogonal noise. This allows for a decomposition of the marginal likelihood into a product of two orthogonal parts

$$p(\mathbf{x}) \approx p'(\mathbf{x}')p(\mathbf{e}^\perp), \quad (3.25)$$

where $p(\mathbf{e}^\perp)$ is the reconstruction error term, e.g. (3.22), and $p(\mathbf{x})'$ is obtained through transformation of variables, see Sec. 5.2.1 for more details. The calculation of (3.25) is however quite computationally expensive, as it needs to compute the singular value decomposition of a Jacobian.

Practical examples

In this section, we give an overview of the current state-of-the-art in VAE-like models in anomaly detection. First, the reason for using the VAE model instead of a reconstruction error of AE is the improved generalization that was described in the previous section. It is discussed in [172] that a VAE model is equivalent to a non-linear robust PCA model and is proficient at dismissing sparse outliers. The authors also make note of the fact that VAE is very efficient in pruning unnecessary latent dimensions in the case when the real latent structure has a lower dimension than the chosen VAE latent space.

In [131] the authors present a so-called **DonutVAE** model with an enhanced loss function to detect anomalies in times series data. The architecture is similar to that of a vanilla VAE, but the training loss (3.15) is modified to consider the nature of the time

series data. The authors then show that usage of this loss function improves overall results. This however has a caveat – known anomalous samples must be available, otherwise the proposed loss is the same as (3.15). Furthermore, the authors claim that using reconstruction probability (3.22) can be seen as a weighted kernel density estimate. A similar problem is solved in [173], where a VAE model coupled with an LSTM recurrent neural network with an attention mechanism is used for detection of anomalies in time series. Again, the model operates in the semisupervised setting, and it is able to capture the temporal structure in the data.

In the self-adversarial Variational Autoencoder (adVAE) [174], an encoder-decoder pair is augmented with a transformer [175], whose goal is to simulate anomalies during training. A seeming flaw of the model is that it is trained only on normal data, and there is no link between the real and the simulated anomalies, even though the authors claim its superiority over a number of well-known competing methods. The sampled reconstruction error 3.22 is used as an anomaly score.

A variant of AAE is used in [153] where it is benchmarked on the MNIST problem. Standard normal distribution prior is compared to a Gaussian mixture model (GMM) latent prior and a special rejection component is introduced for the representation of anomalies. In [176] the AAE model is compared to VAE on the task of detection of brain abnormalities in MRI images. The loss function of the autoencoding part is enhanced by a term $\gamma\|\mathbf{z} - \mathbf{z}'\|$, $\gamma > 0$, where \mathbf{z} is a latent representation of a sample \mathbf{x} and \mathbf{z}' is the latent representation of the reconstructed sample \mathbf{x}' , which is supposed to improve consistency of the representation. The thesis [177] also uses AAEs for the detection of abnormalities in videos. The model presented in [171] uses an additional discriminator on top of the decoder in AAE to improve its reconstruction and generative properties. The model is then tested for anomaly detection on standard benchmark datasets.

Despite its name, GANomaly [178, 179] is more related to adversarial autoencoders than to GANs. It consists of an encoder-decoder-encoder architecture with a discriminator, similar to an AAE. The anomaly score is the difference between latent representations of a sample after the first and second encoding. An upgrade to this model, skip-GANomaly [180], uses skip connections in a U-Net type architecture. Here, the anomaly score is a combination of the reconstruction error and feature-matching loss.

Another way of using generative autoencoders for anomaly detection is to combat the **curse of dimensionality** by employing their ability to produce a low-dimensional representation of high-dimensional data that preserves the important relations between individual observations. Then, an anomaly detection model (be it a generative or a classical one) can be trained on the data encoded in the latent space. This **two-stage** approach is especially useful when the target domain is image data. The usage of this technique will be demonstrated in an experiment in Section 3.4. It has also been used in many publications [181, 182, 38, 17]. In [183], both stages are a VAE and the second stage has the same input and latent space dimensionality (therefore it does not compress data at all). Although this paper does not present an application in anomaly detection, it shows an improvement in learning of the latent space prior. The authors of [75] couple an ordinary autoencoder with a Gaussian mixture model represented by a neural network. The AE reduces the problem dimension to help overcome the curse of dimensionality, while the GMM model serves as a density estimate in the latent space. Both the autoencoder and the GMM model are learnt jointly which improves the performance of the model. Secondly, the input of the GMM model is not only the

3.3 Normalizing flows

latent representation, but also the reconstruction error of the sample. Although this model is not based on VAE, the proposed loss function can be viewed as being similar to the general form (3.18), as it imposes a structure on the distribution of encodings.

In [38], the model optimizes the projection of data (by virtue of NNs) to a new space, where they can be easily enclosed in a sphere of minimum radius. The approach presented in [17, 182] explicitly splits the creation of the detector into two parts. It first trains a VAE (and its variants), and then it fixes the encoder. The anomaly score is calculated by a kNN [17] or by OC-SVM [182] detectors in the latent space, obtained by projecting the sample by the fixed encoder. The two-stage models can also be viewed as a kNN with a trained metric or OC-SVM with a trained kernel. The embedding can be optimized differently, for example, by enforcing the margin between anomaly candidates and normal data as done in the REPEN [83] method, which uses an ensemble of 1NN detectors as the second stage.

3.3 Normalizing flows

Generative models that are based on **normalizing flows** aim to model the data distribution $p(\mathbf{x})$ in a general and expressive manner. While GANs do not explicitly consider a model for $p(\mathbf{x})$ and only build a proxy (generator) that enables sampling, VAEs instead optimize a posterior $p_\theta(\mathbf{x}|\mathbf{z})$ through a lower bound on the data log-likelihood. In this regard, normalizing flows are the most exact in handling the data distribution. This is at the cost of some requirements that need to be followed when building and training a normalizing flow model that will be described in the following text. Normalizing flows have been used to model complex probability distributions in multiple publications [34, 184, 185, 186]. Since the exact log-likelihood of a new sample is readily available when using a normalizing flow model, they have been applied to anomaly detection tasks in [134, 135, 187, 188, 189].

Generally, a normalizing flow is a transformation $f_\nu : \mathcal{Z} \rightarrow \mathcal{X}$ that can be used to express a data sample $\mathbf{x} \sim p(\mathbf{x})$ as

$$\mathbf{x} = f_\nu(\mathbf{z}), \mathbf{z} \sim p(\mathbf{z}), \quad (3.26)$$

where $p(\mathbf{z})$ is the prior which has some desirable properties. The defining property of normalizing flow models that differentiates them from VAEs and GANs is that the transformation f_ν must be invertible, and both f_ν and f_ν^{-1} must be differentiable. This means that the dimension of \mathbf{x} and \mathbf{z} must be the same, so here we assume $\mathcal{Z} = \mathcal{X} = \mathbb{R}^d$. Therefore, from (3.26) and the formula for the change of variables, we have

$$p(\mathbf{x}) = p(\mathbf{z}) \left| \frac{\partial f_\nu(\mathbf{z})}{\partial \mathbf{z}} \right|^{-1} = p(f_\nu^{-1}(\mathbf{x})) \left| \frac{\partial f_\nu^{-1}(\mathbf{x})}{\partial \mathbf{x}} \right| \quad (3.27)$$

which contains the determinant of the square Jacobian matrix. In practice, the normalizing flow f_ν is implemented as a neural network with weights ν . Notice that since it is fully invertible, we do not need an encoder-decoder pair like in a VAE. Again, like in the case of the vanilla VAE and GAN models, the prior might be e.g. $\mathcal{N}(0, \mathbf{I})$. Thanks to (3.27), the model can be directly optimized using the log-likelihood $-\ln p(\mathbf{x})$. When properly trained, it is possible to use a normalizing flow model to generate new samples using (3.26) or evaluate its density using (3.27), which is the basis for anomaly detection.

One can see the transformation f_{ν} as a process of reshaping the space \mathbb{R}^d in order for $p(\mathbf{z})$ to closely fit $p(\mathbf{x})$. This process is commonly broken down into incremental steps described as a series of $K \in \mathbb{N}$ elementary invertible operations (flows)

$$f_{\nu} = f_{\nu,K} \circ f_{\nu,K-1} \circ \dots \circ f_{\nu,1} \quad (3.28)$$

which are composed together to form the full normalizing flow. This gives the model its name, as we can observe the "flow" of transformed variables

$$\mathbf{z}_k = f_{\nu,k}(\mathbf{z}_{k-1}), k \in \hat{K}, \mathbf{z}_0 = \mathbf{z}, \mathbf{z}_K = \mathbf{x}. \quad (3.29)$$

From (3.27), we can express the normalizing flow objective as

$$\mathcal{L}_f(\mathbf{x}, \nu) = -\ln p(\mathbf{x}) = -\ln p(\mathbf{z}) + \sum_{k=1}^K \ln \left| \frac{\partial f_{\nu,k}(\mathbf{z}_{k-1})}{\partial \mathbf{z}_{k-1}} \right|, \quad (3.30)$$

where the inverse evaluation in the direction from \mathbf{x} to \mathbf{z} is given by $\mathbf{z}_{k-1} = f_{\nu,k}^{-1}(\mathbf{z}_k)$. As mentioned earlier, this is used to train a normalizing flow model and is also a well-suited anomaly score.

The different flow models vary in the way the individual transformations $f_{\nu,k}$ are constructed and trained, which is largely dependent on their application. In the **Non-linear Independent Component Estimator** (NICE) [34], each individual flow is called an **additive coupling layer**, which is an operation that splits the input \mathbf{z}_{k-1} into two halves along its dimensions. The first half $\mathbf{z}_{k-1,1}$ remains unchanged and the second $\mathbf{z}_{k-1,2}$ undergoes a transformation using a parametrizable function m_{ν} , which is a simple fully connected neural network with ReLU activations. Therefore

$$\mathbf{z}_{k,1} = \mathbf{z}_{k-1,1} \quad (3.31)$$

$$\mathbf{z}_{k,2} = \mathbf{z}_{k-1,2} + m_{\nu}(\mathbf{z}_{k-1,1}), \quad (3.32)$$

and the reverse operation is

$$\mathbf{z}_{k-1,1} = \mathbf{z}_{k,1} \quad (3.33)$$

$$\mathbf{z}_{k-1,2} = \mathbf{z}_{k,2} - m_{\nu}(\mathbf{z}_{k,1}), \quad (3.34)$$

which is differentiable since m_{ν} is differentiable and its jacobian is easily computed. The **Real-valued Non-Volume Preserving** (RealNVP) [190] is based on the NICE model and uses an **affine coupling layer**, where the second half of input dimensions undergo a scale-and-shift transformation

$$\mathbf{z}_{k,1} = \mathbf{z}_{k-1,1} \quad (3.35)$$

$$\mathbf{z}_{k,2} = \mathbf{z}_{k-1,2} \odot \exp(s_{\nu}(\mathbf{z}_{k-1,1})) + t_{\nu}(\mathbf{z}_{k-1,1}), \quad (3.36)$$

where $s_{\nu}, t_{\nu} : \mathbb{R}^d \rightarrow \mathbb{R}^{d/2}$ are again represented by neural networks. The reverse operation for the second input is

$$\mathbf{z}_{k-1,2} = (\mathbf{z}_{k,2} - t_{\nu}(\mathbf{z}_{k,1})) \odot \exp(-s_{\nu}(\mathbf{z}_{k,1})). \quad (3.37)$$

The **Glow** [191] demonstrates the applicability of normalizing flows to image data, which is otherwise a very difficult domain. The flow used in this model consists of

3.4 Anomaly detection with generative models: practical example

invertible 1×1 convolutions and it is demonstrated to be able to generate realistic images of faces. Some normalizing flow models use an autoregressive constraint [185] to represent the flow of information from the prior to the data distribution. The most prominent is the **Masked Autoregressive Flow** (MAF) [192]. A promising class of **Sum-product-Transform Networks** (SPTN) [188] combines normalizing flows with a graphical model. For a more complex overview and introduction to generative models based on normalizing flows, see [193, 194].

Although there are some applications of normalizing flows to anomaly detection [195, 196, 197, 198], they are less popular than different autoencoding generative models. This might seem surprising, as they are at the same time praised for the theoretical exactness of the log-likelihood computation. However, it seems that matching high-dimensional, complex distributions this way is very difficult in practice and requires normalizing flow models with hundreds of flow levels. Thus, they are very slow to train on complex data, which is also due to the requirement $\dim(\mathcal{Z}) = \dim(\mathcal{X})$. The Glow model requires 200 million parameters optimized over 13,000 GPU-hours to achieve similar performance to computationally much less expensive alternatives [191]. Still, normalizing flows present a very interesting branch of generative modeling.

3.4 Anomaly detection with generative models: practical example

In this section, an application of generative modelling on a practical example is presented. It was previously published in [17]. Some of the different generative autoencoders presented in Sec. 3.2 will be used to model data measured in a complex scientific experiment. Apart from the comparison of the previously presented anomaly scores, consider this to be a preliminary exploration of the two-stage modeling approach to anomaly detection described at the end of Sec. 3.2.3, where an autoencoding model is used to create a meaningful low-dimensional representation of complex data, and which is then coupled with some classical detector from Sec. 2.2. The same concept will also be further explored in Chapter 5.

3.4.1 The application problem

As already mentioned in the introductory chapter, physics has recently enjoyed an influx of very large amounts of data [199, 200] that needs to be processed and most importantly, from which new scientific discoveries may be extracted. This is also true for the field of plasma fusion, which pursues the goal of controlling a fusion reaction as a clean and almost inexhaustible source of energy. The ITER project [201], which is going to be one of the largest and most complicated scientific experiments in history, is expected to produce up to 2 petabytes of data every day. This naturally calls for automatic processing of the data for a multitude of tasks, including anomaly detection. Currently, tokamaks are state-of-the-art devices for experiments with controlled plasma fusion. In this section, an anomaly detection problem that appears during the operation of the COMPASS [202] tokamak will be dissected.

During the operation of COMPASS, **Alfvén eigenmodes** [203, 204, 205] were observed. Alfvén eigenmodes are magnetic instabilities that degrade the performance of the tokamak and possibly endanger the plasma-facing components of the magnetic

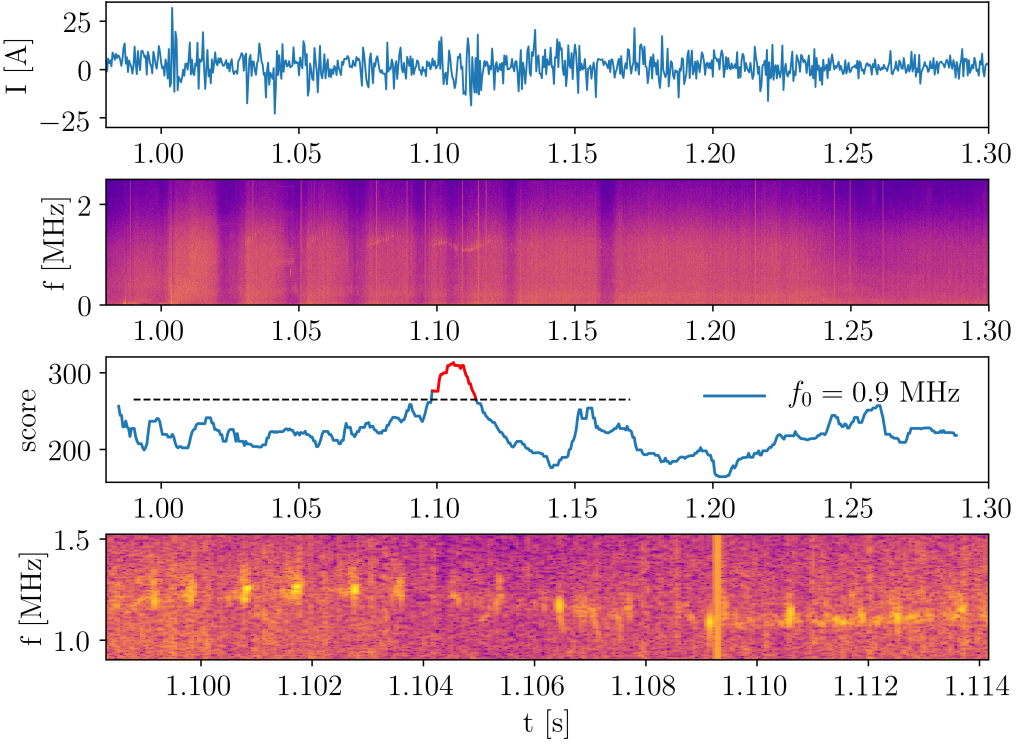


Figure 3.9: COMPASS shot 10870. Raw U-probe signal is in the upper plot. The corresponding spectrogram is below that. The score is the output of one of the tested models over the spectrogram at $f_0 = 0.9$ MHz and it is plotted third from the top. The highest peak around 1.1s corresponds to a detected chirping mode. A close-up of the spectrogram part containing the chirping mode as detected from the red part of the score plot is at the bottom. The size of the close-up is 128×311 pixels.

chamber [206]. For this reason, their automatic detection is very important. Also, it may offer an opportunity for the study of their interactions with high-energy particles present in the plasma during an experiment. On COMPASS, chirping Alfvén eigenmodes are estimated to appear in about 0.1% of all experiments. The primary means of their identification is a manual inspection of spectrograms drawn from the signal of certain magnetic probes, which is very time-consuming. See Fig. 3.9 for an example of the measured signal, a spectrogram that is derived from it, and a detected chirping Alfvén eigenmode. The spectrograms such as the one in Fig. 3.9 are large, so they are divided into patches of 128×128 pixels which is a feasible input size for current convolutional neural network architectures. It is also enough to capture most of a typical chirping mode as can be seen in the bottom plot in Fig. 3.9. The patches that contain a chirping Alfvén eigenmode are considered to be anomalies. There are 370 labeled examples of patches with a chirping Alfvén eigenmode and a large database containing 33000 unlabeled (but considered normal) patches. This is a typical anomaly detection problem, where labeled anomalies are only used for evaluation and comparison of different models and the training dataset is considered to be anomaly-free.

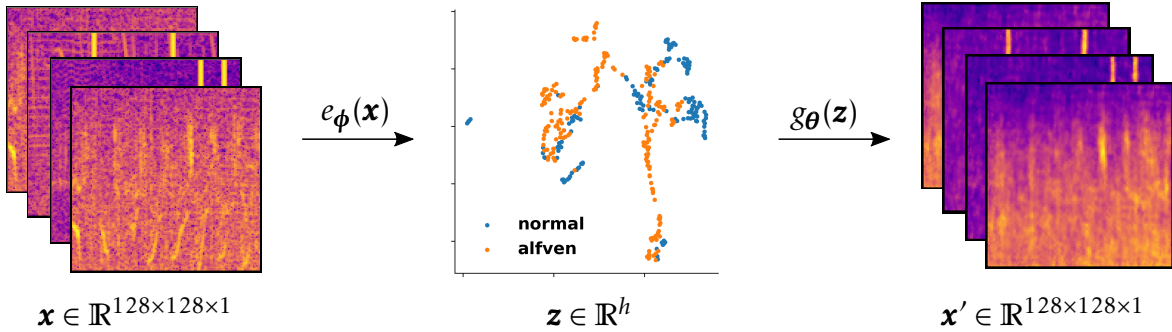


Figure 3.10: A schematic diagram of the convolutional autoencoder used for our experiments. Spectrogram patches are encoded through several convolutional, maxpooling and dense (fully connected) layers into h -dimensional vectors (here $h = 2$) and then decoded back with transposed convolutions and upscaling layers.

3.4.2 The experimental setup

Two basic experimental setups are tested in this section. Both are based on generative autoencoders from Sec. 3.2. The basic models have similar architectures, but they differ in the probability divergences used to regularize the latent space. The KLD (3.12) of a VAE model is compared against the MMD (3.19). A WAE model with a discriminator is regularized by JSD which results in the training losses (3.20) and (3.21). Finally, a plain AE from Sec. 2.2.4 is included to verify that a regularized latent space is useful. The individual components of the models (encoders, decoders, discriminators) are represented by neural networks with convolutional architecture. This is the most often used architecture for image data, as several levels of convolution operations are designed to capture shift-invariant features at different scales of an image. For more technical details on the construction of the models, see [17]. A schematic of a prototypical model is in Fig. 3.10. The models have Gaussian encoders and decoders. The prior is either $\mathcal{N}(0, I)$ or Vamp, as described in Sec. 3.2.2, and the choice is treated as a hyperparameter. Note that Vamp is only possible to use with the MMD or JSD metrics or their combination.

In the first setup, the described models are compared against each other as primary anomaly detectors in the **one class** setting. This means that they are trained on the (assumed) normal spectrogram patches and the anomaly score is the sampled reconstruction error (3.22) in case of probabilistic autoencoders, and the reconstruction error (2.19) in case of the plain autoencoder model. This will test the proposed robustness of generative autoencoders.

In the second setup, the encoding capabilities of generative encoders are leveraged to create uncorrelated low-dimensional representations of spectrogram patches. This is combined with a classifier in a combined **two-stage** model. The first stage is a convolutional generative autoencoder trained with unlabeled data. Through the use of MMD or J_{SD} measures and Vamp, a separation of the encoded data into clusters that contain similar inputs can be enforced, which makes the task of the classifier easier. The second stage is a classifier that is trained on encoded labeled data. Two different classifiers were tested. The kNN classifier, which is similar to the kNN anomaly detector described in Sec. 2.2.2, and where the score of a sample is the average label of its

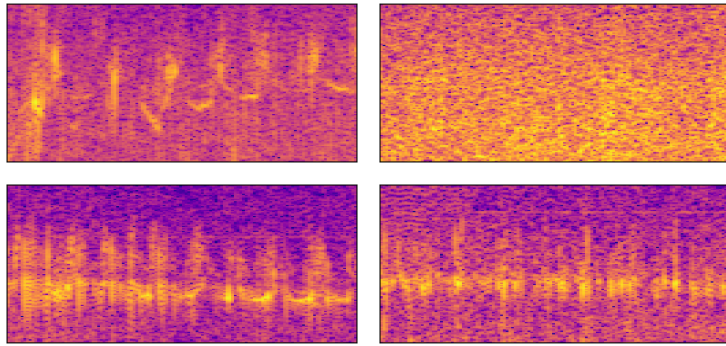


Figure 3.11: Examples of spectrogram patches identified as containing a chirping mode.

k -nearest neighbors, assuming that the label $y \in \{0, 1\}$ is zero for normal samples. The GMM classifier with M components was fitted on the latent representations of both labeled and unlabeled training data. Afterward, we determine one or more components of the mixture into which the positively labeled training samples are most likely to be projected via the encoder. Then, for a new sample, the score is the (average) log-likelihood of the sample in the anomalous components.

For more details on model architecture and hyperparameters used in the experiments, see [17]. For both experimental setups, 10-fold cross-validation over different splits of training and testing data was done. In the experimental results below, the models are selected using average performance on the test set. This is not ideal, as will be shown in Chapter 4, but here the very low number of labeled anomalies would lead to nonrobust results if the proper train/validation/test split was done, which is even more pronounced by the splitting procedure described in Sec. 3.4.3.

3.4.3 Results

During the use of one of the proposed models in the production environment of the tokamak, the following workflow would be observed. A set of experiments to be analyzed would be selected. Then, the needed signals would be extracted, spectrograms computed, and divided into patches of appropriate size. These would be fed to a trained model that would produce scores to enable a ranking of the patches. Since this would produce thousands of patches and scores for each tokamak experiment, the operator would ideally only want to examine a few with the highest score. The problem is illustrated in Fig. 3.11, where the output of such a procedure using one of the best-performing models is shown. It contains 4 patches with the highest score, out of which 3 contain a chirping mode. It illustrates that even though the neural network encoding might be powerful, it is still basically a black box model and we need to be very careful in its evaluation. Because of this, we evaluate the model performance not only by AUC (2.1), and also by the precision@ n score, which is the precision at the n -highest scoring samples, and which is useful because it can be tuned to a certain n given by the operating conditions of the tokamak. Here, we use $n = 50$, which is a realistic number of samples that an operator can examine for each tokamak experiment.

Tab. 3.1 compares the performance of models in the one-class setup. The results are split by the divergence used to regularize the latent space. The difference between

3.4 Anomaly detection with generative models: practical example

divergence	AUC	precision@50
–	0.82 ± 0.03	0.86 ± 0.06
KLD	0.46 ± 0.05	0.50 ± 0.14
MMD	0.84 ± 0.03	0.90 ± 0.06
JSD	0.84 ± 0.05	0.83 ± 0.10
MMD + JSD	0.84 ± 0.01	0.87 ± 0.01

Table 3.1: Results of optimization of the one class model by the divergence used in latent space regularization. The top three values are highlighted with shading. No divergence is used in a plain autoencoder with the training objective (2.19).

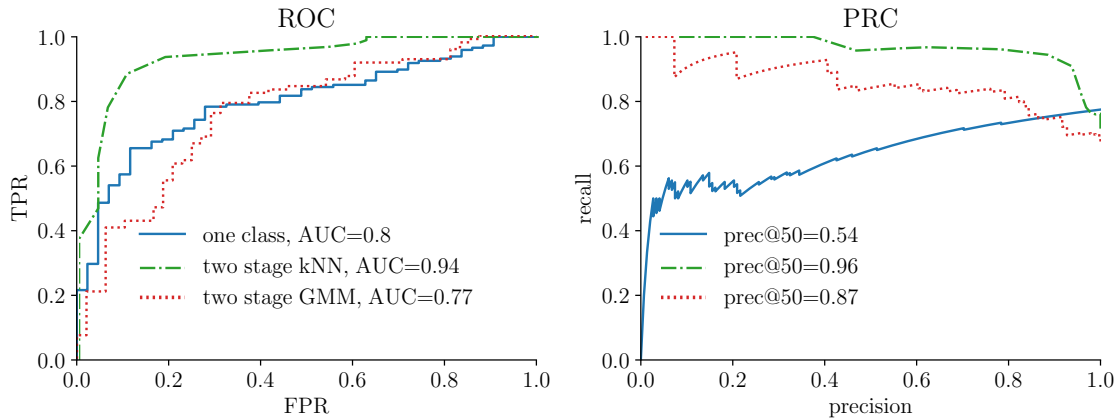


Figure 3.12: ROC and PR curves of selected models. For brevity, we include the best one-class and best two-stage models in the same plot, although they are not directly comparable.

MMD, JSD, and their combination in terms of AUC is negligible, but MMD is slightly better than the rest in terms of precision@50. Surprisingly, vanilla VAE with KLD fails in this task altogether, which indicates that the distribution of the patches with Alfvén eigenmodes is difficult to model through a latent space with an unimodal prior.

The performance of the two-stage models is summarized in Tab. 3.2. What is immediately obvious is that the simple kNN model is superior to the GMM approach with any encoding. Also, MMD regularization produces the best results. We might speculate that this might be due to the improved ability to produce a well-separated encoding enforced by the used prior. Fig. 3.12 captures the ROC and PR curves for the best one-class and two-stage models.

A question one might ask is whether the use of an autoencoder is truly necessary. In the end, we are doing a projection from $d = 128 \times 128 = 16384$ dimensional picture space into at most $h = 64$ dimensional latent space which must naturally lead to a loss of information. As shown in Fig. 3.13, where $h = 8$, the autoencoder is able to identify the difficult nonlinear correlations and improve the performance of a subsequent second-stage kNN model. The compression is clearly necessary for overcoming the curse of dimensionality which says that the L_2 distance degenerates in large dimensions. An alternative approach to overcoming the issue of large input dimension might be to train a classification convolutional neural network, which does the compression

divergence	classifier	AUC	precision@50
–	kNN	0.80±0.07	0.88±0.10
KLD	kNN	0.80±0.08	0.85±0.11
MMD	kNN	0.91±0.06	0.94±0.05
JSD	kNN	0.83±0.07	0.87±0.10
MMD + JSD	kNN	0.86 ± 0.07	0.91±0.10
–	GMM	0.75±0.06	0.80±0.10
KLD	GMM	0.74±0.06	0.83±0.11
MMD	GMM	0.66±0.12	0.72±0.12
JSD	GMM	0.74±0.06	0.82±0.11
MMD + JSD	GMM	0.76±0.06	0.84±0.10

Table 3.2: Results of hyperparameter tuning of the two-stage model across 10 cross-validation splits.

by its nature. However, such a network would be highly susceptible to overfitting since it requires a lot of labeled data that is not available.

Influence of the train/test splitting methodology

At first, the splitting of testing and training labeled patches was done on the level of patches, without any regard for the spectrogram/experiment that the patch came from. It was assumed that the labeled chirping modes are homogeneous across the spectrograms. However, this turned out not to be true. Therefore, the train/test splits were done on the level of spectrograms which were then subsequently divided into patches. See Fig. 3.13 where on the left side, the AUC curves for different values of k of the kNN model are for the case when the data split was done on the level of patches. The blue line that is the result of a kNN fit peaks at $k = 3$. On the other hand, there is no such peak on the right side of the figure, where splitting was done on the level of spectrograms. This indicates that the positively labeled patches in a single spectrogram are much more similar to each other than to those in different spectrograms, as only a relatively low number of neighbors is sufficient for optimal performance. Also, the variance of the right-side plots is much higher, again indicating larger differences across spectrograms. If we continued with the splitting on the level of patches, we would have a biased and too optimistic estimate of performance before using the framework in a production environment.

Final remarks

To sum up the findings from this section: generative autoencoders are a viable tool for unsupervised and semi-supervised anomaly detection. The information contained in the latent spaces is useful for anomaly detection, provided we have at least some examples of labeled anomalies. And finally, the kNN classifier proved to work very well in this simple experiment. All of these findings are going to be useful in the building of the model that is presented in Chapter 5.

3.4 Anomaly detection with generative models: practical example

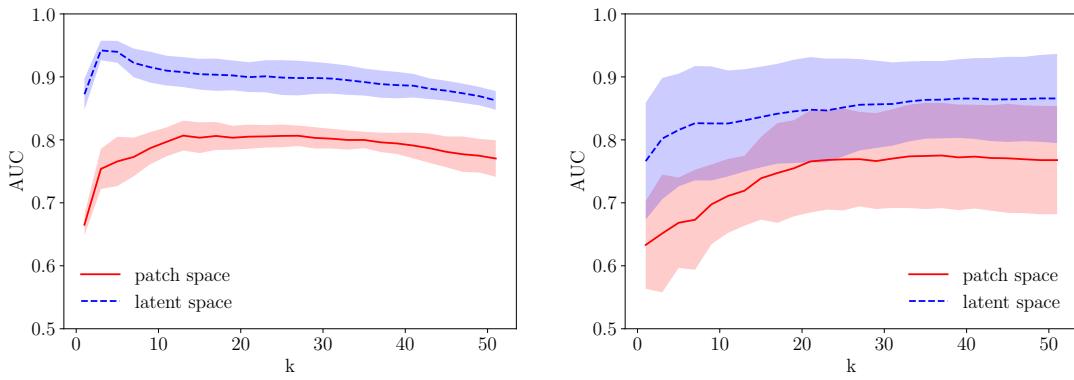


Figure 3.13: kNN fits for different values of k . The red line and band show the mean and one standard deviation bands of the resulting AUC values when kNN is fitted to the original vectorized images. The input space dimensionality is $h = 16384$. The blue dashed line and band are the same quantities for a $h = 8$ dimensional representation by a first-stage model. On the left, the training and testing splits were done on the level of individual patches, leading to improved performance and less variance. On the right, the split was done on the level of the original spectrograms, which is a more realistic scenario. The standard deviation and mean were computed from 10 random splits.

4

Empirical comparison of anomaly detectors

The practical use of anomaly detectors (as well as other machine learning models) consists of finding the right choice of algorithm and its hyperparameters that is the most suitable for the problem at hand. This usually requires a time-consuming effort of training many models and evaluating them fairly on some test data. It is not clear, however, if there is a method or a class of methods that is generally more suitable for solving certain anomaly detection problems than any other. The objective of this chapter is twofold: to provide an empirical comparison of anomaly detection methods of various paradigms with a focus on deep generative models, and to identify the sources of variability in data that have the largest influence on the suitability of a method. The methods are compared on popular tabular and image datasets and under a varying amount of anomalies available for hyperparameter optimization. This serves to establish a direction for the novel anomaly detector described in Chapter 5.

As far as anomaly detectors based on deep generative models are concerned, the number of modifications and extensions of VAE or GANs is sharply increasing (as is documented in Chapter 3), each claiming superiority over the prior art. Although almost every newly published method provides evidence of outperforming its predecessors, sometimes there are contradictory results when the same methods are included in different comparisons. This raises a suspicion that some of the methods are overspecialized or poorly tested. This chapter is inspired by the paper "Do we need hundreds of classifiers to solve real-world classification problems?" [209], and strives to compare anomaly detectors under fair conditions to observe how the field has evolved in the last twenty years — the oldest compared detector (kNN) was published in 2000. Specifically, it investigates if methods based on **deep** generative models offer a benefit over methods based on alternative paradigms, either the **shallow** methods that were introduced in Chapter 2 or deep architectures without the capability of generating samples.

There is a number of works that try to achieve a similar goal, but we have found some deficiencies (with respect to the previously stated goals) in most of them. Earlier surveys [27, 31, 28, 24] do not compare to deep generative methods because they were not developed or sufficiently popular at that time. Contrary to that, the study in [210] contains a detailed description of deep models but provides experiments only with the basic VAE and only on specialized video datasets. Ref. [62] introduces a taxonomy of deep anomaly detection models but does not compare them experimentally. Other recent surveys [58, 59, 60, 61, 211] either ignore deep generative models altogether

4.1 Anomaly Detection Contexts

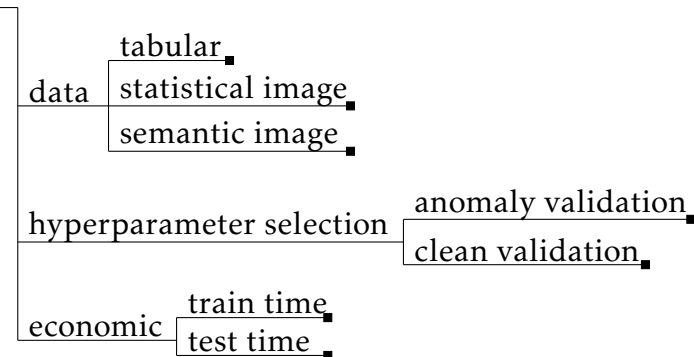


Figure 4.1: Various aspects of anomaly detection comparison forming the context of an experiment.

or describe them only theoretically, without making any experimental comparison. The most relevant prior art is [35], which tries to theoretically link deep and shallow techniques. But again, an extensive experimental comparison of different generative models is missing. One would also expect papers introducing new methods to contain such a comparison. Some of them do [24], but generally, we have found comparisons limited (e.g. using a small number of datasets or methods) or flawed, which is elaborated below.

How do we avoid the aforementioned deficiencies? First, eight shallow methods from Chapter 2 serve as a baseline, with which we compare the generative models and other state-of-the-art deep methods from Chapter 3. Second, the comparison uses a large number of tabular (40) and image (6) datasets popular in the evaluation of deep models, which are described in Appendix B. Third, all methods have been given the same conditions, which primarily means the budget for optimization of hyperparameters, as [212] has shown this to have a significant impact.

This chapter is organized as follows. In Sec. 4.1, the anomaly detection contexts that have the greatest influence on the outcome of our experiments are defined. Sec. 4.2 details the datasets, different approaches to the selection of hyperparameters, and other design decisions in the experimental setup. Sec. 4.3 discusses the experimental results and lessons we have learned. We summarize the chapter with a recommendation to practitioners and our suggestions for future work. The original paper [213], which this chapter summarizes, contains more, mainly technical details and results.

4.1 Anomaly Detection Contexts

While many practitioners are eager to see which method is the best for their application, the specifics of the application may differ. In this chapter, a large number of experiments are conducted in order to identify the main sources of variability influencing the performance of anomaly detection methods. The number of combinations of these aspects is huge. Therefore, we have chosen these key axes of variability: datasets, hyperparameter selection strategy, and economic point of view. From these axes, we select a few discrete points, on which we will provide a comparison. The particular combination of the selected aspects will be called a **context**, see Fig. 4.1 for illustration.

The first axis is the target data domain. Our experiments use two types of datasets:

tabular and **image**. This is the most obvious split, and indeed most authors of prior art test their methods on either choice of data. Another possible way to look at data is whether they contain **statistical** or **semantic** anomalies, see Sec. 1.1. Statistical anomalies should be located in areas of a low likelihood of the normal class, while semantic [52] anomalies cannot be differentiated from normal data statistically. This is because they appear in datasets with multiple sources of variations, where only some of them are considered anomalous. Such types of anomalies are most common in image datasets. The suitability of the compared methods for the dataset context axis is studied in Sec. 4.3.1.

The second axis of variability is the hyperparameter selection strategy. It should be a gold standard that the experiments are repeated on different splits of data to training, validation, and testing subsets, especially if the datasets are small. However, in most of the reviewed recent papers [151, 174, 23, 178, 133], this procedure was not mentioned with the exception of [38]. Therefore, our comparison fills this gap. Also, it is important to define the nature of information available for the selection of the hyperparameters: it is indeed a very different task if there is some (often small) number of known anomalies in the validation dataset that can be used to choose hyperparameters by cross-validation - this is the **anomaly validation** scenario. On the other hand, in the **clean validation** scenario, the validation dataset contains no anomalies. In our experience, the former case is more common. Our observations are summarised in Sec. 4.3.2.

The third axis is the economic aspect of a problem. There might be serious computational restrictions present in solving real-life problems. One might then not opt for a method that promises state-of-the-art performance, but for another that reaches slightly worse performance but can be trained economically, and its performance is robust with regard to hyperparameter optimization. This tradeoff is captured by the **train/test** computational demands of a method. More details on this can be found in Sec. 4.3.3.

4.2 Experimental setup

In order to achieve a fair and robust comparison, a strict procedure for testing each model was followed, which is briefly described in this section. For more details, see the original publication [213].

4.2.1 Data

Two criteria guided the choice of datasets (mainly the tabular ones): first, they ought to be publicly available, and second, they should appear in surveys or articles presenting new methods. We conduct experiments both on tabular (see their list in Appendix B.1) and image datasets (see Appendix B.2). In the setting of this whole work, a single class (of digits/objects) is considered normal and the rest anomalous. Therefore, one classification image dataset is transformed into ten different anomaly detection sub-datasets. Since the MNIST, FashionMNIST, MVTec-AD, and MNISTC datasets have a rich and consistent number of samples in the normal class and clear anomalies, we consider them to be statistical anomalies. On the other hand, images in the majority of classes in CIFAR10 and SVHN2 have a strong background and are thus considered

4.2 Experimental setup

class model		acronym	class model		acronym
flows	MAF	maf	two-stage	DAGMM	dgmm
	RealNVP	rnpv		DeepSVDD	dsvd
	SPTN	sptn		REPEN	rpn
	AAE	aae		VAE-kNN	vaek
	adVAE	avae		VAE-OC-SVM	vaeo
	GANomaly	gano		ABOD	abod
	skipGANomaly	skip		HBOS	hbos
	VAE	vae		IsolationForest	if
	WAE	wae		kNN	knn
	fAnoGAN	fano		LODA	loda
autoencoders	fmGAN	fmgn	shallow	LOF	lof
	GAN	gan		OC-SVM	osvm
	MOGAAL	mgal		PidForest	pidf

Table 4.1: Overview of the main classes of compared methods and the acronyms used in the text.

to contain semantic anomalies. This prior division is also supported by a different behavior of different methods as reported in the following text.

The normal data samples in each dataset were randomly split in 60%/20%/20% ratios to train/validation/test subsets, respectively. Anomalous data samples were split such that 50% were in the validation part and 50% in the testing part, which means the training subset has not contained anomalous samples.¹ The proportion of anomalies that were used in the validation phase varied from zero to the selected 50%. This was done five times to produce different folds in all tabular and small (MvTec-AD and MNIST-C) image datasets, but only once for other image datasets, as the folds would be very homogenous, see the original paper.

4.2.2 Models and their hyperparameters

Since the number of tested models is quite large, Tab. 4.1 offers their overview together with acronyms used in graphs and tables and also an orientational division of the models into separate categories. Most of the deep models were coded from scratch since the original implementations were either missing or non-functional. Properly exploring the space of hyperparameters of all models is paramount to achieving fair and comparable experimental comparison, yet this is often superficially treated. Researchers often use default or recommended values, ignoring that they are sub-optimal on datasets they use in their comparison. The conflicting results of the MOGAAL method in the original publication [151] and in [174] demonstrate our argument. Another prototypical example is OC-SVM, which is typically used with Gaussian kernel and with ν

¹A training set without any anomalies is in practice very optimistic, but this decision removes another degree of freedom from the evaluation for the sake of clarity of results.

set to some default value, e.g. 0.05 [24], but can achieve better results with different kernels. The choice of hyperparameters in anomaly detection is everything but easy. But this means that the experimental settings should be set up such that all methods have been optimized equally. We conjecture that recommended and default values of hyperparameters are strongly correlated with the choice of evaluation datasets in the publications that recommend them.

In order to explore the hyperparameter space of each method properly, we have employed a random search over a predefined grid for each method. This allows the construction of sections through the space for sensitivity studies. Moreover, it is frequently more efficient than grid search [214] and more flexible. For each model, dataset, and repetition, we sampled 100 configurations from corresponding sets of hyperparameters and trained the models with them. A fixed time budget was also given for the training of each model. This automatically penalizes complicated models, that might theoretically achieve great performance but are too computationally demanding.

A thorough exploration of the hyperparameter selection context also requires changing the criteria of model selection. When anomalies are available for validation, we select hyperparameters maximizing the AUC on the validation set. For experiments with no available anomalies, we have decided on the following hyperparameter selection mechanism. For shallow methods, we have used default hyperparameter values from literature - either the authors of the method recommended them, they were used in a survey, or are default in a given implementation. Their overview is found in [213]. For deep methods, this is unfortunately impossible since their hyperparameter space is much larger, and the values are usually tuned to a specific dataset. Therefore, to have a universal solution, we have selected the already trained and evaluated models based on the lowest average anomaly score on the clean validation data, i.e. validation data without anomalies. This approach is theoretically justified for models with proper likelihood (such as flow or VAE models), which also perform better in this scenario.

4.3 Experimental results

Unless specified otherwise, the performance results are estimates of the AUC on the testing set and averaged over all folds of the random cross-validation repetitions. When ranks are reported, they are calculated by ordering methods on each dataset and calculating the average across them (as recommended in [215]). Hyperparameters are selected using the best average performance over the folds of the validation dataset.

4.3.1 Dataset context

The results of the experimental comparison on all dataset types are presented in the form of critical difference diagrams (CDD) as recommended by Demšar [215], see Fig. 4.2. These diagrams show the average rank of detectors across the datasets together with a confidence band that indicates that a statistical test cannot reject the hypothesis that two detectors perform the same. What follows is a commentary on the influence of the datatype with respect to two types of hyperparameter selection strategies differing in the number of anomalies in the validation set as defined in Section 4.1: i) anomaly validation context, and ii) clean validation context.

4.3 Experimental results

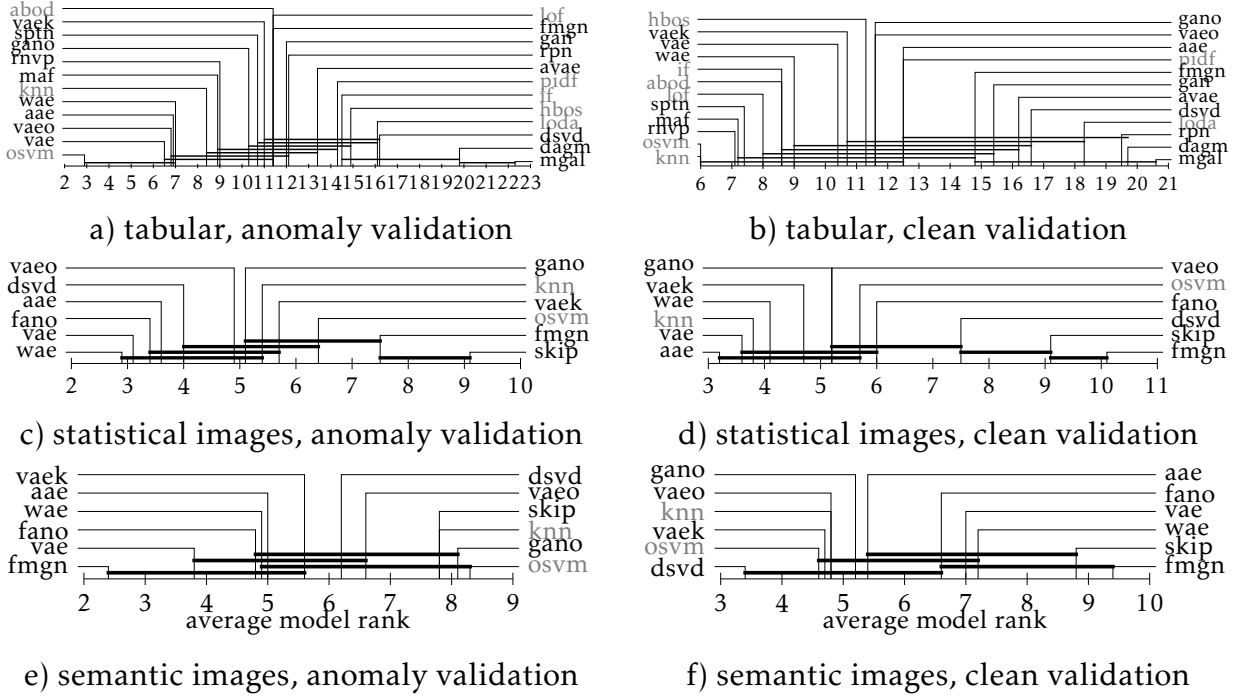


Figure 4.2: Critical difference diagram of models ranked via the test AUC. Models whose performance is statistically indistinguishable have a difference of ranks under the critical value of the Nemenyi test $CD_{0.1}$ and are joined by a horizontal band. Results are presented for different types of datasets: tabular (Top row), image datasets with statistical anomalies (Middle row), and image datasets with semantic anomalies (Bottom row); and two different hyperparameter selection cases: using anomalies in validation (left) and using clean validation (right).

Tabular data: OC-SVM performs the best, and it is *statistically better* than almost all detectors except autoencoder-based generative models and VAE combined with OC-SVM in the case of anomaly validation context. The first 11 places (roughly one half) belong to models that can be divided into three groups: (i) OC-SVM and its variants, which estimate a density level of a distribution; (ii) flow models and kNN, which estimate the pdf (un-normalized in case of kNN); (iii) and variants of autoencoders, where the reconstruction error is related to pdf as explained in Sec. 3.2. The same types of methods occupy the top positions in the clean validation context, Fig. 4.2b), however in a different order. The best is the kNN (due to the simplicity of its hyperparameters), and all other pdf-modeling methods (flows) have improved relative to the anomaly validation context. The autoencoder-based methods moved beyond shallow methods (LOF, ABOD, IF). We believe that models in the lower half of the scale in both validation contexts are not suitable for detecting statistical anomalies. We cannot explain the poor performance of MOGAAL, DAGMM, and adVAE, and we attribute it to different experimental environment. DeepSVDD was primarily implemented for image problems, where it performs relatively well.

Moreover, differences in mean ranks of many models in Fig. 4.2 are statistically insignificant at level $p = 0.1$, which is disappointing. Assuming the ranks remain the same, another 51 datasets would be needed to make the difference between OC-SVM and VAE statistically significant on tabular data with 50% anomalies. This indicates that the results are relatively noisy and can be easily changed for a different choice of

datasets.

Statistical image data: WAE and VAE models have the best average rank when evaluated on statistical image data, although their lead is not statistically significant over most of the other models as is evident from Fig. 4.2c). The autoencoder-based methods (AAE,VAE,WAE) also perform well in the clean validation context, complemented by the kNN, Fig. 4.2d).

Semantic image data: A different story is told by Fig. 4.2e) where the ranking of methods on image datasets with semantic anomalies is dominated by fmGAN by a large margin in the anomaly validation context. However, it is also the worst method in the clean validation context. In the opposite manner, OC-SVM and kNN perform very poorly in the anomaly validation context, but they are among the best in the clean validation context. The best-performing method in the clean validation context is DeepSVDD [38]. We conjecture that the performance of the fmGAN is related to the variability of its training. With a sufficient number of anomalies in the validation set, it is possible to find one trained model that fits the problem.

4.3.2 Hyperparameter selection context

The influence of the hyperparameter selection procedure on the results in the previous section is now studied in detail for a few selected methods. We choose only those that scored among the best in the previous section. First, we analyze the sensitivity of these methods to the number of anomalies in the validation set. Second, we study hyperparameter selection for two individual methods, the variational autoencoder family and OC-SVM.

Impact of the number of anomalies in the validation set

The process of hyperparameter selection described in Sec. 4.2.2 depends on the availability of examples of anomalies in the validation set (recall that it is assumed that the validation dataset does not contain unknown anomalous samples, i.e. is not contaminated). Fig. 4.3 displays the influence of the number of anomalous samples in the validation set on a finer grid between the two contexts reported before. Note that for the first point on the x-axis where the clean validation dataset was used, the mechanism of model selection was different from the rest of the graph. This is the reason for the significant difference between the clean context and the remaining points.

First, we observe that the quality of the models selected using anomalies improves with an increasing number of anomalous samples, which is expected. However, for a low number of anomalies, many methods perform significantly worse than in the case of the clean validation context. This behavior is notable across dataset types, especially for OC-SVM, and to some extent VAE. We conjecture that the hyperparameter selection procedure of those methods has a tendency to overfit, and its hyperparameters are not robust. In contrast to this, the performance of kNN, WAE, and RealNVP degrades slowly with the declining number of anomalies, which suggests that they are quite robust in difficult operating conditions. We attribute it to the fact that these methods are more exact in their estimation of data likelihood than the rest.

Second, we notice that the experimental results on the semantic image datasets are generally poor, as the AUC of the best model (fmGAN) on CIFAR10 is 0.72 and similarly on SVHN2, where the best model achieved 0.74. On the other hand, anomaly detection methods perform well on statistical image datasets. This indicates, contrary

4.3 Experimental results

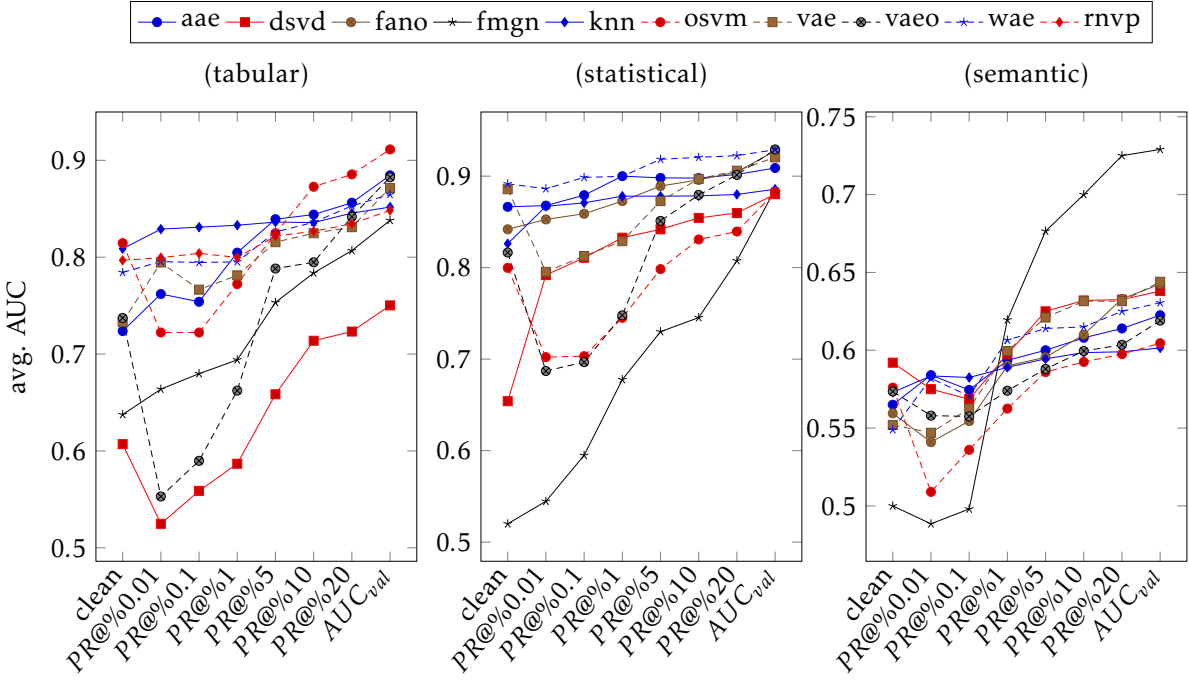


Figure 4.3: Sensitivity of methods to the number of anomalies available in the validation set for hyperparameter selection visualized in terms of the achieved AUC aggregated over all datasets in each category (columns). The clean validation context is the left-most point on the x-axis, and the anomaly validation context (50% of available anomalies) is the right-most point. The points in-between were obtained by selecting models with the highest precision on the reported portion (e.g. 5%) of validation samples with the highest anomaly scores.

to popular belief that the models fail to learn or identify the important semantic information, or they consider different semantic information anomalous, and they should be told which semantic aspect of an image should be considered as an anomaly — e.g. blurred images might be anomalous as well. Again, more detailed results, e.g. non-aggregated AUC values for individual datasets, or illustrative samples of detected anomalies can be found in the original publication [213].

A practitioner might also desire a method robust with respect to a poor choice of hyperparameters. In general, deep methods in our experiments have demonstrated higher variance, probably due to the large number of hyperparameters and stochasticity involved in their initialization and training via batched gradient optimization. In this respect, GAN-based models seem to be the least robust, which is in line with [216] stating that GANs are not directly optimized for anomaly detection. This hints at the potential cost of hyperparameter optimization — with higher performance variance, one is less likely to train a well-performing model in a given number of attempts. On the other hand, given enough labeled anomalies for hyperparameter selection, the fmGAN model gained a noticeable edge on semantic image anomalies.

The good performance of the fmGAN model on semantic anomaly data is perhaps a little surprising in light of the observations made e.g. in Sec. 3.1. There, the covering of the input space by the discriminator seems to be quite non-robust as the discriminator tends to give low anomaly scores even in places where there are no training data. Our hypothesis on why the discriminator performs well on semantic image data is that

due to the high dimension, the space is much more sparse than in the case of tabular data, and such degenerate behaviour which is observed in Fig. 3.2 then happens less frequently. Another explanation might have some connection to noise-contrastive estimation. In [221], a simple approach to anomaly detection is proposed - a logistic regression model that is trained to distinguish normal training data and samples from a uniform distribution which poses as a proxy for the distribution of anomalies. On low-dimensional problems, this approach works well, but as it requires a large volume of the input data space to be covered by samples, it soon reaches its limits. There are some similarities between this approach and the (fm)GAN model - the generator and the uniform sampler have the same role as well as the discriminator and the logistic regression model. It is possible that the generator samples the input space in such a way that fewer samples are required than in the noise-contrastive approach, as it only samples from the input space around the input training samples. Unfortunately, a proper exploration of this hypothesis is beyond the scope of this work, although a generator-discriminator pair is successfully used in Chapter 5 to detect semantic anomalies.

Sensitivity Analysis of the VAE family

The richness of the landscape of models that are based on the VAE is evident even from the relatively short overview in Sec. 3.2. These methods form a whole family with multiple sources of variability: i) approximation of the likelihood in training (loss function), ii) the choice of latent prior, and iii) the anomaly score. We will analyze the sensitivity of the results to these choices on tabular data in the anomaly validation context. We focus on this family since most of the novel deep generative models for anomaly detection are based on the autoencoder architecture, as well as the novel model that is introduced in Chapter 5. Additional degrees of freedom include the parametrization of variance of $p_{\theta}(\mathbf{x}|\mathbf{z})$, which was discussed already in Fig. 3.6. The variance can be either fixed (called VAE-constant), used in [182, 174, 179], a trainable scalar (called VAE-scalar), or a trainable full diagonal (called VAE-diagonal), used in [130, 131, 150]. In the experiments, all three variations were tested on tabular data; however, on image data, the full diagonal was skipped due to computational constraints (and in line with the prior art, where only scalar variance is used).

The overall comparison in Fig. 4.2 revealed that WAE and vanilla VAE variants perform best. The other degrees of freedom, namely richness of prior, used anomaly score, and parametrization of the variance, were treated as hyperparameters. Fig. 4.4 extends the study by showing the distribution of ranks over tabular datasets for different variants of VAE, including GANomaly and adVAE. First, notice that the spread of the method's ranks over various datasets is significant, as even ranks of the best methods vary from 3 to 15. This means that the conclusions below need to be taken with a grain of salt, as the experimental results are extremely noisy.

The ELBO-based score (3.15), -el, together with the orthogonal decomposition (3.25) of the likelihood [171], -jc, does not perform well. The sampled reconstruction error (3.22), -rs, almost always performs better than the usual reconstruction error, -rm, calculated according to (3.23). This demonstrates that the common approach of replacing the mean of the decoder with that of the encoder is inferior but computationally cheaper (see Tab. 4.2 with prediction times). The inclusion of the discriminator score in (3.24), -di, of AAE (an autoencoder combined with GAN) seems to be also on par with the sampled score (3.22).

4.3 Experimental results

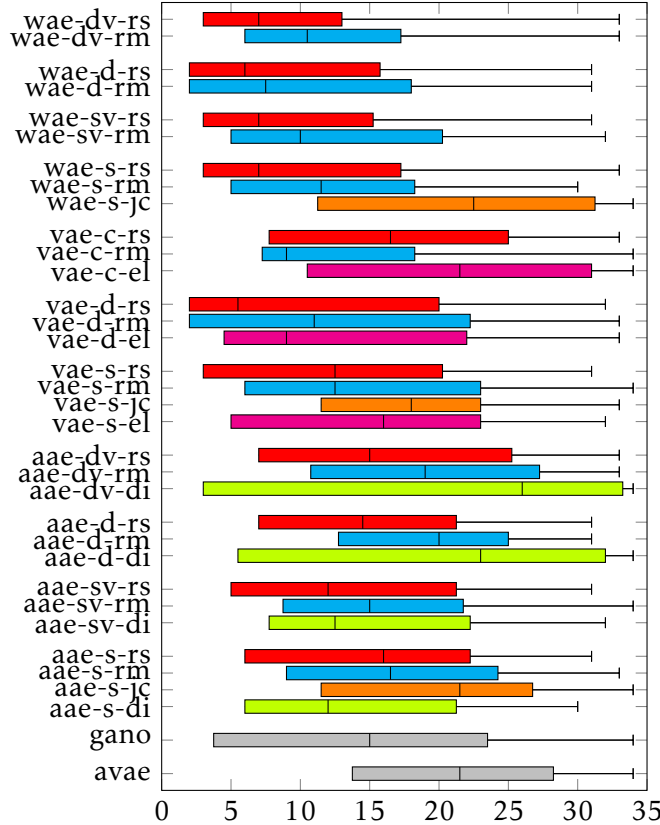


Figure 4.4: Sensitivity study of various variants of autoencoder-based methods displayed in the form of boxplots of their ranks in the AUC metric achieved on the tabular datasets. The first three letters of the method’s name denote the training loss. Models with the -d- middle part estimate the full diagonal of the decoder variance, -s- estimate only a scalar, and -c- use a fixed scalar variance as a hyperparameter. All variants are using the standard Gaussian latent model. Models using the VampPrior are denoted by extending the decoder variance symbol by the letter v-, i.e. -dv-, -sv-, -cv-. The last part of the name denotes score, -rs stands for the sampled rec. probability (3.22) with $L = 100$, -rm for (3.23), -el for the ELBO (3.15) composed of -rs and KLD, -jc for (3.25), -di for (3.24).

From the same figure, we also conclude that the models modelling the full diagonal in $p_{\theta}(x|z)$, -d-, seem to be better than the scalar, -s-, or constant, -c-, variants. This result is important, as many comparisons in the prior art use the VAE-constant, despite the version with full diagonal being discussed in the original publication [217]. It also comes as a bit of a surprise, considering that the reconstruction was of higher quality with a scalar variance in the simple experiment in Fig. 3.6.

The rich prior distribution on the latent space proposed in [170], VAMP, -v-, does not seem to give an advantage in the anomaly detection except in the AAE, although it performed quite well in the practical anomaly detection problem in Sec. 3.4. This might be due to most of the anomaly problems presented in this chapter having an unimodal distribution of normal samples, as opposed to the real-world distribution of tokamak data. Similarly, recent variants adVAE and GANomaly do not seem to perform well on the tabular data, but they were not evaluated on them in the original publications.

	vae-s-rs	vae-d-rs	vae-s-rm	vae-d-rm	vae-d-jc
\bar{t}_{pred} [s]	12.10	18.51	0.11	0.15	57.31

Table 4.2: Average prediction times on the tabular datasets for different combinations of VAE scores and decoder variance estimations. The -d- part stands for a model with an estimate of the full diagonal of the decoder variance, -s- is a scalar estimate. Sampled reconstruction error (3.22) (with $L = 10$ samples) is denoted as -rs, -rm is the anomaly score (3.23) and -jc is (3.25).

Sensitivity study of OC-SVM

This result on the optimization of OC-SVM, taken from [213], is not directly related to the main result presented in Chapter 5, but we found it interesting enough to include it in this compilation. The domination of OC-SVM on tabular data in anomaly validation context contrasts with many prior experimental comparisons [28, 218, 216, 87, 219, 174]. The search for the culprit found it to be the hyperparameter selection. This study has varied the ν parameter, kernels, and their parameters, which is much more than most of the prior art does, which is fixing the kernel to RBF and testing a few values of its width γ and ν . Inclusion of other kernels into the search for hyperparameters seems to be the major source of improvement in this case. Replacing the OC-SVM with one restricted to use only the RBF kernel and $\nu = 0.5$ yields an increase in average rank from 2.9 to 8.1 with an average decrease in performance by 0.06, measured in AUC in the anomaly validation context. This version of OC-SVM is then easily surpassed by variational autoencoders and kNN, as demonstrated in [213]. The importance of the choice of the kernel is furthermore illustrated by the fact that the sigmoid kernel was the optimal choice for 23 datasets, while the RBF kernel was optimal only for 13. Ref. [28] mentions that setting $\nu = 0.5$ provides universally good results, which may be the reason why many authors do not tune it. In theory, it should be set to much lower values ($\nu = 0.05$) corresponding to the presumed low ratio of anomalies in data, but with Bayesian optimization, we found that the best estimate of ν was in some cases even higher, such as ~ 0.75 on the statlog-vehicle dataset.

4.3.3 Economic context

Practitioners ask for fast and accurate algorithms, but these two features rarely go hand in hand, and a decision on a trade-off has to be made. When one plots model performance against computational intensity, the interesting methods lie on the Pareto frontier [220], as in the absence of an external factor, a rationally behaving practitioner does not have the motivation to choose a different model.

Fig. 4.5a-left shows the trade-off between accuracy and training time for tabular data, where the absolute numbers were replaced by average ranks for robustness. The Pareto frontier contains two methods, which are OC-SVM and kNN. The position of OC-SVM is rather surprising, as its training time is known to scale poorly (quadratically) with respect to the number of samples, but it is caused by most of the tabular datasets being small. Different results may arise for a dataset with many data records. Fig. 4.5a-right shows a similar trade-off between accuracy and testing (inference) time. OC-SVM is still on the Pareto frontier, but it is expensive, as the complexity grows linearly in the number of samples. The fmGAN, GAN, and DAGMM methods are there

4.3 Experimental results

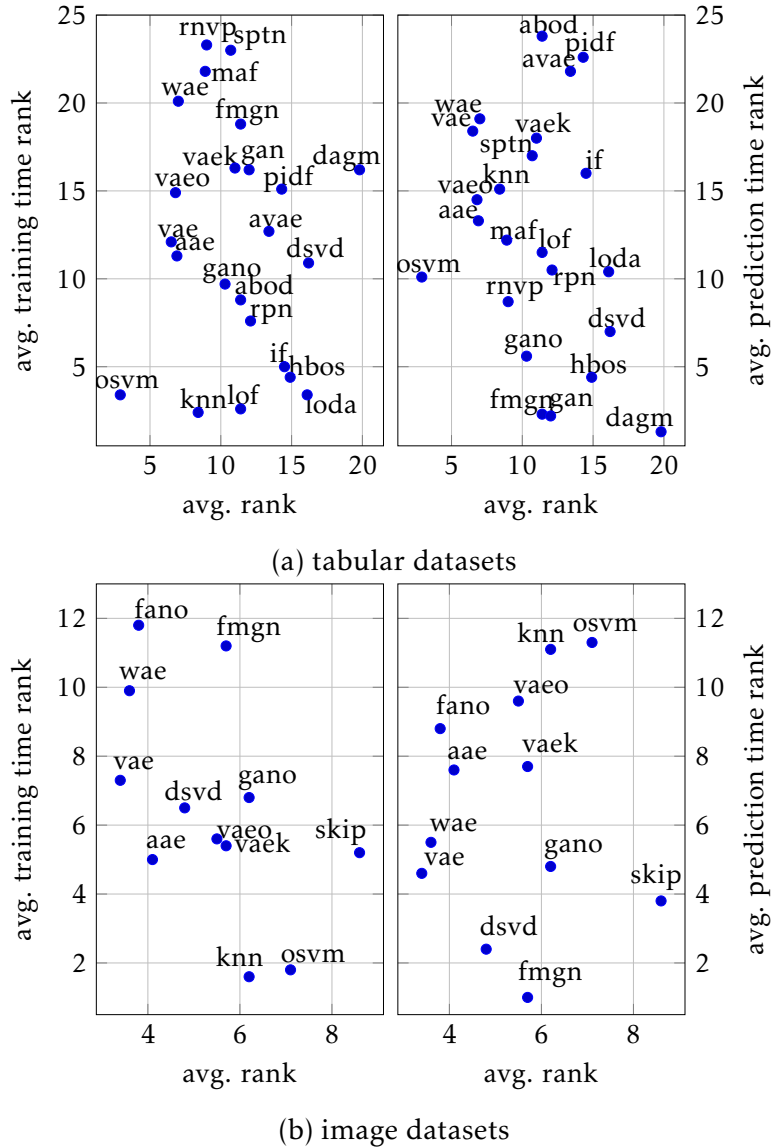


Figure 4.5: Scatter-plots of the average rank in the AUC metric on the tabular (a) and image (b) data versus average rank of the computational complexity of the displayed methods measured via training time (left) and prediction time (right). MO-GAAL has been omitted from the tabular figures, as its performance positioned it too far to the right with the training time rank of 19.4 and the prediction time rank of 10.0.

as well – these methods have fast inference but lower performance.

We provide results averaged over the studied contexts on image data. Due to the variability of the results in each context, the x-axis will vary. In the averaged ranks, VAE is on the Pareto front in both fit and prediction times, see Fig. 4.5b. Its prediction complexity is given mainly by choice of the number of samples taken in the computation of the sampled reconstruction score (3.22). The kNN detector has negligible training time, given only by the construction of the tree structure representing data, but seems to be mostly unusable on image data due to slow prediction times on datasets that are large in dimension and the number of samples. The fmGAN finds itself in a completely reversed scenario.

4.4 Conclusion

The presented extensive comparison of anomaly detection methods based on deep generative methods, namely variants of flows, variational autoencoders, and generative adversarial networks with shallow methods based on alternative paradigms revealed that the performance of anomaly detection methods strongly depends on experimental conditions. We have identified the most important contexts (sources of variation) to be the type of data, availability of labeled anomalies for hyperparameter tuning, and the available computational power. There are also factors of variance that have a smaller relevance in the conducted experiments in [213], such as the use of ensembles, alternative performance metrics, and Bayesian optimization of model hyperparameters, which did not have an effect on the relative performance of different models.

This is the list of some of the most important practical observations and recommendations, some of which will be relevant in Chapter 5.

- Methods with more exact likelihood modeling, such as kNN, flows, and autoencoder-based models, perform better in scenarios with a limited number of anomalies available for hyperparameter tuning.
- Majority of the methods fail to detect semantic anomalies. The exception is the fmGAN, which uses a generator-discriminator pair, but only if given enough computational resources and many anomalous samples for cross-validation.
- OC-SVM, when properly tuned, can defeat most of the state-of-the-art on tabular data, although it suffers from overfitting when hyperparameters are selected using too few anomalies in the validation set.
- The method of the first choice appears to be the VAE/WAE due to its relatively cheap, precise, and consistent performance in most of the experiments. However, it possesses so many degrees of freedom that it forms a full family of methods. It was found that the best performance is obtained when estimating the full variance of (tabular data) samples on the output of the decoder and evaluating anomalies using sampled reconstruction score.

Many aspects have not been covered and remain a topic of future work, such as the identification of the relevant kind of anomalies in the semantic datasets or the design of ensembles of methods of various types. Although we have shown that the number of anomalies available for validation is an important context, there was no

4.4 Conclusion

further budget for a comparison of anomaly detection methods with active learning. We have also completely left out the comparison of models on temporal data, such as time series or video, which is a very challenging task. Finally, an interesting area to study further is the influence of the presence of unlabeled anomalies in the training data.

5

Anomaly detection in multi-factor data

5.1 Introduction

In the course of this text, we have been gathering information about state-of-the-art methods, available datasets, and potential unsolved problems in anomaly detection. The ultimate goal of this endeavour was to find an intriguing anomaly detection problem and propose a novel method for its solution, which will be presented in this chapter. Here is a list of the findings that have been gathered so far.

1. In Section 3.4, the problem of identifying anomalies in high-resolution image data was solved and the two-stage model approach proved to be the most successful. The best models were a combination of a probabilistic autoencoder, which produced informative latent encoding, and a classical anomaly detector, which operated on the encoded data of highly reduced dimensionality. The dimensionality reduction alleviated the computational burden from the second stage model which could be more deeply fine-tuned. Eventually, a simple kNN detector was the best choice for a second-stage model.
2. In Chapter 4, a thorough comparison of existing anomaly detectors was done. We have seen what are the most important contexts of an anomaly detection problem (data type, number of labeled anomalies, and budget available for hyperparameter tuning) that one should consider when choosing a method for solving a practical problem. It was shown that deep generative models gain an edge over other methods when solving anomaly detection problems on image data, especially on problems where semantic anomalies occur.
3. In the same chapter, it was shown that although probabilistic autoencoders are generally well-suited for image anomaly detection problems, adversarial training might be beneficial for the detection of **semantic** anomalies [52] with enough budget for hyperparameter tuning. In fact, the majority of the methods compared in Chapter 4 failed in the detection of semantic anomalies.

Since the detection of semantic anomalies in images is a relatively novel field, we have decided to cover this problem in this chapter using the findings described in the list above. Semantic anomalies appear most often in visual data and their anomaly is based on the high-level (semantic) information in the image. For example, an image (used in [213]) can be anomalous because it is blurred, or because it has a different object in the foreground (e.g. plane in the sky instead of a bird in the sky), or different background (e.g. the plane is on a runway, whereas it is usually on the sky).

5.2 Decomposing the anomaly score

From the point of view of the above definition, they are all anomalies, but the user might be interested in anomalies of a certain type, or they might want the anomalies to be automatically classified according to their type. This difference can only be made based on the high-level, semantic information of an image. A good semantic detector should be also robust to non-semantic shifts [222], i.e. data-generating factors that are not present in the training data but are not considered anomalous. The detection of semantic anomalies has been previously studied under the name **subspace** anomaly detection [223, 224, 225]. The idea, as the name suggests, is that the anomaly is not visible in the full input space, where it might be shadowed by noise, but only in the subspace. The subspace is most of the time "axis parallel" or defined in a linear transformation of the input space. Semantic anomalies further generalize this to non-linear transformations.

It seems unlikely in practice that the subspace in which anomalies would be detectable would be aligned with the input space, or with its linear transformation. Contrary, independent components emerge after non-linear projections as shown in [226, 227, 228, 229, 230, 231, 232], which motivates this work. Here, we propose to disentangle the input into independent factors, each providing an anomaly score. Ideally, a semantic anomaly and its source would be then better detectable by one of these scores rather than by a score given to the original input.

In this chapter, the proposed disentanglement into independent factors and the resulting composition of anomaly scores is first theoretically justified. This multi-factor anomaly score is a weighted combination of anomaly scores corresponding to individual factors of the disentangled latent space. In Sec. 5.3, the concrete details (construction, training, and evaluation) of the novel model are described. In the experimental Sec. 5.4, the proposed model is extensively compared to baselines on several image benchmarks. It is demonstrated that the model is capable of detecting the factor that is the most likely source of the anomaly in the unsupervised case, and quickly improves with very few labeled samples.

5.2 Decomposing the anomaly score

In this section, we will derive a general formula for the computation of the anomaly score of a VAE model for the case when the latent space can be disentangled into independent components. This will be useful as a theoretical foundation of the proposed anomaly detector in Sec. 5.3.

5.2.1 Orthogonal generative model

Let us remind ourselves that the VAE (see Sec. 3.2.1) fits a generative model with data $\mathbf{x} \in \mathbb{R}^d$

$$p_{\theta}(\mathbf{x}) = \int_{\mathcal{Z}} p_{\theta}(\mathbf{x}|\mathbf{z}) p(\mathbf{z}) d\mathbf{z} \quad p_{\theta}(\mathbf{x}|\mathbf{z}) = \mathcal{N}(\mathbf{x}; \boldsymbol{\mu}_{\theta}(\mathbf{z}), \boldsymbol{\sigma}^2 \mathbf{I}), \quad (5.1)$$

where $p_{\theta}(\mathbf{x}|\mathbf{z})$ is the decoder and the prior on the latent h -dimensional variable \mathbf{z} is either fixed $p(\mathbf{z}) = \mathcal{N}(0, \mathbf{I})$, or further parametrized $p_{\theta}(\mathbf{z})$, e.g. as in [233]. The VAE also includes an encoder $q_{\phi}(\mathbf{z}|\mathbf{x})$ and is optimized by minimization of the ELBO objective (3.11).

The above generative model (5.1) can be rewritten as $\mathbf{x} = \boldsymbol{\mu}_{\theta}(\mathbf{z}) + \mathbf{e}$ where \mathbf{e} is (usually isotropic) Gaussian noise. This formulation emphasizes the need for marginalization since $\boldsymbol{\mu}_{\theta}(\mathbf{z})$ is a random variable of dimension h (same as that of the latent space \mathcal{Z}) and noise \mathbf{e} is a random variable of dimension d , which is the same as the data. Equation (5.1) therefore marginalizes away random variables corresponding to latent \mathbf{z} . Due to this ambiguity, the assignment between \mathbf{x} and \mathbf{z} is not unique. In fact, for any \mathbf{x} exists \mathbf{z}' [171, 234] such that

$$\mathbf{x} = \mathbf{x}' + \mathbf{e}^{\perp} = \boldsymbol{\mu}_{\theta}(\mathbf{z}') + \mathbf{e}^{\perp}$$

where \mathbf{e}^{\perp} is the observation noise that lies in the normal space perpendicular to the manifold defined by the decoder mean $\boldsymbol{\mu}_{\theta}(\mathbf{z})$. This interpretation implies independence between $\boldsymbol{\mu}_{\theta}(\mathbf{z}')$ and \mathbf{e}^{\perp} , which allows for the approximation

$$p_{\theta}(\mathbf{x}) \approx p(\boldsymbol{\mu}_{\theta}(\mathbf{z}'))p(\mathbf{e}^{\perp}). \quad (5.2)$$

However, the independence relation was found [234] to be sufficiently accurate even for the original noise estimate, $\mathbf{x} = \mathbf{x}' + \mathbf{e}$. The probability of the reconstruction $p_{\theta}(\mathbf{x}')$ is given by the change of coordinate formula from $p_z(\mathbf{z})$ (here we use the subscript z in order to distinguish that the distribution is on the latent space \mathcal{Z}), yielding

$$p_{\theta}(\mathbf{x}) \approx p_{\theta}(\mathbf{x}')p(\mathbf{e}) = p_z(\boldsymbol{\mu}_{\theta}^{-1}(\mathbf{x}')) \left| \frac{\partial \boldsymbol{\mu}_{\theta}^{-1}(\mathbf{x})}{\partial \mathbf{x}} \right| p(\mathbf{e}). \quad (5.3)$$

A gaussian noise model might be assumed, e.g. $p(\mathbf{e}) = \mathcal{N}(\mathbf{x} - \mathbf{x}', \sigma^2 \mathbf{I})$. In practice, an anomaly score for the orthogonal model $s(\mathbf{x}) = -\log p_{\theta}(\mathbf{x})$ is computed as

$$s(\mathbf{x}) = -\log p(\mathbf{e}) - \log p_z(\mathbf{z}) - \log \left| \frac{\partial \boldsymbol{\mu}_{\theta}^{-1}(\mathbf{x})}{\partial \mathbf{x}} \right|, \quad (5.4)$$

which is essentially the reconstruction error with additional terms.

5.2.2 Anomaly in the latent space

Let's observe how the above generative model changes when we assume the distribution on latent \mathbf{z} to be multi-modal conditioned by hidden label y . This simplification assumes that the latent distribution for normal and anomalous data is different. Let

$$p_z(\mathbf{z}|y) = p_n(\mathbf{z})^y p_a(\mathbf{z})^{1-y}, y \in [0, 1], \quad (5.5)$$

where $y = 1$ for normal data, $y = 0$ for anomalies, and $p_n(\mathbf{z}), p_a(\mathbf{z})$ are the latent distributions of normal and anomalous data, respectively. Then from (5.4) we have

$$s(\mathbf{x}|y) = -\log p(\mathbf{e}) - y \log p_n(\mathbf{z}) - (1-y) \log p_a(\mathbf{z}) - \log \left| \frac{\partial \boldsymbol{\mu}_{\theta}^{-1}(\mathbf{x})}{\partial \mathbf{x}} \right|,$$

Since y is usually unknown, we will integrate it away by expectation over y ,

$$\begin{aligned} \mathbb{E}_{p(y)}[s(\mathbf{x}|y)] &= -\log p(\mathbf{e}) - \log \left| \frac{\partial \boldsymbol{\mu}_{\theta}^{-1}(\mathbf{x})}{\partial \mathbf{x}} \right| \\ &\quad - \int_y y \log p_n(\mathbf{z}) p(y) dy - \int_y (1-y) \log p_a(\mathbf{z}) p(y) dy \\ &\propto -\log p(\mathbf{e}) - \log \left| \frac{\partial \boldsymbol{\mu}_{\theta}^{-1}(\mathbf{x})}{\partial \mathbf{x}} \right| - \alpha \log p_n(\mathbf{z}) = s(\mathbf{x}). \end{aligned} \quad (5.6)$$

5.3 Shape-guided decomposition

where we assume $\mathbb{E}_{p(y)}[y] = \alpha$, and $p_a(\mathbf{z}) \propto 1$, because the probability of an anomaly is assumed to be the same everywhere, which then allows us to drop this term since it is independent of \mathbf{x} .

Now consider a **disentangled** model, where the data is generated from multiple independent latent spaces, $\mathbf{z} = \mathbf{z}_1, \dots, \mathbf{z}_l$,

$$\mathbf{x} = f(\mathbf{z}_1, \dots, \mathbf{z}_l) + \boldsymbol{\epsilon}, \quad (5.7)$$

where each of the latents has distribution $p(\mathbf{z}_i) = \mathcal{N}(0, \mathbf{I})$. Using the same derivations, each of the latent spaces \mathbf{z}_i can be a potential source of different types of anomalies, with hidden labels $y = (y_1, \dots, y_l)$. Therefore, instead of (5.5), we have

$$p(\mathbf{z}|y) = \prod_{i=1}^l p_{n_i}(\mathbf{z}_i)^{y_i} p_{a_i}(\mathbf{z}_i)^{1-y_i}, y_i \in [0, 1]. \quad (5.8)$$

Repeating derivation of (5.6) for multiple latent variables, the anomaly score becomes

$$s(\mathbf{x}) = -\log p(\boldsymbol{\epsilon}) - \log \left| \frac{\partial \boldsymbol{\mu}_{\boldsymbol{\theta}}^{-1}(\mathbf{x})}{\partial \mathbf{x}} \right| - \sum_{i=1}^l \alpha_i \log p_{n_i}(\mathbf{z}_i), \quad (5.9)$$

where α_i denotes the probability that the latent variable of the i th factor is generated from the normal class. In this work, we assume that α_i is not known during training but has to be estimated in the validation stage from examples of anomalous samples.¹

The interpretation of the values of α_i will be important later, in Sec. 5.3, where we construct the latent spaces to give them a specific meaning, and in Sec. 5.3.2, where we describe their fitting. Fitting the values of all α_i on a set of labeled data is equal to estimating the mean of $p(y_i)$ for the given data. This can be interpreted as estimating how likely it is for an anomaly to appear in the i -th latent in the context of the current dataset.

In contrast, for a single data sample, we are more interested in the actual values of y_i , which are binary and which determine whether the sample is anomalous in the context of the latent space i . Their estimation is equal to the estimation of the distributions $p(y_i|\mathbf{x})$ and will be discussed in Sec. 5.3.3.

5.3 Shape-guided decomposition

We demonstrate the advantage of disentanglement in detecting semantic anomalies on image data, because (i) the disentanglement has been researched mostly in this domain [227, 231, 235], (ii) the anomaly detection community is the most active in this field, and (iii) the findings of Chapter 4 showed that most deep generative models are not very efficient when dealing with semantic anomalies.

For the construction of the proposed model, we assume an image \mathbf{x} to be composed of three main components: a mask (shape of the object), a background texture, and a foreground texture (the object). This of course is not true for all images, but many open datasets contain images that are structured this way. The mask together with the

¹Based on the industrial experience of authors, this assumption is safe, i.e. there are usually examples of anomalies, though their diversity might be low.



Figure 5.1: Examples of decomposition on the Wildlife MNIST dataset by the SGVAE-GAN model. The first row contains the input samples, below that are the decoded masks, backgrounds, foregrounds, and finally the whole reconstructions. The model can learn appropriate masks in an unsupervised fashion.

foreground texture defines the semantic meaning of the object, as it is what defines the class of the image in datasets. According to the above assumptions, each component (mask, background texture, and foreground texture) is generated from an independent variable. Therefore, for the latent distribution $p(\mathbf{z})$ it holds that

$$p(\mathbf{z}) = p_{z_m}(\mathbf{z}_m)p_{z_f}(\mathbf{z}_f)p_{z_b}(\mathbf{z}_b), \quad (5.10)$$

where subscripts m, f, b denote the mask, foreground, and background latent variable, respectively. A representative example of a dataset where each image is composed of three independent components is the Wildlife MNIST dataset [236]. It is constructed using masks from MNIST [237] combined with foreground and background textures from [238] (see more details on its construction in Appendix B). For examples from individual classes see the top row of Fig. 5.1.

The independent decomposition (5.10) is akin to (5.7), but here we ascribe high-level semantic meaning to the individual latent spaces. This means that the model built on top of the assumption (5.10) has an inductive bias, which enables the unsupervised disentangled representation of the individual components of an image. The independency is further reinforced by the fact that the parts of the model responsible for the representation of the components do not share weights. Furthermore, since we want to *a priori* ascribe specific meaning to the disentangled latent spaces, we cannot use automatic disentanglement of individual dimensions as is the case in literature [226, 231, 232], since there, the disentanglement is not unique and the semantic meaning of the disentangled factors has to be found manually in a post-processing phase.

In this section, the structure of the proposed generative model with independent latent spaces and its training procedure is described first. Then, in order to be able to detect and describe semantic anomalies, we combine the model with the anomaly

5.3 Shape-guided decomposition

score derived in Sec. 5.2.

5.3.1 Shape-guided VAEGAN model

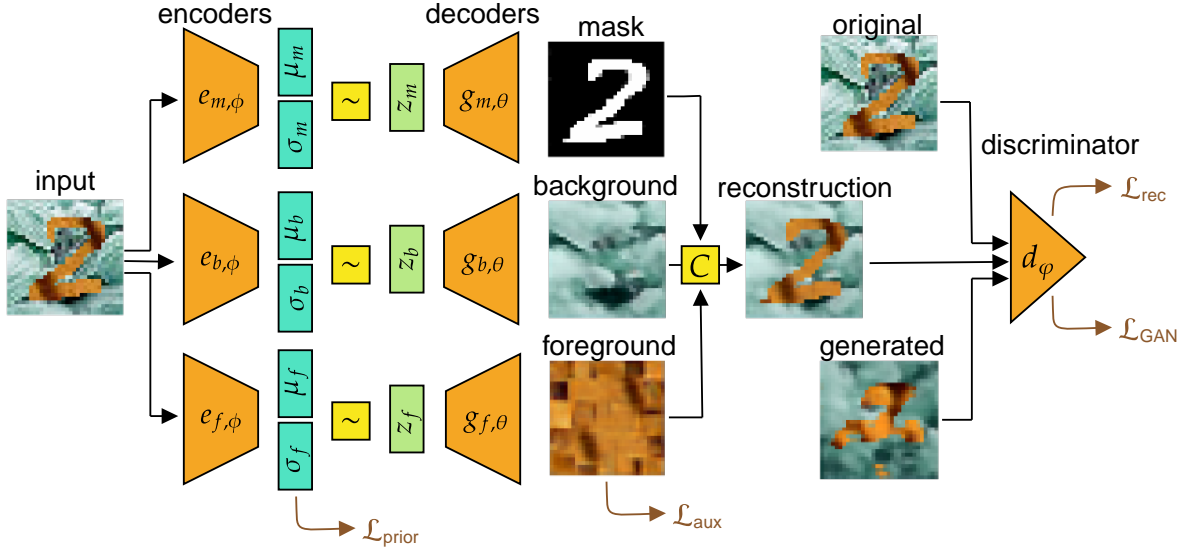


Figure 5.2: The schema of the proposed model. Convolutional blocks are denoted in orange, fully connected in cyan, and intermediate representations in green. The yellow squares represent special operations - c is the composition (5.13) and the reparametrization trick is denoted by \sim . The generated sample is obtained by feeding samples from priors $\mathcal{N}(0, \mathbf{I})$ to the decoders.

The model disentangling the input image into its three components is our synthesis of a VAEGAN [239] and Counterfactual generative networks (CGN) [236].² Building blocks of this model, further denoted as SGVAEGAN, are outlined in Fig. 5.2. The model uses three separate independent autoencoders for three components of an image, a block combining them to the reconstructed image, and a discriminator for improved performance on semantic image data. We emphasize that it is this strict separation of autoencoders that improves the desired disentanglement.

Autoencoders responsible for individual components are vanilla VAE consisting of an encoder

$$q_{i,\phi}(\mathbf{z}_i|\mathbf{x}) = \mathcal{N}\left(\mathbf{z}_i; \boldsymbol{\mu}_{i,\phi}(\mathbf{x}), \text{diag}(\boldsymbol{\sigma}_{i,\phi}(\mathbf{x}))\right), \quad i \in \{m, f, b\}, \quad (5.11)$$

and a decoder

$$\mathbf{x}_i = g_{i,\theta}(\mathbf{z}_i), \quad i \in \{m, f, b\}. \quad (5.12)$$

Although Sec. 5.2 we assumed $\mathbf{x} \in \mathcal{X} = \mathbb{R}^d$, here the data are colored images, therefore $\mathcal{X} = \mathbb{R}^{H \times W \times 3}$, where (W, H) stands for the width and height of an image in pixels. This is without any loss of generalization on the already derived results, as it only affects the term $\log p(\mathbf{e})$ in (5.9), but this will be expressed by an element-wise operation which is introduced in the following text. Latent variables \mathbf{z}_i are sampled through the usual reparametrization trick (3.13) from the normal distribution (5.11) with a diagonal covariance matrix.

²Counterfactual generative networks [236] were selected because based on our preliminary experiments, the result offered superior disentanglement likely due to highly inductive bias.

All three autoencoders output a tensor of the size of the input image, \mathbf{x}_m , \mathbf{x}_f , and $\mathbf{x}_b \in \mathbb{R}^{H \times W \times 3}$, which are then composed by a compositor $c(\mathbf{x}_m, \mathbf{x}_f, \mathbf{x}_b)$ to form a reconstructed image \mathbf{x}'

$$\mathbf{x}' = c(\mathbf{x}_m, \mathbf{x}_f, \mathbf{x}_b) = \mathbf{x}_m \odot \mathbf{x}_f + (1 - \mathbf{x}_m) \odot \mathbf{x}_b, \quad (5.13)$$

where \odot denotes a Hadamard (element-wise) product and 1 is a matrix of ones with the same dimension as \mathbf{x}_m . The elements of the mask \mathbf{x}_m lie in the interval $[0, 1]$ and the training procedure ensures that they are pushed to the extremes of the closed interval, such that elements with nonzero values represent the pixels that contain the most prominent object in the image.

The **loss function** optimized during training is an augmented version of the VAE ELBO loss (3.11), which accounts for the need to optimize the discriminator, and also for ensuring that the separate autoencoders that are responsible for encoding and decoding different components of an image retain their meaning. Without the additional constraints imposed during training, it could happen that the autoencoder responsible for modelling of the background learns the foreground instead, or learns to reconstruct the complete image, while the remaining autoencoders learn nothing. Therefore, the total training loss consists of a reconstruction error term, a GAN-like loss, regularization of the latent space, and an auxiliary part,

$$\mathcal{L} = \lambda_{\text{rec}} \mathcal{L}_{\text{rec}} + \mathcal{L}_{\text{GAN}} + \mathcal{L}_{\text{prior}} + \mathcal{L}_{\text{aux}}. \quad (5.14)$$

Their contributions are controlled by a scalar weight λ_{rec} and by weights contained in \mathcal{L}_{aux} . The first three parts in Eq. (5.14) are adopted from VAEGAN while the last part is adopted from the CGN model. The rest of this section describes them in detail.

Reconstruction loss uses the feature-matching construction (3.5), which was chosen because of its good performance on semantic anomalies in Chapter 4. It generalizes the standard reconstruction loss by comparing \mathbf{x} and \mathbf{x}' at a certain depth of the discriminator d_{ϕ} as

$$\mathcal{L}_{\text{rec}} = \|d_{n,\phi}(\mathbf{x}) - d_{n,\phi}(\mathbf{x}')\|_2^2, \quad (5.15)$$

where $d_{n,\phi}(\mathbf{x})$ is the intermediate representation of \mathbf{x} at the n -th layer of the discriminator and ϕ are its weights. When $n = 0$, the loss coincides with log-likelihood (3.13) for VAE with Gaussian output distribution. In the experiments in Sec. 5.4, n is treated as a hyperparameter subjected to tuning.³ The authors of the VAEGAN model claim that incorporating the discriminator for image reconstruction leads to an improvement in the overall reconstruction/generation quality as it pushes the model to be able to abstract beyond the capabilities of pixel-wise reconstruction loss such as (3.13). Note that (5.15) is used to optimize the weights of the decoders and encoders and not the discriminator. This is possible because the reconstruction \mathbf{x}' undergoes the process (5.11)-(5.13) which makes it functionally dependent on θ and ϕ .

GAN loss \mathcal{L}_{GAN} was adopted from the VAEGAN model. It is used to optimize the discriminator d_{ϕ} and the decoders $g_{m,\theta}$, $g_{f,\theta}$, and $g_{b,\theta}$, of the model via

$$\mathcal{L}_{\text{GAN}} = -\log d_{\phi}(\mathbf{x}) - \log(1 - d_{\phi}(\mathbf{x}')) - \log(1 - d_{\phi}(\tilde{\mathbf{x}})), \quad (5.16)$$

³Based on our experimental results, we cannot recommend a single good value, as values selected on the validation set ranged from 0 to 7.

5.3 Shape-guided decomposition

where $\tilde{\mathbf{x}}$ is a generated sample obtained by sampling $\tilde{\mathbf{z}}_m$, $\tilde{\mathbf{z}}_f$, and $\tilde{\mathbf{z}}_b$ from $\mathcal{N}(0, \mathbf{I})$, decoding these via (5.12) and composing them via (5.13). The training procedure of a VAE-GAN model is slightly different from a standard GAN. Compare the expression (5.16) with the usual GAN training objective (3.1), where only the generated sample $\tilde{\mathbf{x}}$ is used. This makes perfect sense since there is no reconstruction \mathbf{x}' in a GAN. Furthermore, the output of the discriminator d_ϕ also has a slightly changed meaning. It outputs a scalar in the range $[0, 1]$, where a higher value means a sample comes from the training dataset and a lower value means the sample is generated or reconstructed. In order for the discriminator to learn to score the samples in this fashion, the loss (5.16) is minimized with respect to the discriminator parameters and maximized with respect to the decoders' parameters. This corresponds to discriminator/generator training in a GAN model, see Sec. 3.1.

Prior loss is used to regularize the latent spaces as in (3.10) by minimizing the KL divergence between $q_\phi(\mathbf{z}|\mathbf{x})$ and the prior $p(\mathbf{z})$ as

$$\mathcal{L}_{\text{prior}} = D_{\text{KL}}(q_\phi(\mathbf{z}|\mathbf{x})||p(\mathbf{z})) = \sum_{i \in \{m, f, b\}} D_{\text{KL}}(q_{i,\phi}(\mathbf{z}_i|\mathbf{x})||p(\mathbf{z}_i)), \quad (5.17)$$

because \mathbf{z}_i are assumed to be independent. Furthermore, since it is assumed $p(\mathbf{z}_i) = \mathcal{N}(0, \mathbf{I})$, $\mathcal{L}_{\text{prior}}$ can be computed analytically, see (3.12).

Auxiliary loss was adopted from [236] and it is a weighted combination of three parts

$$\mathcal{L}_{\text{aux}} = \lambda_{\text{bin}} \mathcal{L}_{\text{bin}}(\mathbf{x}_m) + \lambda_{\text{mask}} \mathcal{L}_{\text{mask}}(\mathbf{x}_m) + \lambda_{\text{text}} \mathcal{L}_{\text{text}}(\mathbf{x}_m, \mathbf{x}_f, \mathbf{x}). \quad (5.18)$$

The texture loss $\mathcal{L}_{\text{text}}(\mathbf{x}_m, \mathbf{x}_f, \mathbf{x})$ ensures that the parts of the network assigned to reconstruct the background and foreground are not switched and that no shape information is stored in the foreground. It is computed in the following way: 36 patches are sampled from the image \mathbf{x} in regions where the mask \mathbf{x}_m is nonzero. These are then composed together to form a tensor \mathbf{x}_g that is as large as the image. Then, a perceptual loss [240] between \mathbf{x}_g and \mathbf{x}_f is computed. A perceptual loss is a measure of the similarity of two images that uses a convolutional neural network that was pre-trained on a very large database of image data. It is used because by using a pre-trained network, one can compare higher-level, semantic information of two images, which cannot be captured by a pixel-wise similarity measure such as L2 loss. In our case, the perceptual loss is computed as the L1 distance between the activation maps of \mathbf{x}_f and \mathbf{x}_g in the first four convolutional layers of a VGG16 [241] convolutional network. By minimizing it, the output of the foreground autoencoder is forced to be similar to the general (because of the sampling) texture of the object captured by the mask.

The term \mathcal{L}_{bin} forces elements of the mask to be close to either 0 or 1. The objective to be minimized is

$$\mathcal{L}_{\text{bin}}(\mathbf{x}_m) = -\frac{1}{N} \sum_{i=1}^N \mathbf{x}_{m,i} \log_2(\mathbf{x}_{m,i}) + (1 - \mathbf{x}_{m,i}) \log_2(1 - \mathbf{x}_{m,i}), \quad (5.19)$$

where the index i goes over all elements of the tensor \mathbf{x}_m and N is the number of its elements.

Finally, $\mathcal{L}_{\text{mask}}$ prevents degeneration of the mask to be all zeroes or all ones, which would lead to failure in the identification of background/foreground. This is achieved

by computing

$$\mathcal{L}_{\text{mask}}(\mathbf{x}_m) = \left[\max\left(0, \tau - \frac{1}{N} \sum_{i=1}^N \mathbf{x}_{m,i}\right) + \max\left(0, \frac{1}{N} \sum_{i=1}^N \mathbf{x}_{m,i} - \tau\right) \right] \quad (5.20)$$

where $\tau \in [0, 1]$ is a parameter that forces the mask to occupy a total area of the image that is in the interval $[\tau, 1 - \tau]$.

The complete training procedure of the SGVAEGAN model is described in detail in Alg. 6.

Algorithm 6 Training of the SGVAEGAN model. The budget is either a time limit or a fixed maximum number of iterations. Capital letters denote a batched variable.

Require: An SGVAEGAN model with encoders and decoders $(q_{i,\phi}(\mathbf{z}_i|\mathbf{x}), g_{i,\theta}(\mathbf{z}_i))$, $i \in \{m, f, b\}$ and a discriminator $d_\phi(\mathbf{x})$, a composition operator $c(\mathbf{x}_m, \mathbf{x}_f, \mathbf{x}_b)$, a training set $X = \{\mathbf{x}_1, \mathbf{x}_2, \dots, \mathbf{x}_n\} \subset \mathcal{X}$, maximum number of iterations $I \in \mathbb{N}$, batchsize $B \in \mathbb{N}$.

- 1: $i \leftarrow$ Iteration counter
- 2: $(\phi, \theta, \varphi) \leftarrow$ initialize parameters
- 3: **while** $i < I$ or (ϕ, θ, φ) are not converged **do**
- 4: $X_B \leftarrow$ batch of B samples from the dataset X
- 5: $\mathcal{L}_{\text{rec}}, \mathcal{L}_{\text{aux}}, \mathcal{L}_{\text{prior}}, \mathcal{L}_{\text{GAN}} \leftarrow 0$
- 6: **for** $\mathbf{x} \in X_B$ **do**
- 7: // Computation of prior, reconstruction, and auxiliary losses
- 8: $(\mathbf{z}_m, \mathbf{z}_f, \mathbf{z}_b) \leftarrow$ encodings of \mathbf{x}
- 9: $\mathcal{L}_{\text{prior}} \xleftarrow{+} \sum_{i \in \{m, f, b\}} D_{\text{KL}}(q_{i,\phi}(\mathbf{z}_i||\mathbf{x})|p(\mathbf{z}_i))$
- 10: $(\mathbf{x}_m, \mathbf{x}_f, \mathbf{x}_b) \leftarrow (g_{m,\theta}(\mathbf{z}_m), g_{f,\theta}(\mathbf{z}_f), g_{b,\theta}(\mathbf{z}_b))$
- 11: $\mathbf{x}' \leftarrow c(\mathbf{x}_m, \mathbf{x}_f, \mathbf{x}_b)$
- 12: $\mathcal{L}_{\text{rec}} \xleftarrow{+} \|d_{n,\varphi}(\mathbf{x}) - d_{n,\varphi}(\mathbf{x}')\|_2^2$
- 13: $\mathcal{L}_{\text{aux}} \xleftarrow{+} \lambda_{\text{bin}} \mathcal{L}_{\text{bin}}(\mathbf{x}_m) + \lambda_{\text{mask}} \mathcal{L}_{\text{mask}}(\mathbf{x}_m) + \lambda_{\text{text}} \mathcal{L}_{\text{text}}(\mathbf{x}_m, \mathbf{x}_f, \mathbf{x})$.
- 14: // Adversarial loss
- 15: $(\tilde{\mathbf{z}}_m, \tilde{\mathbf{z}}_f, \tilde{\mathbf{z}}_b) \leftarrow$ samples from the prior $p(\mathbf{z})$
- 16: $(\tilde{\mathbf{x}}_m, \tilde{\mathbf{x}}_f, \tilde{\mathbf{x}}_b) \leftarrow (g_{m,\theta}(\tilde{\mathbf{z}}_m), g_{f,\theta}(\tilde{\mathbf{z}}_f), g_{b,\theta}(\tilde{\mathbf{z}}_b))$
- 17: $\tilde{\mathbf{x}} \leftarrow c(\tilde{\mathbf{x}}_m, \tilde{\mathbf{x}}_f, \tilde{\mathbf{x}}_b)$ a generated sample
- 18: $\mathcal{L}_{\text{GAN}} \xleftarrow{+} -\log d_\phi(\mathbf{x}) - \log(1 - d_\phi(\mathbf{x}')) - \log(1 - d_\phi(\tilde{\mathbf{x}}))$
- 19: **end for**
- 20: // Update of the parameters
- 21: $\phi \xleftarrow{+} -\nabla_\phi \frac{1}{B} (\lambda_{\text{rec}} \mathcal{L}_{\text{rec}} + \mathcal{L}_{\text{aux}} + \mathcal{L}_{\text{prior}})$
- 22: $\theta \xleftarrow{+} -\nabla_\theta \frac{1}{B} (\lambda_{\text{rec}} \mathcal{L}_{\text{rec}} + \mathcal{L}_{\text{aux}} - \mathcal{L}_{\text{GAN}})$
- 23: $\varphi \xleftarrow{+} -\nabla_\varphi \frac{1}{B} \mathcal{L}_{\text{GAN}}$
- 24: **end while**
- 25: **return** encoders and decoders $(q_{i,\phi}(\mathbf{z}_i|\mathbf{x}), g_{i,\theta}(\mathbf{z}_i))$, $i \in \{m, f, b\}$, discriminator $d_\phi(\mathbf{x})$

5.3.2 Detecting anomalies with SGVAEGAN

If the SGVAEGAN is trained well, particularly if the decomposition into latent spaces is (at least approximately) right, different types of anomalies should be in low-density

5.3 Shape-guided decomposition

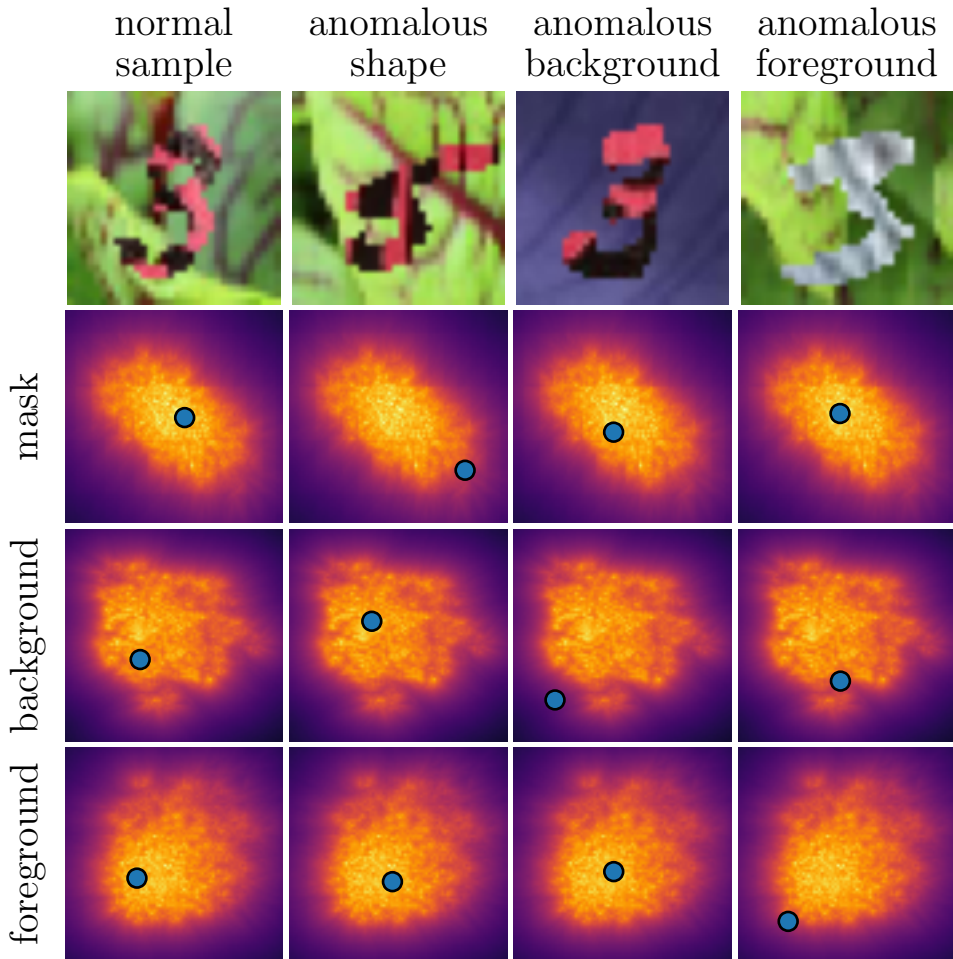


Figure 5.3: Position of different images encoded to individual latent spaces using SG-VAEGAN model with two-dimensional latent spaces. The training set consisted of images with factors fixed to those of the digit in the first column. The densities of encodings of normal (training) data, estimated by a kNN detector (5.26) are depicted as well.

regions of different latent spaces. This is illustrated in Fig. 5.3 on the Wildlife MNIST dataset, where we can see that anomalous shape, background texture, and foreground texture is anomalous in the corresponding latent space. We can use the score (5.9) and assign $p_{n_i}(\mathbf{z}_i) = p_{z_i}(\mathbf{z}_i), i \in \{m, f, b\}$, since the model is trained on normal data. Then we have

$$s(\mathbf{x}) = -\log p(\mathbf{e}) - \log \left| \frac{\partial g^{-1}(\mathbf{x})}{\partial \mathbf{x}} \right| - \sum_{i \in \{m, f, b\}} \alpha_i \log p_{z_i}(\mathbf{z}_i), \quad (5.21)$$

where $g(\mathbf{z})$ is a function that computes an image from the latent encodings via (5.13)

$$g(\mathbf{z}) = g(\mathbf{z}_m, \mathbf{z}_f, \mathbf{z}_b) = g_{m,\theta}(\mathbf{z}_m) \odot g_{f,\theta}(\mathbf{z}_f) + (1 - g_{m,\theta}(\mathbf{z}_m)) \odot g_{b,\theta}(\mathbf{z}_b). \quad (5.22)$$

Following the derivations in [234], we use the fact that $\frac{\partial g^{-1}(\mathbf{x})}{\partial \mathbf{x}} = \left(\frac{\partial g(\mathbf{z})}{\partial \mathbf{z}} \right)^{-1}$, and assume the independency of the latent spaces of $\mathbf{z}_m, \mathbf{z}_f, \mathbf{z}_b$. Then Eq. (5.21) can be rewritten to

$$s(\mathbf{x}) = -\log p(e) + s_j(\mathbf{x}) - \sum_{i \in \{m, f, b\}} \alpha_i \log p_{z_i}(\mathbf{z}_i), \quad (5.23)$$

where $s_j(\mathbf{x}) = \log \left| \frac{\partial g(\mathbf{z})}{\partial \mathbf{z}} \right|$ denotes the Jacobian term, which is functionally dependent on the input image \mathbf{x} through the latent encodings $\mathbf{z} = (\mathbf{z}_m, \mathbf{z}_f, \mathbf{z}_b)$, see (5.11). A reader recognizes that $\frac{\partial g(\mathbf{z})}{\partial \mathbf{z}}$ is not square, hence its determinant is zero. Ref. [234] suggests estimating the determinant from a diagonal matrix after SVD decomposition, which is valid if one assumes the orthogonality of the data and noise.

The proposed score, based on (5.23), reads as a weighted sum of the individual components

$$s(\mathbf{x}) = \alpha_r s_r(\mathbf{x}) + \alpha_j s_j(\mathbf{x}) + \alpha_m s_m(\mathbf{x}) + \alpha_f s_f(\mathbf{x}) + \alpha_b s_b(\mathbf{x}), \quad (5.24)$$

where $s_i, i \in \{r, j, m, f, b\}$ are individual anomaly score components which will be described in the following text. The α_r, α_j weights were added in order to tune the total score to the modalities of anomalous data, which were not seen during the training, and therefore the base model is not fitted to them. The values of α can be either set manually or estimated from a small number of labeled anomalies as described in the following text.

Reconstruction error Reconstructed samples are needed for the computation of the reconstruction term $-\log p(\mathbf{e})$. However, since the reconstruction steps (5.11)-(5.13) contain sampling through the reparametrization trick, the reconstructions \mathbf{x}' are stochastic. As we have shown already in (3.22), the estimate of the reconstruction error is stabilized by taking an average from multiple reconstructions $\{\mathbf{x}'_l\}_{l=1}^L$ computed as

$$s_r(\mathbf{x}) = -\frac{1}{\sigma^2 L} \sum_{l=1}^L \|\mathbf{x} - \mathbf{x}'_l\|_2^2, \quad (5.25)$$

where the scalar variance $\sigma^2 \in \mathbb{R}$ is estimated from the data during the training of the model. The number of samples was set to $L = 10$ during our experiments.

Latent scores A correct estimate of the likelihood of latent representations $p_{z_i}(\mathbf{z}_i)$, $i \in \{m, f, b\}$ is important for the score (5.24). Even though latent representations are regularized during the fitting of the model to have normal distribution $\mathcal{N}(0, \mathbf{I})$, it was shown [183] that the fit is usually not very good. This can be also seen in Fig. 5.3, where the distribution of the latent representations is not perfectly normal. Therefore, we approximate $p_{z_i}(\mathbf{z}_i)$ by the k-nearest-neighbor (kNN) density estimator, see Sec. 2.2.2, which is trained on latent representations of normal data. This method was chosen for its simplicity yet powerful performance, which was demonstrated both by the results in Sec. 3.4 and also in Chapter 4, where it scored amongst the top models on low dimensional data. This requirement will be satisfied here, as the encoders comprise the high-dimensional image data into latent space with dimensionality on the order of 10^2 . The score of a sample in the i -th latent space, $i \in \{m, f, b\}$, has the form

$$s_i(\mathbf{x}) = \frac{1}{k} \sum_{\mathbf{z}_j \in \mathcal{Z}_{k,i}} \|\mathbf{z}_i - \mathbf{z}_j\|_2, \mathbf{z}_i = \boldsymbol{\mu}_{i,\phi}(\mathbf{x}), \quad (5.26)$$

5.3 Shape-guided decomposition

which is the average Euclidean distance between the projection \mathbf{z}_i of the tested sample \mathbf{x} into the latent space, and the set $\mathcal{Z}_{k,i}$ of the k -nearest projections of the normal data to the same latent space. The value of k is a hyperparameter tuned on the validation set.

Optimization of α The proposed score is effectively a weighted sum of individual parts. In theory, one can set the weights α by themselves if one knows in which latent to expect the anomaly. Since this knowledge is rarely available, we estimate them from data (that contains examples of labeled anomalies) by regularized logistic regression as

$$\alpha^* = \arg \min_{\alpha} - \sum_n y_n \log \sigma(s(\mathbf{x}_n|\alpha)) + (1 - y_n) \log(1 - \sigma(s(\mathbf{x}_n|\alpha))) + \beta \|\alpha - \alpha_0\|_2^2, \quad (5.27)$$

$$s(\mathbf{x}_n|\alpha) = \sum_i \alpha_i \hat{s}_i(\mathbf{x}_n), i \in \{r, j, m, f, b\}, \quad (5.28)$$

where $\sigma(\cdot)$ is the sigmoid function, $y_n \in \{0, 1\}$ are labels, α_0 is a prior value and the index n goes over the samples in the labeled dataset. Since the scores $s_i(\mathbf{x})$ can have very different scales (e.g. $s_r(\mathbf{x}) \sim 10^4$ while $s_f(\mathbf{x}) \sim 10^0$), we rescale them to have zero mean and unit variance. The rescaled scores are denoted as $\hat{s}_i(\mathbf{x})$. The regularization is set using $\beta = \frac{\beta_0}{n_1}$, $\beta_0 \in \mathbb{R}$, where n_1 is the number of positive (anomalous) samples in the dataset, and β_0 is a hyperparameter. This ensures that the prior α_0 has a large influence over the final value of α when there is a small number of known anomalies, thus ensuring the robustness of the final α estimate. The prior is set such that $\alpha_{0,i} = 1$ for such i where the AUC computed from $\{s_i(\mathbf{x}_n), y_n\}_n$ is maximal and zero everywhere else, making α_0 a failsafe value. The criterion (5.27) is optimized by an LBFGS optimizer [242].

Removing the Jacobian from the score While the score (5.23) is theoretically correct under the assumption that anomalies are located in areas of low density, the publication [234] shows that it does not work well when the model is trained on data without anomalies. Our experiments shown below arrived at the same conclusion. We suspect the cause to be that the decoders g can be arbitrary (with arbitrary jacobian) in parts of the space not supported by the data, where anomalous samples are located. Moreover, the computation of the determinant is so expensive that the score is effectively useless for state-of-the-art image models. Therefore, we propose dropping the Jacobian term $s_j(\mathbf{x})$ from (5.24) and adding the discriminator score

$$s_d(\mathbf{x}) = 1 - d_{\varphi}(\mathbf{x}), \quad (5.29)$$

which works well for anomaly detection according to [239] and also for semantic anomaly detection in images, which was shown by an exceptional performance of the fmGAN model with the score (5.29) in Chapter 4. The alternative score then reads

$$s(\mathbf{x}) = \alpha_r s_r(\mathbf{x}) + \alpha_d s_d(\mathbf{x}) + \alpha_m s_m(\mathbf{x}) + \alpha_f s_f(\mathbf{x}) + \alpha_b s_b(\mathbf{x}). \quad (5.30)$$

Again, the values of α are optimized similarly to (5.27).

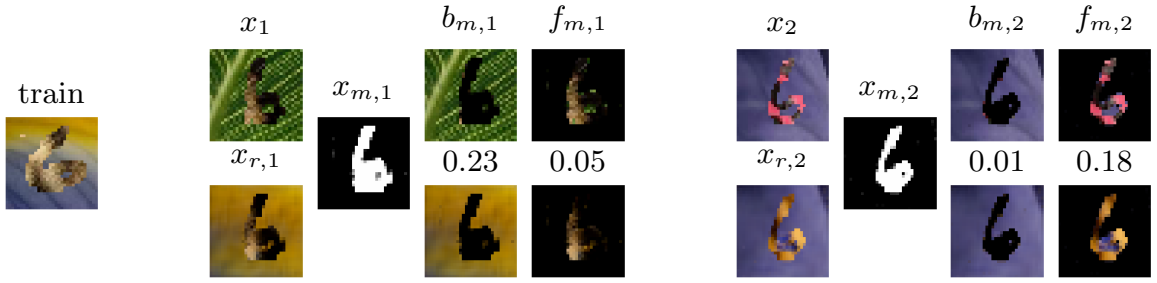


Figure 5.4: Masked detection technique for identifying the source of anomaly. The model was originally trained on samples similar to the one on the very left, brown-striped sixes on a purple-yellow background. To distinguish between anomalies in the background and foreground texture, a reconstruction \mathbf{x}_r and a mask \mathbf{x}_m are computed for a test sample \mathbf{x}_1 , which is anomalous in the background, and \mathbf{x}_2 , which is anomalous in the foreground texture. The scores S_b (5.31), S_f (5.32) are computed as scaled differences between the original and reconstructed masked-out backgrounds, $b_m = \mathbf{x} \odot (1 - \mathbf{x}_m)$ and foregrounds $f_m = \mathbf{x} \odot \mathbf{x}_m$ and their values are displayed between the image of the original and reconstructed foregrounds and backgrounds.

5.3.3 Anomaly factor identification

The model presented above can identify the source of the anomaly through the information from the individual latent spaces. Under the formalism (5.5), estimation of the probability of being generated from the normal model is simply $p(y|\mathbf{z}) \propto p(\mathbf{z}|y)$, which is only possible for proper distributions. Since we used an improper distribution ($p_a(\mathbf{x}) \propto 1$) to minimize the number of unknown parameters, we cannot use direct estimation and have to rely on approximation. This approximation relies on the fact that the source of anomaly should have a low probability in the respective latent space. We have designed two approximate methods for identifying it. The main benefit of these methods is that they are completely unsupervised and computationally cheap. Note that when using them, it is assumed that anomalies are generated from a single source, i.e. being anomalous only either in shape, foreground, or background.

Ranked anomaly factor identification The first approximation relies on the replacement of the likelihood $p(y_i|\mathbf{z}_i(\mathbf{x}))$ by an empirical quantile. Specifically, we store the values of anomaly scores $s_{i,train} = s_i(\mathbf{x}_{train})$ for the training set and for a new sample \mathbf{x} compute the quantile $q_i(\mathbf{x})$ (relative rank) within the training scores of the corresponding latent space. The anomaly source estimate is then computed as the maximum of the relative rank $y^* = \arg \max_{i \in \{m,f,b\}} q_i(\mathbf{x})$.

Masked anomaly factor identification Using even a properly trained model, the ranked method is not always able to correctly identify all three types of anomaly sources. Therefore, we have simplified the problem to distinguish the source of an anomaly only in the background or foreground texture by computing the reconstruction errors for those components separately. For an input \mathbf{x} , the reconstructed image \mathbf{x}' and a mask \mathbf{x}_m are computed. Using these, we compute the normalized reconstruction

5.4 Experiments

errors as

$$S_b = \frac{\sum_j ((\mathbf{x}_j - \mathbf{x}'_j)(1 - \mathbf{x}_{m,j}))^2}{\sum_j 1 - \mathbf{x}_{m,j}} \quad (5.31)$$

$$S_f = \frac{\sum_j ((\mathbf{x}_j - \mathbf{x}'_j)\mathbf{x}_{m,j})^2}{\sum_j \mathbf{x}_{m,j}} \quad (5.32)$$

where index j goes over elements in all dimensions of an array $\mathbf{x} \in \mathbb{R}^{H \times W \times 3}$ representing an RGB image. See Fig. 5.4 for an illustration of the principle of this method. The normalization factor in (5.31,5.32) is important since the object in the foreground usually covers fewer pixels than the background. If S_b is higher, the prediction for the anomaly factor is "background" and vice versa. The comparison of the ranked and masked method is presented in Sec. 5.4.4

5.4 Experiments

In the experimental evaluation of the proposed model, we follow the strict protocol that was established in Chapter 4. The datasets were split into training, validation, and test subsets for each of their classes (or subproblems in the case of the MVTec-AD dataset). Details on the splits for individual experiments can be found in the respective sections below. Then, for each such split and each model, 50 hyperparameter settings were randomly sampled from a set of possible values. The use of Bayesian optimization to select hyperparameters was considered but eventually dropped as it did not have an impact on the relative rank of the methods in Chapter 4. The validation set was used to select the best hyperparameter values for a given model on a specific subproblem. Unless mentioned otherwise, the experiments below report (ROC)AUC values of the selected models computed on the test set. The models were trained for 50 epochs each.

The datasets used in the experimental evaluation were selected in order to contain semantic anomalies (with the exception of the MVTec-AD dataset). Two artificial datasets (Wildlife MNIST and COCOPlaces) were created as baselines on which the model is supposed to perform well. Especially Wildlife MNIST contains easily segmentable objects. For details on datasets, see Appendix B.

5.4.1 Baseline methods

We have selected unsupervised anomaly detectors mainly based on the review in Chapter 4, specifically those that were amongst the top performers on colored images. For additional These models include:

Variational Autoencoder (VAE) - a convolutional VAE from Sec. 3.2 that uses the sampled reconstruction error (5.25). The decoder variance σ^2 is estimated from the data.

Feature-matching GAN (fmGAN) - a convolutional GAN model trained using the feature-matching loss (3.4). The anomaly score is based on the discriminator (5.29).

VAEGAN - a convolutional VAE where reconstruction is enforced through a discriminator [239]. The anomaly score is (5.29).

Deep Support Vector Data Description (DSVDD) - is a model that learns a transformation of data via a neural network to a subspace where the anomalies lie outside of a hypersphere composed of transformed normal data. The anomaly score is then the distance of a point from the center of the hypersphere, see Sec. 2.2.3.

fast Anomaly GAN (fAnoGAN) - a GAN model trained via Wasserstein loss and gradient penalization that identifies anomalies by backward-searching the latent code z that is the most likely to generate the given test samples, see Sec. 3.1.2.

Counterfactual Generative Network (CGN) - this is a baseline model [236] for the decomposition of data into three components. Although not originally intended as an anomaly detector, it can be used as one as it provides the discriminator score (5.29) and proved itself to be competitive in our experiments.

Shape Guided VAE (SGVAE) - this is a modification of the proposed model introduced to study the impact of the discriminator. It is trained without a discriminator and the reconstruction loss is $-\mathbb{E}_{q_\phi(\mathbf{z}|\mathbf{x})}[\log p_\theta(\mathbf{x}|\mathbf{z})]$, similar to a classical VAE. The anomaly score for this model is the sampled reconstruction error (5.25).

Shape Guided VAEGAN (SGVAEGAN) - this is the basic proposed model that is trained in a completely unsupervised fashion and evaluated without considering the full anomaly scores (5.24) and (5.30). Instead, the default anomaly score is (5.29).

SGVAE $_\alpha$ - this is the SGVAE model where the score (5.24) is considered. To compute the anomaly scores, SGVAE models pre-trained in an unsupervised fashion were used and only the weights α were computed on a validation dataset.

SGVAEGAN $_\alpha$ - this is the full proposed model. As discussed in the Sec. 5.4.2, it is used with the score (5.24) with the Jacobian, but later the Jacobian is dropped and the model is used with score (5.30).

5.4.2 The contribution of the Jacobian

We start by demonstrating that dropping the Jacobian term from the score (5.24) does not have a negative effect on the detection performance of the proposed model. Tab. 5.1 shows AUCs of the model that uses the score (5.24) with and without the Jacobian term $s_j(\mathbf{x})$ on a subset of the SVHN2 dataset. For each normal class, training, and testing sets containing 750 normal and 150 anomalous samples were used. To obtain the presented statistic, the subsets were sampled 5 times. The difference in performance is almost negligible but the difference in computational costs is high. Therefore, we omit the term from all further experiments, and the score (5.30) is used for the SGVAEGAN $_\alpha$ instead, while for SGVAE $_\alpha$, the term is dropped from (5.24).

5.4.3 Detection of semantic anomalies

We now study how the proposed detector behaves as it gradually incorporates more knowledge in the form of labeled anomalies used to optimize weights α via (5.27). To simulate a semantic anomaly scenario, the following training and testing protocol is used with the Wildlife MNIST and COCOPlaces datasets. The training set consists of

5.4 Experiments

class	AUC - no $s_j(x)$	AUC - with $s_j(x)$	α_r	α_j
0	0.70 ± 0.04	0.70 ± 0.05	1.00	0.00
1	0.82 ± 0.01	0.82 ± 0.02	1.09	-0.03
2	0.71 ± 0.02	0.72 ± 0.02	0.93	-0.01
3	0.64 ± 0.02	0.64 ± 0.02	0.94	0.01
4	0.72 ± 0.03	0.72 ± 0.03	1.00	0.00
5	0.67 ± 0.01	0.66 ± 0.01	0.98	0.00
6	0.68 ± 0.02	0.68 ± 0.02	0.60	0.00
7	0.73 ± 0.05	0.73 ± 0.05	1.00	0.00
8	0.69 ± 0.04	0.71 ± 0.02	0.98	-0.04
9	0.63 ± 0.05	0.63 ± 0.04	0.80	0.00

Table 5.1: Experiment with $s_j(x)$ on a subset of the SVHN2 dataset. The mean values of α weights estimated with (5.27) are also presented and show that the weight of the Jacobian term is suppressed during their computation.

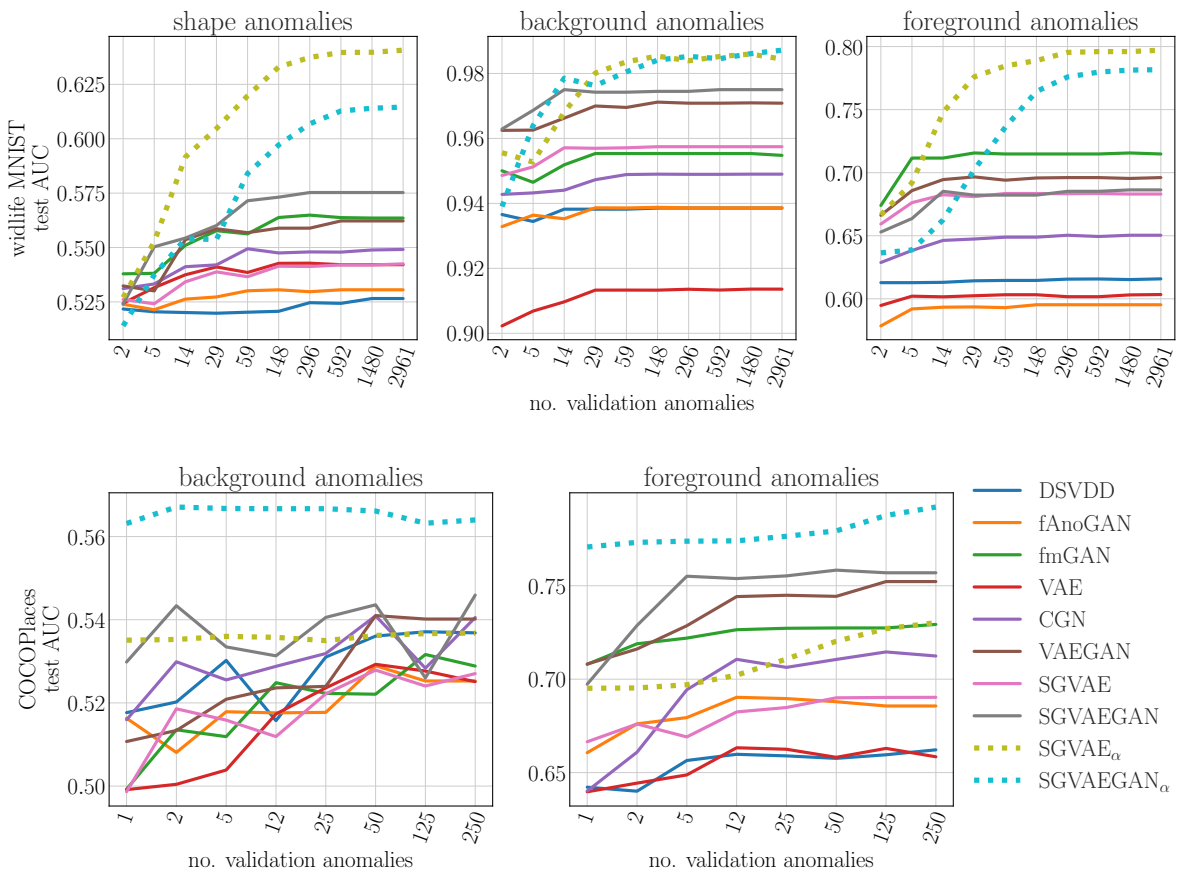


Figure 5.5: Semantic anomaly detection experiment on the Wildlife MNIST (top) and COCOPlaces (bottom) datasets. The x-axis covers a changing number of anomalies present in the validation dataset. The y-axis reports the average AUC over dataset subclasses and 5-fold cross-validation.

samples of one class (the whole experiment is repeated for all 10 classes) from the non-mixed version of the datasets (see Appendix B for details of how this is generated). Then, for a given factor of variation, validation, and test sets are drawn from the mixed version of the dataset, where the anomaly of a sample is based on whether the target factor is the same or different as in the training dataset. This introduces a non-semantic shift, as the validation and test sets contain a variation of a factor that was not seen in the training data but is not considered anomalous.

An example of how the individual data sets are constructed is the following: consider that the training set contains only images of MNIST class "0" with "leaf" background and brown foreground texture, like in Fig. 5.1. When the target factor of variation is *background*, then in the validation and test set, all images with "leaf" background are considered normal and any other background is considered anomalous, no matter what the remaining factors of variation (digit and foreground texture) are, therefore a brown digit "0" with a blue background texture is considered anomalous, while a yellow "9" with "leaf" background is considered normal.

Fig. 5.5 shows AUCs of compared methods with respect to the number of known anomalies in the validation set, in which the ratio of anomalous to normal data ranges from 0.1% to 100% with the number of normal samples staying the same. The models are trained on the same training non-mixed data, their hyperparameters are selected on the validation dataset and the resulting test set AUC is averaged over 10 classes and a 5-fold random selection of the validation anomalies. While on Wildlife MNIST, both SGVAE $_{\alpha}$ and SGVAEGAN $_{\alpha}$ quickly dominate other methods once a few (five) examples of anomalies are available, the SGVAE $_{\alpha}$ performs worse on COCOPlaces. This is the effect of the discriminator of SGVAEGAN, which is used in the score and which contributes to the improved fit of the model. The results also show how methods benefit from a better selection of hyperparameters when more known anomalies are in the validation set.

5.4.4 Anomaly factor identification

In this section, we compare the two approximate methods for identification of the source of an anomaly as described in Sec. 5.3.3, i.e. the ranked and the masked method. For the comparison, we use the mixed version of the Wildlife MNIST dataset. The results in the form of prediction accuracies over different normal classes are shown in Tab. 5.2.

The ranked method sometimes fails to identify all three factors better than random chance, which has an accuracy of 0.33. The masked method performs better than the ranked one in the identification of the background and foreground anomalies, although the background anomaly detection accuracies are not completely satisfactory on all digit classes. However, we explain this by some classes having very similar backgrounds, e.g. a very common misclassification for class "4" is that with anomalous background from classes "1" or "7", see Fig. 5.1. In these misclassifications, the background is reconstructed rather well, while even a small imprecision in the mask leads to a high reconstruction error in the foreground. Still, this method of detection of the source of anomaly might be useful in some real-world problems, given we can train the model to produce correct masks.

5.4 Experiments

normal class	ranked			masked	
	shape	background	foreground	background	foreground
0	0.82	0.19	0.62	0.88	0.95
1	0.84	0.92	0.19	0.85	1.0
2	0.92	0.37	0.7	0.95	0.6
3	0.55	0.86	0.24	0.63	0.96
4	0.79	0.46	0.85	0.62	1.0
5	0.57	0.89	0.31	0.72	1.0
6	0.74	0.95	0.52	0.96	0.96
7	0.47	0.84	0.75	0.87	0.98
8	0.64	0.64	0.62	0.98	0.97
9	0.88	0.27	0.1	0.77	0.94

Table 5.2: Accuracy of factor detection on the wildlife MNIST dataset for *ranked* and *masked* methods. The columns correspond to test samples anomalous in the respective factor.

5.4.5 Large scale study

problem	DSVDD	fAnoGAN	fmGAN	VAE	CGN	VAEGAN	SGVAE	SGVAEGAN	SGVAEGAN $_{\alpha}$	
bottle	0.81	0.97	0.95	0.98	0.90	0.85	0.98	0.83	0.97	0.92
capsule	0.65	0.69	0.67	0.74	0.69	0.58	0.76	0.66	0.80	0.67
nut	0.78	0.72	0.88	0.71	0.82	0.84	0.69	0.78	0.81	0.86
pill	0.64	0.71	0.73	0.73	0.59	0.70	0.77	0.72	0.78	0.73
transistor	0.69	0.77	0.90	0.81	0.88	0.75	0.78	0.79	0.81	0.79
mean rank	8.90	6.20	3.50	4.20	5.50	7.60	4.50	7.00	2.80	4.80

Table 5.3: Aggregated performance in test AUC of models on MVTec-AD problems.

This experiment compares the proposed model in a traditional anomaly detection scenario on selected image datasets. We assume the leave-one-in scenario, when the training dataset contains samples from one class and the rest is considered to be anomalous in validation and test datasets. We believe this is a good representation of a semantic anomaly detection problem as well as being a more realistic option since in real-world problems, anomalies may come from many varying distributions.⁴ To test the models in a non-semantic anomaly detection setting, we have included the

⁴In this regard, we disagree with the authors of [52] which propose the alternative of leave-one-out, stating that in most anomaly detection problems, we want to detect only small perturbations from the target class. However, traditional image benchmarks don't allow for this anyway as the classes are very distinct even in the latter case.

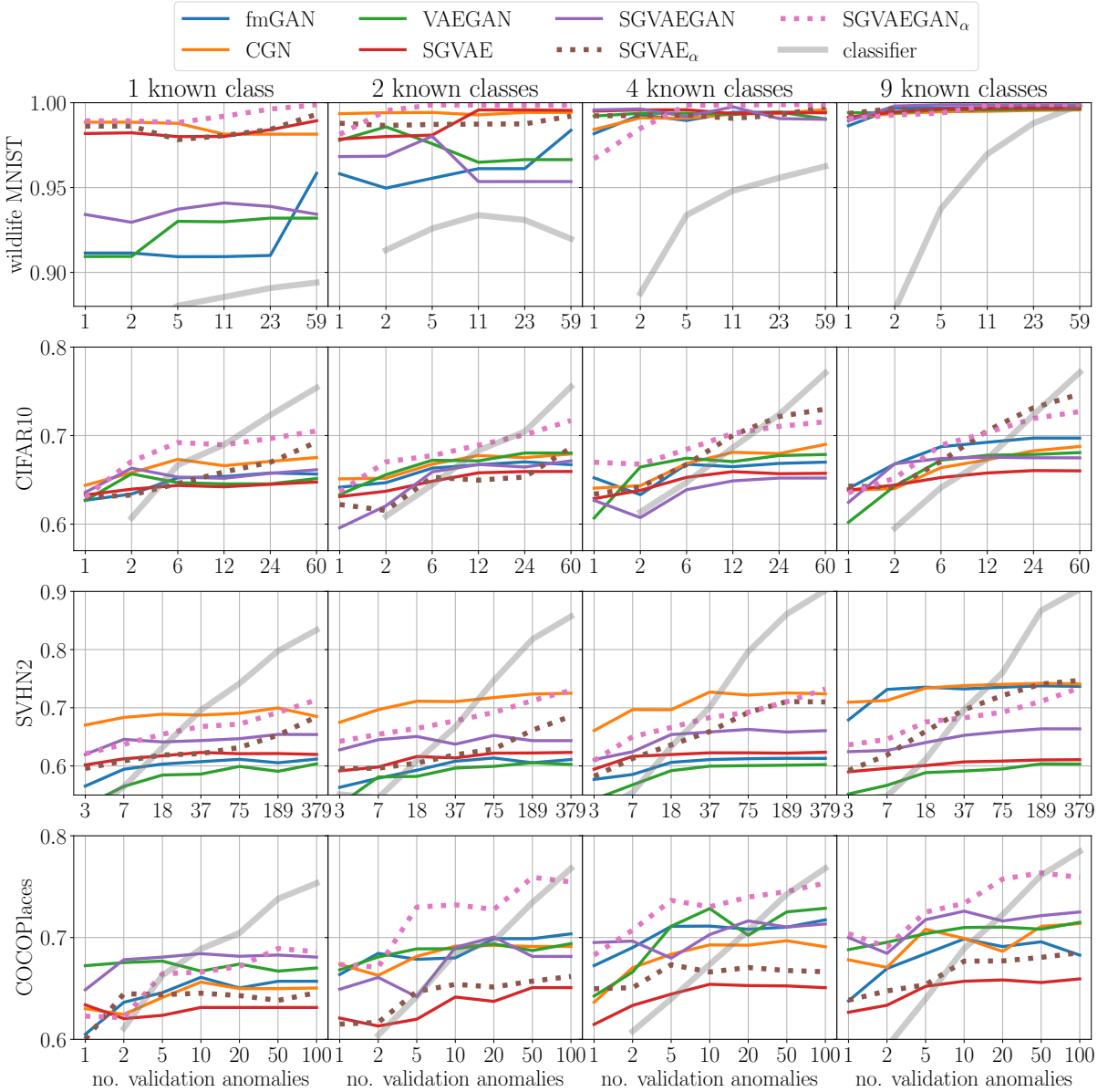


Figure 5.6: Comparison of models on selected image datasets for the leave-one-in experiment. The x-axis covers a changing number of anomalies in the validation dataset, which is used for hyperparameter selection and α computation. The y-axis reports the average test AUC over 10 normal classes. The columns capture experiments with varying availability of validation samples from different anomalous classes, while anomalies of all classes are present in the test set. The number of normal samples in the validation set is the following: Wildlife MNIST: 1184, CIFAR10: 1200, SVHN2: 3792, COCOPhotos: 100.

MVTec-AD dataset where the normal and anomalous data differ only in small details, and which is popular for benchmarking anomaly detection methods.

In practice, it might happen that anomalies are in a few clusters, but only samples from some of them are labeled and available for model selection. To simulate such a scenario and similar validation/test discrepancies, we performed model selection with significantly varied validation sets. First, the total number of anomalies in the validation set was varied, which constitutes the x-axis in Fig. 5.6. Second, for each normal

5.4 Experiments

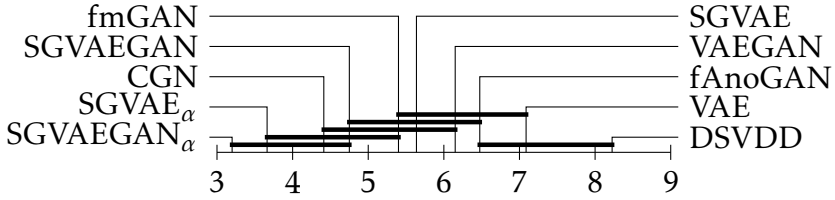


Figure 5.7: A critical difference diagram that shows mean ranks of models from Tab. 5.4. The difference in the performance of 2 models compared on 40 datasets to be statistically significant on level 10% must be greater than the value of the Nemenyi test $CD_{0.1}=1.95$. The thick horizontal lines connect the models with performance differences less than this.

class, samples from only a limited number of anomalous classes were sampled to the validation set, which creates the different columns in Fig. 5.6. The test set contained anomalies from all the classes left out of training. An example with 4 anomalous classes known in validation: training of models was done using class "1" of the SVHN2 dataset. The validation dataset contained normal data from class "1" and anomalies sampled from classes "2", "3", "4" and "5". The testing dataset contained normal samples from class "1" and anomalies sampled from all the other classes. The normal data split is 60/20/20%, 50% of available anomalies are in the test set.

Fig. 5.6 contains the overall comparison across the different variants of validation datasets used for model selection. It contains only a selection of the best-performing models to improve readability. Apart from the SVHN2 dataset, the proposed model outperforms the baselines after observing just 10 examples of anomalies, in some cases even less. A comparison of all baselines aggregated over all semantic datasets is presented in the critical difference diagram in Fig. 5.7, where mean ranks of models are compared using the methodology presented in [243]. Tab. 5.4 contains a disaggregated comparison in the case of 2% of labeled anomalies from 4 classes in the validation dataset. Finally, see Tab. 5.3 for the results on the MVTec-AD subproblems. Here the alternative $SGVAE_\alpha$ trained without a discriminator performs better. This is probably because the dataset only contains non-semantic anomalies, which cannot be well captured by the discriminator score which is used in $SGVAEGAN_\alpha$. Since the total number of anomalies in MVTec-AD is low, the use of the discriminator score may lead to overfitting of the α estimate on the validation dataset. By selecting the optimal model on the validation set and reporting on the test set, which is not standard in every publication [213], we believe that our experiments provide a realistic comparison of baselines.

A fully supervised classifier trained on the validation dataset is included in the comparison in Fig. 5.6. By its inclusion, we try to answer a question that is very pertinent for practitioners – if you need at least some labeled anomalies to tune your unsupervised models anyway, what amount of labeled anomalies means that you can train a fully supervised classifier instead? Our comparison shows that this amount is surprisingly low, apart from the (relatively easy) Wildlife MNIST dataset. This result is, of course, closely tied to the specific setting of our experiment and should not be extrapolated to other problems without further research.

5.5 Conclusion

In this chapter, the SGVAEGAN was proposed - a deep generative model for anomaly detection that uses several independent latent spaces to generate a data sample. The generative model is assumed to generate the normal class, and the flexibility of the latent spaces allows us (i) to detect anomalies of a certain type, and (ii) to question which component of the test sample is anomalous. This concept has been applied to semantic anomaly detection of images where the anomaly may be present in the shape, foreground, and background textures. The proposed anomaly detector was tested on synthetic as well as real-world image datasets.

The detector was fine-tuned to the type of anomalies that are of interest. This has been achieved by learning the weights of the scores from the independent latent spaces for known anomalies. Naturally, the performance of the proposed method improves with a growing number of available anomalies in the validation. However, as shown in the experimental section, as few as ten labeled anomalies were already enough to improve over the tested baselines, and this was shown to be true even if samples from only certain anomalous classes were labeled. A comparison with a supervised classifier was done, which demonstrated that a relatively low number of labeled anomalies is enough for the supervised classifier to outperform any anomaly detector. This sets an upper bound on the meaningful range of problems suitable for anomaly detection methods. We recommend performing such an experiment for every anomaly detection method.

A possible improvement of the proposed model might come from the use of a more flexible latent model, such as Vamp, that was introduced in Sec. 3.2.2 and successfully used on the Alfvén mode detection problem in Sec. 3.4. This was not initially considered, since the large scale study in the previous chapter did not show it brought any performance benefits on other data (see the discussion on the VAE family of models in Sec. 4.3.2). It might be possible though that real-world problems with complicated latent distributions might be a more suitable environment, where a multi-modal prior is suitable.

The proposed SGVAEGAN model is a demonstration of the general approach, which can be used with any type of decomposition/disentanglement of the latent space. The requirement for the application of another generative model is that it has to be capable of learning the disentanglement in an unsupervised manner. We wish these results motivate the research in the learning of disentangled models.

5.5 Conclusion

	class	DSVDD	fANoGAN	fmGAN	VAE	CGN	VAEGAN	SGVAE	SGVAEGAN	SGVAEGAN _{α}
wildlife MNIST	0	0.82	0.98	1.00	0.94	1.00	1.00	1.00	1.00	1.00
	1	0.88	1.00	1.00	1.00	1.00	1.00	1.00	1.00	1.00
	2	0.63	0.97	1.00	0.85	0.99	1.00	0.96	0.93	0.99
	3	0.83	0.99	0.99	0.99	0.99	0.99	1.00	1.00	1.00
	4	0.91	1.00	0.99	0.99	1.00	1.00	1.00	0.99	1.00
	5	0.39	0.93	0.99	0.85	0.99	0.99	1.00	1.00	1.00
	6	0.69	1.00	1.00	1.00	1.00	1.00	1.00	1.00	1.00
	7	0.92	0.99	0.99	1.00	0.99	0.99	1.00	1.00	1.00
	8	1.00	1.00	1.00	1.00	1.00	1.00	1.00	1.00	1.00
	9	0.71	0.94	0.99	0.94	0.99	1.00	0.99	1.00	0.99
CIFAR10	airplane	0.72	0.72	0.68	0.68	0.68	0.78	0.78	0.76	0.81
	automobile	0.63	0.56	0.69	0.62	0.78	0.75	0.46	0.76	0.74
	bird	0.67	0.67	0.60	0.66	0.60	0.56	0.70	0.47	0.68
	cat	0.61	0.58	0.59	0.57	0.62	0.60	0.59	0.56	0.69
	deer	0.71	0.75	0.65	0.74	0.66	0.63	0.74	0.66	0.78
	dog	0.60	0.59	0.65	0.58	0.64	0.64	0.59	0.63	0.67
	frog	0.71	0.76	0.71	0.75	0.67	0.69	0.73	0.60	0.78
	horse	0.61	0.56	0.60	0.54	0.75	0.72	0.67	0.65	0.70
	ship	0.74	0.80	0.77	0.71	0.74	0.71	0.82	0.72	0.84
	truck	0.67	0.65	0.79	0.63	0.76	0.67	0.54	0.70	0.73
SVHN2	0	0.64	0.64	0.68	0.64	0.78	0.64	0.67	0.65	0.71
	1	0.63	0.60	0.61	0.67	0.76	0.61	0.69	0.70	0.82
	2	0.61	0.58	0.58	0.62	0.76	0.62	0.62	0.63	0.75
	3	0.55	0.55	0.59	0.58	0.71	0.54	0.59	0.64	0.64
	4	0.58	0.58	0.63	0.63	0.80	0.66	0.62	0.69	0.74
	5	0.56	0.57	0.61	0.58	0.72	0.57	0.60	0.65	0.67
	6	0.57	0.60	0.58	0.59	0.75	0.62	0.61	0.66	0.73
	7	0.59	0.58	0.66	0.64	0.82	0.61	0.65	0.69	0.77
	8	0.58	0.60	0.57	0.58	0.70	0.57	0.59	0.65	0.65
	9	0.56	0.59	0.62	0.59	0.74	0.56	0.60	0.65	0.68
COCOPlaces	airplane	0.72	0.74	0.77	0.74	0.68	0.79	0.64	0.81	0.77
	bird	0.48	0.48	0.64	0.53	0.64	0.61	0.47	0.69	0.66
	boat	0.65	0.70	0.81	0.76	0.76	0.77	0.77	0.71	0.77
	bus	0.58	0.82	0.85	0.67	0.83	0.87	0.74	0.70	0.78
	dog	0.72	0.71	0.71	0.72	0.63	0.64	0.71	0.66	0.71
	horse	0.58	0.57	0.69	0.65	0.59	0.71	0.65	0.69	0.64
	motorcycle	0.63	0.65	0.75	0.60	0.77	0.77	0.69	0.73	0.78
	train	0.64	0.71	0.68	0.65	0.55	0.62	0.69	0.74	0.75
	truck	0.48	0.65	0.61	0.63	0.63	0.69	0.63	0.70	0.68
	zebra	0.68	0.63	0.59	0.66	0.84	0.82	0.52	0.79	0.86
mean rank		8.23	6.48	5.40	7.09	4.41	6.15	5.64	4.75	3.66
										3.20

Table 5.4: Test AUC of models trained on the normal class marked in the first column of the table. The shading highlights the top 3 models. In this experiment, the validation dataset contained anomalies from 4 known classes, which is the same as the third column in Fig. 5.6. The ratio of normal data and anomalies in the validation dataset was 100:2. In absolute numbers, this means the following numbers of validation anomalies: wildlife MNIST: 23, CIFAR10: 24, SVHN2: 75, COCOPlaces: 2.

6

Conclusion

In this chapter, we summarize the individual chapters of the dissertation and their relationship to original contributions that were published as peer-reviewed papers or are publicly available in the form of preprints. Also, we try to evaluate the goals that were set in the introduction in Sec. 1.3. Finally, we offer an outlook on future work.

6.1 Contributions

Chapter 1 This chapter sets the playing field for the rest of the text with definitions of basic terms and ideas that are important for anomaly detection. It also introduces basic types of anomalies and sets a list of objectives that we are going to evaluate.

Chapter 2 This chapter contains an introduction to measures available for comparison of anomaly detectors, which is an excerpt from the paper [53], where the goal was to determine whether the standard AUC is the most suitable measure for anomaly detector comparison, as it has some weaknesses. Besides the theoretical description present here, the paper also contains an extensive experimental comparison. Besides that, Chapter 2 also contains an extensive description of the current state-of-the-art shallow anomaly detectors, which partly covers the first objective from Sec. 1.3.

Chapter 3 The rest of the first objective is covered in this chapter with an extensive description of deep anomaly detectors. Special attention is given to detectors based on deep generative models. We believe it is useful both for novices and experienced researchers in the field of generative models and/or anomaly detection as we strived to distill our knowledge of this topic in a digestible yet comprehensive manner.

In Sec. 3.4, the practical use of generative autoencoders is presented in the context of anomaly detection problems in plasma fusion physics. It was published as a journal paper [17]. It provides inspiration for the following chapters because it shows the feasibility of a two-stage approach, where a deep model is coupled with a shallow one operating on the latter model’s low-dimensional representations of otherwise high-dimensional inputs.

Chapter 4 Here, the main results of the paper [213], which is a large-scale theoretical and experimental survey of deep generative models in anomaly detection, are presented. Its goals were to find a research direction in which generative anomaly detectors gain an advantage over other approaches, and it was successful in doing so, as

6.2 Future work

it inspired the model proposed in Chapter 5. Also, this paper itself is a continuation of the original publication [212], which had the same goals, but a much lesser scope.

This chapter fully covers the second objective that was set in Sec. 1.3 by providing insights into: i) the effect of building blocks of anomaly detection on their performance, and ii) the generally poor performance of the existing methods on semantic image anomalies, which is the focus of the following chapter.

Chapter 5 This is the product of the previous chapters and the main contribution of the thesis, which also covers the last objective set in Sec. 1.3. In this chapter, we present a novel multi-factor anomaly detection scheme. The scheme is demonstrated on a novel SGVAEGAN model which performs successfully on the problem of semantic anomaly detection on image data. It also provides a novel manner of informed but unsupervised image disentanglement and most importantly a procedure for anomaly origin detection and explanation, which is something that is missing in the current state-of-art of image anomaly detection. At the time of the writing of this thesis, it is currently considered for publication.

Finally, one of the contributions of this work is that it contains links to all the related software developed during our research process. The list of publicly available repositories is in Appendix C.

6.2 Future work

As the field of anomaly detection progresses, novel methods appear constantly. In the vein of Chapter 4, we should strive to add novel methods into a fair comparison that evaluates them from different perspectives. Although this is clearly not feasible to do continuously, an updated version of such a survey, created after a few years, would be helpful in assessing how the field of anomaly detection has evolved in the meantime. In fact, when publishing the original article [213], we knew that there were novel methods that appeared during the publication process and which we would have liked to cover as well. Furthermore, the conclusion of Chapter 4 covers some missing topics, such as anomaly detection with active learning or temporal anomaly detection, which is a research area that has been gaining a lot of momentum recently.

Possible technical improvements of the model proposed in Chapter 5, such as the use of a more flexible latent prior, are mentioned at the end of that chapter. Although the SGVAEGAN model was specifically designed for anomaly detection on images where a prominent object is positioned on a distinct background, the general approach to anomaly detection via disentanglement based on Eq. (5.9) is possibly applicable to a different kind of data where there is a possibility of anomalies coming from different independent sources. Finally, we believe that in order to improve the understanding of the proposed model behaviour, its capabilities would be best demonstrated in new experiments on some real-world application data.

Apendices

A

Mathematical formulations

A.1 Multivariate normal distribution

A random vector $\mathbf{x} \in \mathbb{R}^d$ follows the multivariate normal (Gaussian) distribution with mean $\boldsymbol{\mu} \in \mathbb{R}^d$, symmetric and positive-definite covariance matrix $\Sigma \in \mathbb{R}^{d \times d}$, if its probability density is

$$p(\mathbf{x}|\boldsymbol{\mu}, \Sigma) = \mathcal{N}(\mathbf{x}|\boldsymbol{\mu}, \Sigma) = (2\pi)^{-\frac{d}{2}} |\Sigma|^{-\frac{1}{2}} \exp\left(-\frac{1}{2} (\mathbf{x} - \boldsymbol{\mu})^T \Sigma^{-1} (\mathbf{x} - \boldsymbol{\mu})\right), \quad (\text{A.1})$$

where $|\Sigma|$ is the determinant of the covariance matrix. Sometimes, instead of covariance the precision matrix is used $\Lambda = \Sigma^{-1}$ which makes some manipulations easier. Some moments of interest are

$$\mathbb{E}[\mathbf{x}] = \boldsymbol{\mu}, \quad (\text{A.2})$$

$$\mathbb{E}[\mathbf{x}\mathbf{x}^T] = \Sigma + \boldsymbol{\mu}\boldsymbol{\mu}^T, \quad (\text{A.3})$$

$$\mathbb{E}[\mathbf{x}^T \mathbf{x}] = \boldsymbol{\mu}^T \boldsymbol{\mu} + \text{Tr}(\Sigma), \quad (\text{A.4})$$

where $\text{Tr}(\cdot)$ is the trace operator.

A.2 The Kullback-Leibler divergence

The Kullback-Leibler (KL) divergence is a measure of distance between two probability distributions. For two continuous probability distributions with probability densities $p(\mathbf{x})$ and $q(\mathbf{x})$ defined on the same probability space we define it as

$$D_{\text{KL}}(p(\mathbf{x})||q(\mathbf{x})) = \int_{\mathcal{X}} p(\mathbf{x}) \ln \frac{p(\mathbf{x})}{q(\mathbf{x})} d\mathbf{x}. \quad (\text{A.5})$$

It is an asymmetric measure, therefore it is not a proper metric. These relations hold

$$p(\mathbf{x}) = q(\mathbf{x}) \text{ almost everywhere} \iff D_{\text{KL}}(p(\mathbf{x})||q(\mathbf{x})) = 0, \quad (\text{A.6})$$

$$D_{\text{KL}}(p(\mathbf{x})||q(\mathbf{x})) \geq 0, \quad (\text{A.7})$$

$$\text{generally } D_{\text{KL}}(p(\mathbf{x})||q(\mathbf{x})) \neq D_{\text{KL}}(q(\mathbf{x})||p(\mathbf{x})). \quad (\text{A.8})$$

A.3 Kullback–Leibler divergence of two normal distributions

For the case of two multivariate normal distributions $p_0(\mathbf{x}) = \mathcal{N}(\mathbf{x}|\boldsymbol{\mu}_0, \Sigma_0)$ and $p_1(\mathbf{x}) = \mathcal{N}(\mathbf{x}|\boldsymbol{\mu}_1, \Sigma_1)$ where $\mathbf{x} \in \mathbb{R}^d$ the KL divergence is

$$\begin{aligned}
D_{\text{KL}}(p_0(\mathbf{x})||p_1(\mathbf{x})) &= \mathbb{E}_{p_0}[\ln p_0(\mathbf{x}) - \ln p_1(\mathbf{x})] \\
&= \frac{1}{2}\mathbb{E}_{p_0}\left[-\ln|\Sigma_0| - (\mathbf{x} - \boldsymbol{\mu}_0)^T \Sigma_0^{-1}(\mathbf{x} - \boldsymbol{\mu}_0) + \ln|\Sigma_1|\right] + \\
&\quad \frac{1}{2}\mathbb{E}_{p_0}\left[(\mathbf{x} - \boldsymbol{\mu}_1)^T \Sigma_1^{-1}(\mathbf{x} - \boldsymbol{\mu}_1)\right] \\
&= \frac{1}{2}\ln\frac{|\Sigma_1|}{|\Sigma_0|} + \frac{1}{2}\mathbb{E}_{p_0}\left[-\text{Tr}(\Sigma_0^{-1}(\mathbf{x} - \boldsymbol{\mu}_0)(\mathbf{x} - \boldsymbol{\mu}_0)^T)\right] + \\
&\quad \frac{1}{2}\mathbb{E}_{p_0}\left[\text{Tr}(\Sigma_1^{-1}(\mathbf{x} - \boldsymbol{\mu}_1)(\mathbf{x} - \boldsymbol{\mu}_1)^T)\right] \\
&= \frac{1}{2}\ln\frac{|\Sigma_1|}{|\Sigma_0|} - \frac{1}{2}\text{Tr}(\Sigma_0^{-1}\mathbb{E}_{p_0}[(\mathbf{x} - \boldsymbol{\mu}_0)(\mathbf{x} - \boldsymbol{\mu}_0)^T]) + \\
&\quad \frac{1}{2}\text{Tr}(\mathbb{E}_{p_0}[\Sigma_1^{-1}(\mathbf{x}\mathbf{x}^T - 2\mathbf{x}\boldsymbol{\mu}_1^T + \boldsymbol{\mu}_1\boldsymbol{\mu}_1^T)]) \\
&= \frac{1}{2}\ln\frac{|\Sigma_1|}{|\Sigma_0|} - \frac{1}{2}\text{Tr}(\Sigma_0^{-1}\Sigma_0) + \frac{1}{2}\text{Tr}(\Sigma_1^{-1}(\Sigma_0 + \boldsymbol{\mu}_0\boldsymbol{\mu}_0^T - 2\boldsymbol{\mu}_0\boldsymbol{\mu}_1^T - \boldsymbol{\mu}_1\boldsymbol{\mu}_1^T)) \\
&= \frac{1}{2}\ln\frac{|\Sigma_1|}{|\Sigma_0|} - \frac{1}{2}d + \frac{1}{2}\text{Tr}(\Sigma_1^{-1}\Sigma_0) + \frac{1}{2}\text{Tr}(\Sigma_1^{-1}(\boldsymbol{\mu}_0 - \boldsymbol{\mu}_1)^T(\boldsymbol{\mu}_0 - \boldsymbol{\mu}_1)) \\
&= \frac{1}{2}\left(\ln\frac{|\Sigma_1|}{|\Sigma_0|} - d + \text{Tr}(\Sigma_1^{-1}\Sigma_0) + (\boldsymbol{\mu}_0 - \boldsymbol{\mu}_1)^T\Sigma_1^{-1}(\boldsymbol{\mu}_0 - \boldsymbol{\mu}_1)\right). \tag{A.9}
\end{aligned}$$

where we have used the common trick using the trace of a scalar, the relation $\text{Tr}(ABC) = \text{Tr}(BCA) = \text{Tr}(CAB)$ and the linearity of the trace operator. For us, a special case is of high interest – one where we have a normal distribution with diagonal covariance and a standard normal distribution, that is $p_0(\mathbf{x}) = \mathcal{N}(\mathbf{x}|\boldsymbol{\mu}, \text{diag}(\boldsymbol{\sigma}^2), \boldsymbol{\sigma}^2 \in \mathbb{R}^d)$ and $p_1(\mathbf{x}) = \mathcal{N}(\mathbf{x}|0, \mathbf{I})$. In that case

$$D_{\text{KL}}(p_0(\mathbf{x})||\mathcal{N}(\mathbf{x}|0, 1)) = \frac{1}{2}\left(\ln\frac{1}{\prod_{i=1}^d \boldsymbol{\sigma}_i^2} - d + \sum_{i=1}^d \boldsymbol{\sigma}_i^2 + \boldsymbol{\mu}^T \boldsymbol{\mu}\right) = \frac{1}{2}\sum_{i=1}^d \boldsymbol{\sigma}_i^2 - 1 - \ln\boldsymbol{\sigma}_i^2 + \boldsymbol{\mu}_i^2. \tag{A.10}$$

B

Datasets

B.1 Tabular datasets

In total, we have collected 40 tabular datasets, the majority of which come from the UCI repository [244]. The complete listing of dataset dimensions is recorded in Tab. B.1 and B.2. Except for the ANNThyroid, Arrhythmia, HAR, HTRU2, KDD Cup 99 (small), Spambase, Mammography, and Seismic, where the anomaly class has a clear meaning (security incident or disease), we have followed the technique of [245] for creating artificial datasets for anomaly detection tasks from classification datasets. More precisely, we have used only "easy" and "medium" anomalies, as "hard" and "very hard" are not truly anomalous in the sense of being statistically distinct from the normal class.

B.2 Image datasets

The number of image datasets used for the evaluation of deep models is limited, as there are very few publicly available image datasets designed purely for anomaly detection. In our experiments, we have used the MNIST-C and MVTec-AD datasets. Furthermore, we have extended these with artificially created anomaly datasets based on common image datasets that are usually used for classification. These contain ten classes of distinct objects. In most of our experiments, we have used the leave-one-in protocol, where one of the classes is considered normal and the remaining are anomalous. Therefore, one classification image dataset with ten distinct classes is transformed into ten different anomaly detection sub-datasets. Finally, for the experiments with the SGVAEGAN model, we have created two completely artificial image datasets where the goal was to have images with prominent objects on a more or less unified background. Again, the basic statistics on image datasets are shown in Tab. B.3.

MNIST dataset [237] is a collection of greyscale images of handwritten digits and one of the most ubiquitous datasets used in machine learning due to its simplicity and easy interpretation.

FashionMNIST [246] is a classification dataset of low-resolution greyscale images of ten different classes of fashion articles, such as coats, shirts, or sandals. It is supposed to be slightly more difficult than the MNIST datasets.

SVHN2 is a well-known benchmark dataset [247] containing images of house numbers. In this cropped version of the dataset, the target digit is centered in the middle of the picture. However, there may be partial digits adjacent to it, which

B.2 Image datasets

dataset	alias	dim	anom	normal
ANNthyroid	ann	21	534	6665
Arrhythmia	arr	275	206	245
HAR	har	561	1944	8355
HTRU2	htr	8	1638	16257
KDD99 (10%)	kdd	118	396742	97276
Mammography	mam	6	260	10921
Seismic	sei	24	170	2412
Spambase	spm	57	1812	2786

Table B.1: Basic statistics (dimensionality, number of normal and anomalous samples) of the tabular dataset designed directly for anomaly detection.

makes the problem harder. Furthermore, there are no available annotations for the background/foreground factor and in this paper, it is included mainly as a benchmark for comparison to other baseline methods.

CIFAR10 is another classical dataset of images of 10 classes of different objects or animals often used for validation of anomaly detectors [38, 102, 94]. For an overview of the dataset see [248].

MNIST-C is an artificially created anomaly detection dataset introduced in [249]. It is created using digits from the MNIST datasets to which certain distortions and corruptions are added. The normal data in this case are the original MNIST images and the anomalies are their corrupted counterparts. There are 15 classes of corruptions, such as different types of blur, noise, or geometrical transformations. The difficulty of the detection of corrupted images varies a lot. While brightness change is usually very easy for most detectors, translation or rotation is sometimes very difficult, see the extended results in the Appendix of [213].

MVTec-AD is an industrial dataset [250] that captures several different problems of identifying faulty or damaged objects. We have included only some classes of the dataset that either represented an anomaly detection problem of a varying degree of difficulty or contained a prominent object in the foreground. The individual problems are smaller — on average about 200 normal and 100 anomalous samples. The images used in our experiments are downsampled to 128x128 pixels from the original size of 1024x1024.

Wildlife MNIST [236] is an artificial dataset based on the standard MNIST. For each MNIST digit, a background and foreground texture is sampled from a texture dataset described in [238] to create a colored version. Two versions of this dataset were created - *mixed* and *non-mixed*. In the mixed version, the background and foreground for each digit are sampled randomly from 10 background and foreground texture classes to create a very diverse set of images. In the non-mixed version, the background and foreground class is kept the same for all basic MNIST digits from the same class, resulting in a less diverse dataset. For examples of the

dataset		alias	dim	anom	normal
Abalone		aba	10	50	2151
Blood Transfusion		blt	4	16	382
Breast Cancer Wisconsin		bcw	30	206	356
Breast Tissue		bts	9	22	65
Cardiotocography		crd	27	228	1830
Ecoli		eco	7	108	205
Glass		gls	10	94	112
Haberman		hab	3	14	225
Ionosphere		ion	33	122	225
Iris		irs	4	46	100
Isolet		iso	617	3300	4496
Letter Recognition		ltr	617	3600	4196
Libras		lbr	90	142	215
Magic Telescope		mgc	10	3882	12331
Miniboone		mnb	50	23922	93565
Multiple Features		mlt	649	800	1200
PageBlocks		pgb	10	384	4911
Parkinsons		prk	22	44	146
Pendigits		pen	16	5384	5537
Pima Indians		pim	8	176	500
Sonar		snr	60	96	110
Spect Heart		sph	44	52	211
Statlog Satimage		sat	36	2630	3592
Statlog Segment		seg	18	938	1320
Statlog Shuttle		sht	8	28	57767
Statlog Vehicle		vhc	18	132	627
Synthetic Control Chart		scc	60	200	400
Wall Following Robot		wrb	24	2220	2921
Waveform-1		wf1	21	1482	3302
Waveform-2		wf2	21	1472	3302
Wine		wne	13	70	106
Yeast		yst	8	390	751

Table B.2: Basic statistics of the tabular multi-class datasets that were transformed into anomaly detection problems.

B.2 Image datasets

dataset	alias	dim	anom	normal
MNIST-C	mnistc	28x28x1	70000	70000
MVTec-AD - wood	wood	128x128x3	60	266
MVTec-AD - grid	grid	128x128x3	57	285
MVTec-AD - transistor	transistor	128x128x3	40	273
MVTec-AD - bottle	transistor	128x128x3	40	273
MVTec-AD - capsule	transistor	128x128x3	40	273
MVTec-AD - nut	transistor	128x128x3	40	273
MVTec-AD - pill	transistor	128x128x3	40	273
FashionMNIST	fashionmnist	28x28x1	63000	7000
MNIST	mnist	28x28x1	63686	6312
CIFAR10	cifar10	32x32x3	54000	6000
SVHN2	svhn2	32x32x3	80327	18960
Wildlife MNIST	wmnist	32x32x3	54000	6000
COCOPlaces	coco	64x64x3	4500	500

Table B.3: Basic statistics of image datasets. Note that the numbers of normal and anomalous samples are approximate, as each dataset (apart from MVTec-AD) has 10 classes of data and some datasets have an uneven distribution of the number of samples in these classes.

non-mixed version, see the top row of Fig. 5.1. Each version contains 60000 samples of RGB images with three factors of variation.

COCOPlaces is a dataset created similarly to Wildlife MNIST. 10 classes of objects from the COCO dataset [251] were combined with 10 background classes from the Places dataset [252]. Again, mixed and non-mixed variants were created. Because the object shape and texture cannot be separated in this case, it represents a problem with two factors of variation that is slightly more realistic than the previous one. Furthermore, it is much harder, as the object shapes are very distinct, sometimes the foreground object is only partially visible and the background itself may sometimes contain some other objects as well. A total of 5000 RGB images were generated for each variant. For sample images of all classes, see Fig. B.1.



Figure B.1: Samples from the semantic image datasets and the MvTec-AD dataset which were used in the experiments. Datasets from the top row to bottom: CO-COPPlaces, CIFAR10, SVHN2, and MVTec-AD. MVTec-AD examples of normal and anomalous samples from the *bottle*, *capsule*, *metal nut*, *pill*, and *transistor* classes are shown.

C

Additional resources

Most of the datasets from Appendix B are publicly available. The Wildlife MNIST and COCOPlaces datasets were created and published by the author of this thesis and are available at <https://zenodo.org/record/7602025> and <https://zenodo.org/record/7612053>. The data that were produced during the extensive experimental comparison are not publicly available, since they exceed 10TB in size, but the model performance metrics from experiments in Chapters 4 and 5 are available upon request from the authors.

Most of the models which were experimented with experiments were implemented either mostly in the Julia [253] language, with the exception of the SGVAEGAN model, which was implemented in PyTorch [254]. Now we list the publicly available repositories used in the creation of this thesis.

1. Repository <https://github.com/vitskvara/UCI.jl> provides easy access to anomaly benchmark datasets that were created from classification problems in the UCI dataset database. This was used for the experiments with tabular data in Chapter 4.
2. Repository <https://github.com/vitskvara/AlfvenDetectors.jl> is a collection of model code and utilities for experiments on Alfvén detection that was described in Sec. 3.4.
3. Repository <https://github.com/aicenter/GenerativeModels.jl> contains a very general interface for training and evaluation of basic generative models.
4. Repository github.com/vitskvara/GenerativeAD.jl compiles the experimental framework used for the large-scale experimental comparisons in Chapters 4 and 5.
5. Finally, the repository github.com/vitskvara/sgad contains the PyTorch implementation of the SGVAEGAN model.

Bibliography

- [1] JWL Glaisher. On the rejection of discordant observations. *Monthly Notices of the Royal Astronomical Society*, 33:391–402, 1873.
- [2] Francis Ysidro Edgeworth. On discordant observations. *The London, Edinburgh, and Dublin philosophical magazine and journal of science*, 23(143):364–375, 1887.
- [3] Hung-Jen Liao, Chun-Hung Richard Lin, Ying-Chih Lin, and Kuang-Yuan Tung. Intrusion detection system: A comprehensive review. *Journal of Network and Computer Applications*, 36(1):16–24, 2013.
- [4] Juan Vanerio and Pedro Casas. Ensemble-learning approaches for network security and anomaly detection. In *Proceedings of the Workshop on Big Data Analytics and Machine Learning for Data Communication Networks*, pages 1–6, 2017.
- [5] Yang Xin, Lingshuang Kong, Zhi Liu, Yuling Chen, Yanmiao Li, Hongliang Zhu, Mingcheng Gao, Haixia Hou, and Chunhua Wang. Machine learning and deep learning methods for cybersecurity. *Ieee access*, 6:35365–35381, 2018.
- [6] Richard J Bolton and David J Hand. Statistical fraud detection: A review. *Statistical science*, 17(3):235–255, 2002.
- [7] Johan Perols. Financial statement fraud detection: An analysis of statistical and machine learning algorithms. *Auditing: A Journal of Practice & Theory*, 30(2):19–50, 2011.
- [8] Mohiuddin Ahmed, Abdun Naser Mahmood, and Md Rafiqul Islam. A survey of anomaly detection techniques in financial domain. *Future Generation Computer Systems*, 55:278–288, 2016.
- [9] Lionel Tarassenko, Paul Hayton, Nicholas Cerneaz, and Michael Brady. Novelty detection for the identification of masses in mammograms. *International Conference on Artificial Neural Networks*, 1995.
- [10] Weng-Keen Wong, Andrew W Moore, Gregory F Cooper, and Michael M Wagner. Bayesian network anomaly pattern detection for disease outbreaks. In *Proceedings of the 20th International Conference on Machine Learning (ICML-03)*, pages 808–815, 2003.
- [11] Dimitris K Iakovidis, Spiros V Georgakopoulos, Michael Vasilakakis, Anastasios Koulaouzidis, and Vassilis P Plagianakos. Detecting and locating gastrointestinal anomalies using deep learning and iterative cluster unification. *IEEE transactions on medical imaging*, 37(10):2196–2210, 2018.

Bibliography

- [12] Joey Tianyi Zhou, Jiawei Du, Hongyuan Zhu, Xi Peng, Yong Liu, and Rick Siow Mong Goh. Anomalynet: An anomaly detection network for video surveillance. *IEEE Transactions on Information Forensics and Security*, 14(10):2537–2550, 2019.
- [13] Mohamad Mahmoudi, Ahmed Aziz Ezzat, and Alaa Elwany. Layerwise anomaly detection in laser powder-bed fusion metal additive manufacturing. *Journal of Manufacturing Science and Engineering*, 141(3), 2019.
- [14] Mingliang Bai, Jinfu Liu, Jinhua Chai, Xinyu Zhao, and Daren Yu. Anomaly detection of gas turbines based on normal pattern extraction. *Applied Thermal Engineering*, 166:114664, 2020.
- [15] Yeji Choi, Hyunki Lim, Heeseung Choi, and Ig-Jae Kim. Gan-based anomaly detection and localization of multivariate time series data for power plant. In *2020 IEEE international conference on big data and smart computing (BigComp)*, pages 71–74. IEEE, 2020.
- [16] Pavlos Protopapas, JM Giammarco, L Faccioli, MF Struble, Rahul Dave, and Charles Alcock. Finding outlier light curves in catalogues of periodic variable stars. *Monthly Notices of the Royal Astronomical Society*, 369(2):677–696, 2006.
- [17] Vít Škvára, Tomáš Pevný, Václav Šmídl, Jakub Seidl, Aleš Havránek, and David Tskhakaya. Detection of Alfvén eigenmodes on COMPASS with generative neural networks. *Fusion Science and Technology*, 76(8):962–971, 2020.
- [18] Tudor I Oprea. Chemical space navigation in lead discovery. *Current opinion in chemical biology*, 6(3):384–389, 2002.
- [19] Katherine Fraser, Samuel Homiller, Rashmish K Mishra, Bryan Ostdiek, and Matthew D Schwartz. Challenges for unsupervised anomaly detection in particle physics. *Journal of High Energy Physics*, 2022(3):1–31, 2022.
- [20] Fei Tony Liu, Kai Ming Ting, and Zhi-Hua Zhou. Isolation forest. In *2008 Eighth IEEE International Conference on Data Mining*, pages 413–422. IEEE, 2008.
- [21] Stefan Harmeling, Guido Dornhege, David Tax, Frank Meinecke, and Klaus-Robert Müller. From outliers to prototypes: ordering data. *Neurocomputing*, 69(13-15):1608–1618, 2006.
- [22] Vijay Mahadevan, Weixin Li, Viral Bhalodia, and Nuno Vasconcelos. Anomaly detection in crowded scenes. In *Computer Vision and Pattern Recognition (CVPR), 2010 IEEE Conference on*, pages 1975–1981. IEEE, 2010.
- [23] Thomas Schlegl, Philipp Seeböck, Sebastian M Waldstein, Ursula Schmidt-Erfurth, and Georg Langs. Unsupervised anomaly detection with generative adversarial networks to guide marker discovery. In *International Conference on Information Processing in Medical Imaging*, pages 146–157. Springer, 2017.
- [24] Tomáš Pevný. Loda: Lightweight on-line detector of anomalies. *Machine Learning*, 102(2):275–304, 2016.

- [25] Longin Jan Latecki, Aleksandar Lazarevic, and Dragoljub Pokrajac. Outlier detection with kernel density functions. In *International Workshop on Machine Learning and Data Mining in Pattern Recognition*, pages 61–75. Springer, 2007.
- [26] Bernhard Schölkopf, John C Platt, John Shawe-Taylor, Alex J Smola, and Robert C Williamson. Estimating the support of a high-dimensional distribution. *Neural computation*, 13(7):1443–1471, 2001.
- [27] Marco AF Pimentel, David A Clifton, Lei Clifton, and Lionel Tarassenko. A review of novelty detection. *Signal Processing*, 99:215–249, 2014.
- [28] Markus Goldstein and Seiichi Uchida. A comparative evaluation of unsupervised anomaly detection algorithms for multivariate data. *PloS one*, 11(4):e0152173, 2016.
- [29] Aleksandar Lazarevic, Levent Ertoz, Vipin Kumar, Aysel Ozgur, and Jaideep Srivastava. A comparative study of anomaly detection schemes in network intrusion detection. In *Proceedings of the 2003 SIAM International Conference on Data Mining*, pages 25–36. SIAM, 2003.
- [30] Varun Chandola, Arindam Banerjee, and Vipin Kumar. Anomaly detection: A survey. *ACM computing surveys (CSUR)*, 41(3):15, 2009.
- [31] Guilherme O Campos, Arthur Zimek, Jörg Sander, Ricardo JGB Campello, Barbora Micenková, Erich Schubert, Ira Assent, and Michael E Houle. On the evaluation of unsupervised outlier detection: measures, datasets, and an empirical study. *Data Mining and Knowledge Discovery*, 30(4):891–927, 2016.
- [32] Ian Goodfellow, Jean Pouget-Abadie, Mehdi Mirza, Bing Xu, David Warde-Farley, Sherjil Ozair, Aaron Courville, and Yoshua Bengio. Generative adversarial nets. In *Advances in neural information processing systems*, pages 2672–2680, 2014.
- [33] Diederik P Kingma and Max Welling. Auto-encoding variational bayes. *arXiv preprint arXiv:1312.6114*, 2013.
- [34] Laurent Dinh, David Krueger, and Yoshua Bengio. Nice: Non-linear independent components estimation. *arXiv preprint arXiv:1410.8516*, 2014.
- [35] Lukas Ruff, Jacob R Kauffmann, Robert A Vandermeulen, Grégoire Montavon, Wojciech Samek, Marius Kloft, Thomas G Dietterich, and Klaus-Robert Müller. A Unifying Review of Deep and Shallow Anomaly Detection. *arXiv:2009.11732 [cs]*, 2020.
- [36] Edwin M. Knorr and Raymond T. Ng. Algorithms for mining distance-based outliers in large datasets. In Ashish Gupta, Oded Shmueli, and Jennifer Widom, editors, *VLDB’98, Proceedings of 24rd International Conference on Very Large Data Bases, August 24–27, 1998, New York City, New York, USA*, pages 392–403. Morgan Kaufmann, 1998.
- [37] Victoria Hodge and Jim Austin. A survey of outlier detection methodologies. *Artificial intelligence review*, 22(2):85–126, 2004.

Bibliography

- [38] Lukas Ruff, Robert Vandermeulen, Nico Goernitz, Lucas Deecke, Shoaib Ahmed Siddiqui, Alexander Binder, Emmanuel Müller, and Marius Kloft. Deep one-class classification. In *International conference on machine learning*, pages 4393–4402, 2018.
- [39] Shiyu Liang, Yixuan Li, and Rayadurgam Srikant. Enhancing the reliability of out-of-distribution image detection in neural networks. *arXiv preprint arXiv:1706.02690*, 2017.
- [40] Vic Barnett and Toby Lewis. *Outliers in statistical data*. Wiley, 1974.
- [41] Emanuel Parzen. On estimation of a probability density function and mode. *The annals of mathematical statistics*, 33(3):1065–1076, 1962.
- [42] Shai Ben-David and Michael Lindenbaum. Learning distributions by their density levels: A paradigm for learning without a teacher. *Journal of Computer and System Sciences*, 55(1):171–182, 1997.
- [43] Wolfgang Polonik. Minimum volume sets and generalized quantile processes. *Stochastic processes and their applications*, 69(1):1–24, 1997.
- [44] Fabian Pedregosa, Gaël Varoquaux, Alexandre Gramfort, Vincent Michel, Bertrand Thirion, Olivier Grisel, Mathieu Blondel, Peter Prettenhofer, Ron Weiss, Vincent Dubourg, et al. Scikit-learn: Machine learning in Python. *Journal of machine learning research*, 12(Oct):2825–2830, 2011.
- [45] Muhammad Qasim Ali, Ehab Al-Shaer, Hassan Khan, and Syed Ali Khayam. Automated anomaly detector adaptation using adaptive threshold tuning. *ACM Transactions on Information and System Security (TISSEC)*, 15(4):1–30, 2013.
- [46] Mohiuddin Ahmed. Collective anomaly detection techniques for network traffic analysis. *Annals of data science*, 5(4):497–512, 2018.
- [47] Gwenolé Quellec, Mathieu Lamard, Michel Cozic, Gouenou Coatrieux, and Guy Cazuguel. Multiple-instance learning for anomaly detection in digital mammography. *IEEE transactions on medical imaging*, 35(7):1604–1614, 2016.
- [48] Boyang Wan, Yuming Fang, Xue Xia, and Jiajie Mei. Weakly supervised video anomaly detection via center-guided discriminative learning. In *2020 IEEE International Conference on Multimedia and Expo (ICME)*, pages 1–6. IEEE, 2020.
- [49] Marc-André Carbonneau, Veronika Cheplygina, Eric Granger, and Ghyslain Gagnon. Multiple instance learning: A survey of problem characteristics and applications. *Pattern Recognition*, 77:329–353, 2018.
- [50] Ruey S Tsay, Daniel Pena, and Alan E Pankratz. Outliers in multivariate time series. *Biometrika*, 87(4):789–804, 2000.
- [51] Sanjay Chawla and Pei Sun. SLOM: a new measure for local spatial outliers. *Knowledge and Information Systems*, 9(4):412–429, 2006.
- [52] Faruk Ahmed and Aaron Courville. Detecting semantic anomalies. In *Proceedings of the AAAI Conference on Artificial Intelligence*, volume 34, pages 3154–3162, 2020.

- [53] Vít Škvára, Tomáš Pevný, and Václav Šmídl. Is AUC the best measure for practical comparison of anomaly detectors? *arXiv:2305.04754 [cs]*, 2023.
- [54] David J Hand and Robert J Till. A simple generalisation of the area under the ROC curve for multiple class classification problems. *Machine learning*, 45(2):171–186, 2001.
- [55] Stéphan Cléménçon and Jérémie Jakubowicz. Scoring anomalies: a M-estimation formulation. In *Artificial Intelligence and Statistics*, pages 659–667, 2013.
- [56] Christian P Robert, George Casella, Christian P Robert, and George Casella. Monte carlo integration. *Monte Carlo statistical methods*, pages 71–138, 1999.
- [57] Nicolas Goix. How to evaluate the quality of unsupervised anomaly detection algorithms? *arXiv preprint arXiv:1607.01152*, 2016.
- [58] Nour Moustafa, Jiankun Hu, and Jill Slay. A holistic review of network anomaly detection systems: A comprehensive survey. *Journal of Network and Computer Applications*, 128:33–55, 2019.
- [59] Donghwoon Kwon, Hyunjoo Kim, Jinoh Kim, Sang C Suh, Ikkyun Kim, and Kuinam J Kim. A survey of deep learning-based network anomaly detection. *Cluster Computing*, pages 1–13, 2019.
- [60] Gilberto Fernandes, Joel JPC Rodrigues, Luiz Fernando Carvalho, Jalal F Al-Muhtadi, and Mario Lemes Proen  a. A comprehensive survey on network anomaly detection. *Telecommunication Systems*, 70(3):447–489, 2019.
- [61] Hongzhi Wang, Mohamed Jaward Bah, and Mohamed Hammad. Progress in outlier detection techniques: A survey. *IEEE Access*, 7:107964–108000, 2019.
- [62] Raghavendra Chalapathy and Sanjay Chawla. Deep learning for anomaly detection: A survey. *arXiv:1901.03407 [cs]*, 2019.
- [63] Frank E Grubbs. Procedures for detecting outlying observations in samples. *Technometrics*, 11(1):1–21, 1969.
- [64] Vic Barnett, Toby Lewis, et al. *Outliers in statistical data*, volume 3. Wiley New York, 1994.
- [65] Jorma Laurikkala, Martti Juhola, Erna Kentala, N Lavrac, S Miksch, and B Kavsek. Informal identification of outliers in medical data. In *Fifth international workshop on intelligent data analysis in medicine and pharmacology*, volume 1, pages 20–24. Citeseer, 2000.
- [66] Stephen Roberts and Lionel Tarassenko. A probabilistic resource allocating network for novelty detection. *Neural Computation*, 6(2):270–284, 1994.
- [67] Arthur P Dempster, Nan M Laird, and Donald B Rubin. Maximum likelihood from incomplete data via the EM algorithm. *Journal of the Royal Statistical Society: Series B (Methodological)*, 39(1):1–22, 1977.

Bibliography

- [68] Christopher M Bishop. *Pattern recognition and machine learning*. Springer, 2006.
- [69] Stephen W Hoare, David Asbridge, and Paul CW Beatty. On-line novelty detection for artefact identification in automatic anaesthesia record keeping. *Medical engineering & physics*, 24(10):673–681, 2002.
- [70] Dit-Yan Yeung and Yuxin Ding. Host-based intrusion detection using dynamic and static behavioral models. *Pattern recognition*, 36(1):229–243, 2003.
- [71] Xiaoqiang Zhang, Pingzhi Fan, and Zhongliang Zhu. A new anomaly detection method based on hierarchical HMM. In *Proceedings of the Fourth International Conference on Parallel and Distributed Computing, Applications and Technologies*, pages 249–252. IEEE, 2003.
- [72] Matt P Wand and M Chris Jones. *Kernel smoothing*. CRC press, 1994.
- [73] Dit-Yan Yeung and Calvin Chow. Parzen-window network intrusion detectors. In *2002 International Conference on Pattern Recognition*, volume 4, pages 385–388. IEEE, 2002.
- [74] Markus Goldstein and Andreas Dengel. Histogram-based outlier score (hbos): A fast unsupervised anomaly detection algorithm. *KI-2012: Poster and Demo Track*, pages 59–63, 2012.
- [75] Bo Zong, Qi Song, Martin Renqiang Min, Wei Cheng, Cristian Lumezanu, Daeki Cho, and Haifeng Chen. Deep autoencoding gaussian mixture model for unsupervised anomaly detection. In *International Conference on Learning Representations*, 2018.
- [76] Geoffrey E Hinton. Training products of experts by minimizing contrastive divergence. *Neural computation*, 14(8):1771–1800, 2002.
- [77] Geoffrey E Hinton, Simon Osindero, and Yee-Whye Teh. A fast learning algorithm for deep belief nets. *Neural computation*, 18(7):1527–1554, 2006.
- [78] Ruslan Salakhutdinov and Hugo Larochelle. Efficient learning of deep Boltzmann machines. In *Proceedings of the thirteenth international conference on artificial intelligence and statistics*, pages 693–700. JMLR Workshop and Conference Proceedings, 2010.
- [79] Shuangfei Zhai, Yu Cheng, Weining Lu, and Zhongfei Zhang. Deep structured energy based models for anomaly detection. *arXiv preprint arXiv:1605.07717*, 2016.
- [80] Sridhar Ramaswamy, Rajeev Rastogi, and Kyuseok Shim. Efficient algorithms for mining outliers from large data sets. In *ACM Sigmod Record*, volume 29, pages 427–438. ACM, 2000.
- [81] Jon Louis Bentley. Multidimensional binary search trees used for associative searching. *Communications of the ACM*, 18(9):509–517, 1975.
- [82] Jeff Johnson, Matthijs Douze, and Hervé Jégou. Billion-scale similarity search with GPUs. *IEEE Transactions on Big Data*, 7(3):535–547, 2019.

- [83] Guansong Pang, Longbing Cao, Ling Chen, and Huan Liu. Learning Representations of Ultrahigh-dimensional Data for Random Distance-based Outlier Detection. *arXiv:1806.04808 [cs, stat]*, June 2018.
- [84] Markus M Breunig, Hans-Peter Kriegel, Raymond T Ng, and Jörg Sander. LOF: identifying density-based local outliers. In *ACM sigmod record*, volume 29, pages 93–104. ACM, 2000.
- [85] Jian Tang, Zhixiang Chen, Ada Wai-Chee Fu, and David W Cheung. Enhancing effectiveness of outlier detections for low density patterns. In *Pacific-Asia Conference on Knowledge Discovery and Data Mining*, pages 535–548. Springer, 2002.
- [86] Zengyou He, Xiaofei Xu, and Shengchun Deng. Discovering cluster-based local outliers. *Pattern Recognition Letters*, 24(9-10):1641–1650, 2003.
- [87] Parikshit Gopalan, Vatsal Sharan, and Udi Wieder. PIDForest: Anomaly Detection via Partial Identification. *arXiv:1912.03582 [cs]*, 2019.
- [88] Hans-Peter Kriegel, Matthias Schubert, and Arthur Zimek. Angle-based outlier detection in high-dimensional data. In *Proceedings of the 14th ACM SIGKDD international conference on Knowledge discovery and data mining*, pages 444–452, 2008.
- [89] John Shawe-Taylor, Nello Cristianini, et al. *Kernel methods for pattern analysis*. Cambridge university press, 2004.
- [90] Corinna Cortes and Vladimir Vapnik. Support-vector networks. *Machine learning*, 20:273–297, 1995.
- [91] Stefan Van Aelst and Peter Rousseeuw. Minimum volume ellipsoid. *Wiley Interdisciplinary Reviews: Computational Statistics*, 1(1):71–82, 2009.
- [92] Nico Görnitz, Luiz Alberto Lima, Klaus-Robert Müller, Marius Kloft, and Shinichi Nakajima. Support vector data descriptions and k -means clustering: one class? *IEEE transactions on neural networks and learning systems*, 29(9):3994–4006, 2017.
- [93] Alireza Ghasemi, Hamid R Rabiee, Mohammad Taghi Manzuri, and Mohammad Hossein Rohban. A bayesian approach to the data description problem. In *Proceedings of the AAAI Conference on Artificial Intelligence*, volume 26, pages 907–913, 2012.
- [94] Raghavendra Chalapathy, Aditya Krishna Menon, and Sanjay Chawla. Anomaly detection using one-class neural networks. *arXiv:1802.06360 [cs]*, 2019.
- [95] Sarah M Erfani, Sutharshan Rajasegarar, Shanika Karunasekera, and Christopher Leckie. High-dimensional and large-scale anomaly detection using a linear one-class SVM with deep learning. *Pattern Recognition*, 58:121–134, 2016.
- [96] Zahra Ghafoori and Christopher Leckie. Deep multi-sphere support vector data description. In *Proceedings of the 2020 SIAM International Conference on Data Mining*, pages 109–117. SIAM, 2020.

Bibliography

- [97] Ingo Steinwart, Don Hush, and Clint Scovel. A classification framework for anomaly detection. *Journal of Machine Learning Research*, 6(Feb):211–232, 2005.
- [98] Wei Fan, Matthew Miller, Sal Stolfo, Wenke Lee, and Phil Chan. Using artificial anomalies to detect unknown and known network intrusions. *Knowledge and Information Systems*, 6:507–527, 2004.
- [99] Dan Hendrycks, Mantas Mazeika, and Thomas Dietterich. Deep Anomaly Detection with Outlier Exposure. *arXiv:1812.04606 [cs, stat]*, January 2019.
- [100] Dan Hendrycks, Mantas Mazeika, Saurav Kadavath, and Dawn Song. Using self-supervised learning can improve model robustness and uncertainty. *Advances in neural information processing systems*, 32, 2019.
- [101] Zhi-Hua Zhou. A brief introduction to weakly supervised learning. *National science review*, 5(1):44–53, 2018.
- [102] Lukas Ruff, Robert A Vandermeulen, Nico Görnitz, Alexander Binder, Emmanuel Müller, Klaus-Robert Müller, and Marius Kloft. Deep semi-supervised anomaly detection. *arXiv preprint arXiv:1906.02694*, 2019.
- [103] Philipp Liznerski, Lukas Ruff, Robert A Vandermeulen, Billy Joe Franks, Marius Kloft, and Klaus-Robert Müller. Explainable deep one-class classification. *arXiv preprint arXiv:2007.01760*, 2020.
- [104] Naoki Abe, Bianca Zadrozny, and John Langford. Outlier detection by active learning. In *Proceedings of the 12th ACM SIGKDD international conference on Knowledge discovery and data mining*, pages 504–509, 2006.
- [105] Alexander Kolesnikov, Xiaohua Zhai, and Lucas Beyer. Revisiting self-supervised visual representation learning. In *Proceedings of the IEEE/CVF conference on computer vision and pattern recognition*, pages 1920–1929, 2019.
- [106] Ting Chen, Simon Kornblith, Mohammad Norouzi, and Geoffrey Hinton. A simple framework for contrastive learning of visual representations. In *International conference on machine learning*, pages 1597–1607. PMLR, 2020.
- [107] Izhak Golan and Ran El-Yaniv. Deep anomaly detection using geometric transformations. *Advances in neural information processing systems*, 31, 2018.
- [108] Liron Bergman and Yedid Hoshen. Classification-based anomaly detection for general data. *arXiv preprint arXiv:2005.02359*, 2020.
- [109] Mei-Ling Shyu, Shu-Ching Chen, Kanoksri Sarinnapakorn, and LiWu Chang. A novel anomaly detection scheme based on principal component classifier. Technical report, MIAMI UNIV CORAL GABLES FL DEPT OF ELECTRICAL AND COMPUTER ENGINEERING, 2003.
- [110] Charu C Aggarwal. Outlier analysis. In *Data mining*, pages 237–263. Springer, 2015.
- [111] Bernhard Schölkopf, Alexander Smola, and Klaus-Robert Müller. Nonlinear component analysis as a kernel eigenvalue problem. *Neural computation*, 10(5):1299–1319, 1998.

-
- [112] Yingchao Xiao, Huangang Wang, Wenli Xu, and Junwu Zhou. L1 norm based KPCA for novelty detection. *Pattern Recognition*, 46(1):389–396, 2013.
 - [113] Mark A Kramer. Nonlinear principal component analysis using autoassociative neural networks. *AIChE journal*, 37(2):233–243, 1991.
 - [114] Diederik P. Kingma and Jimmy Ba. Adam: A Method for Stochastic Optimization. *arXiv:1412.6980 [cs]*, 2017.
 - [115] Sashank J Reddi, Satyen Kale, and Sanjiv Kumar. On the convergence of adam and beyond. *arXiv preprint arXiv:1904.09237*, 2019.
 - [116] Paul J Werbos. Applications of advances in nonlinear sensitivity analysis. In *System modeling and optimization*, pages 762–770. Springer, 1982.
 - [117] Jun Deng, Zixing Zhang, Erik Marchi, and Björn Schuller. Sparse autoencoder-based feature transfer learning for speech emotion recognition. In *2013 humaine association conference on affective computing and intelligent interaction*, pages 511–516. IEEE, 2013.
 - [118] Xugang Lu, Yu Tsao, Shigeki Matsuda, and Chiori Hori. Speech enhancement based on deep denoising autoencoder. In *Interspeech*, volume 2013, pages 436–440, 2013.
 - [119] Eric Kauderer-Abrams. Quantifying translation-invariance in convolutional neural networks. *arXiv preprint arXiv:1801.01450*, 2017.
 - [120] Mayu Sakurada and Takehisa Yairi. Anomaly detection using autoencoders with nonlinear dimensionality reduction. In *Proceedings of the MLSDA 2014 2nd Workshop on Machine Learning for Sensory Data Analysis*, page 4. ACM, 2014.
 - [121] Benjamin Berry Thompson, Robert J Marks, Jai J Choi, Mohamed A El-Sharkawi, Ming-Yuh Huang, and Carl Bunje. Implicit learning in autoencoder novelty assessment. In *Neural Networks, 2002. IJCNN’02. Proceedings of the 2002 International Joint Conference on*, volume 3, pages 2878–2883. IEEE, 2002.
 - [122] Tsatsral Amarbayasgalan, Bilguun Jargalsaikhan, and Keun Ho Ryu. Unsupervised novelty detection using deep autoencoders with density based clustering. *Applied Sciences*, 8(9):1468, 2018.
 - [123] Andrew Ng and Michael Jordan. On discriminative vs. generative classifiers: A comparison of logistic regression and naive bayes. *Advances in neural information processing systems*, 14, 2001.
 - [124] Christopher Bishop and Julia Lasserre. Generative or discriminative? getting the best of both worlds. *Bayesian statistics*, 8(3):3–24, 2007.
 - [125] Andrew Brock, Jeff Donahue, and Karen Simonyan. Large scale GAN training for high fidelity natural image synthesis. *arXiv preprint arXiv:1809.11096*, 2018.
 - [126] Tom Brown, Benjamin Mann, Nick Ryder, Melanie Subbiah, Jared D Kaplan, Prafulla Dhariwal, Arvind Neelakantan, Pranav Shyam, Girish Sastry, Amanda Askell, et al. Language models are few-shot learners. *Advances in neural information processing systems*, 33:1877–1901, 2020.

Bibliography

- [127] Prafulla Dhariwal, Heewoo Jun, Christine Payne, Jong Wook Kim, Alec Radford, and Ilya Sutskever. Jukebox: A generative model for music. *arXiv preprint arXiv:2005.00341*, 2020.
- [128] Jascha Sohl-Dickstein, Eric Weiss, Niru Maheswaranathan, and Surya Ganguli. Deep unsupervised learning using nonequilibrium thermodynamics. In *International Conference on Machine Learning*, pages 2256–2265. PMLR, 2015.
- [129] Chitwan Saharia, William Chan, Saurabh Saxena, Lala Li, Jay Whang, Emily Denton, Seyed Kamyar Seyed Ghasemipour, Burcu Karagol Ayan, S Sara Mahdavi, Rapha Gontijo Lopes, et al. Photorealistic text-to-image diffusion models with deep language understanding. *arXiv preprint arXiv:2205.11487*, 2022.
- [130] Jinwon An and Sungzoon Cho. Variational autoencoder based anomaly detection using reconstruction probability. *SNU Data Mining Center, Tech. Rep.*, 2015.
- [131] Haowen Xu, Wenxiao Chen, Nengwen Zhao, Zeyan Li, Jiahao Bu, Zhihan Li, Ying Liu, Youjian Zhao, Dan Pei, Yang Feng, et al. Unsupervised anomaly detection via variational auto-encoder for seasonal kpis in web applications. In *Proceedings of the 2018 World Wide Web Conference*, pages 187–196, 2018.
- [132] Huan-gang Wang, Xin Li, and Tao Zhang. Generative adversarial network based novelty detection using minimized reconstruction error. *Frontiers of Information Technology & Electronic Engineering*, 19(1):116–125, 2018.
- [133] Pramuditha Perera, Ramesh Nallapati, and Bing Xiang. Ocgan: One-class novelty detection using GANs with constrained latent representations. In *Proceedings of the IEEE Conference on Computer Vision and Pattern Recognition*, pages 2898–2906, 2019.
- [134] Masataka Yamaguchi, Yuma Koizumi, and Noboru Harada. AdaFlow: Domain-adaptive density estimator with application to anomaly detection and unpaired cross-domain translation. In *ICASSP 2019-2019 IEEE International Conference on Acoustics, Speech and Signal Processing (ICASSP)*, pages 3647–3651. IEEE, 2019.
- [135] Maximilian Schmidt and Marko Simic. Normalizing flows for novelty detection in industrial time series data. *arXiv:1906.06904 [cs, stat]*, June 2019.
- [136] William Lotter, Gabriel Kreiman, and David Cox. Unsupervised learning of visual structure using predictive generative networks. *arXiv preprint arXiv:1511.06380*, 2015.
- [137] Tim Salimans, Ian Goodfellow, Wojciech Zaremba, Vicki Cheung, Alec Radford, and Xi Chen. Improved techniques for training gans. In *Advances in Neural Information Processing Systems*, pages 2234–2242, 2016.
- [138] Jun-Yan Zhu, Philipp Krähenbühl, Eli Shechtman, and Alexei A Efros. Generative visual manipulation on the natural image manifold. In *European Conference on Computer Vision*, pages 597–613. Springer, 2016.
- [139] Ting-Chun Wang, Ming-Yu Liu, Jun-Yan Zhu, Andrew Tao, Jan Kautz, and Bryan Catanzaro. High-resolution image synthesis and semantic manipulation with

- conditional gans. In *Proceedings of the IEEE conference on computer vision and pattern recognition*, pages 8798–8807, 2018.
- [140] Tero Karras, Samuli Laine, and Timo Aila. A style-based generator architecture for generative adversarial networks. In *Proceedings of the IEEE/CVF conference on computer vision and pattern recognition*, pages 4401–4410, 2019.
- [141] Sang-gil Lee, Wei Ping, Boris Ginsburg, Bryan Catanzaro, and Sungroh Yoon. Bigvgan: A universal neural vocoder with large-scale training. *arXiv preprint arXiv:2206.04658*, 2022.
- [142] Michael Maschler, Shmuel Zamir, and Eilon Solan. *Game theory*. Cambridge University Press, 2020.
- [143] Jie Gui, Zhenan Sun, Yonggang Wen, Dacheng Tao, and Jieping Ye. A review on generative adversarial networks: Algorithms, theory, and applications. *IEEE transactions on knowledge and data engineering*, 2021.
- [144] Ian Goodfellow. NIPS 2016 Tutorial: Generative Adversarial Networks. *arXiv:1701.00160 [cs]*, 2017.
- [145] Yongjun Hong, Uiwon Hwang, Jaeyoon Yoo, and Sungroh Yoon. How generative adversarial networks and their variants work: An overview. *ACM Computing Surveys (CSUR)*, 52(1):1–43, 2019.
- [146] Thomas Schlegl, Philipp Seeböck, Sebastian M. Waldstein, Georg Langs, and Ursula Schmidt-Erfurth. F-AnoGAN: Fast unsupervised anomaly detection with generative adversarial networks. *Medical Image Analysis*, 54:30–44, May 2019.
- [147] Ishaan Gulrajani, Faruk Ahmed, Martin Arjovsky, Vincent Dumoulin, and Aaron C Courville. Improved training of Wasserstein gans. *Advances in neural information processing systems*, 30, 2017.
- [148] Ilyass Haloui, Jayant Sen Gupta, and Vincent Feuillard. Anomaly detection with Wasserstein GAN. *arXiv preprint arXiv:1812.02463*, 2018.
- [149] Mark Kliger and Shachar Fleishman. Novelty Detection with GAN. *arXiv:1802.10560 [cs]*, 2018.
- [150] Houssam Zenati, Chuan Sheng Foo, Bruno Lecouat, Gaurav Manek, and Vijay Ramaseshan Chandrasekhar. Efficient GAN-Based Anomaly Detection. *arXiv:1802.06222 [cs]*, 2019.
- [151] Yezheng Liu, Zhe Li, Chong Zhou, Yuanchun Jiang, Jianshan Sun, Meng Wang, and Xiangnan He. Generative adversarial active learning for unsupervised outlier detection. *IEEE Transactions on Knowledge and Data Engineering*, 2019.
- [152] Jeff Donahue, Philipp Krähenbühl, and Trevor Darrell. Adversarial Feature Learning. *arXiv:1605.09782 [cs]*, 2017.
- [153] Valentin Leveau and Alexis Joly. Adversarial autoencoders for novelty detection. Research report, Inria - Sophia Antipolis, February 2017.

Bibliography

- [154] Diederik P Kingma, Max Welling, et al. An introduction to variational autoencoders. *Foundations and Trends® in Machine Learning*, 12(4):307–392, 2019.
- [155] Danilo Jimenez Rezende, Shakir Mohamed, and Daan Wierstra. Stochastic backpropagation and approximate inference in deep generative models. *arXiv preprint arXiv:1401.4082*, 2014.
- [156] Samuel R Bowman, Luke Vilnis, Oriol Vinyals, Andrew M Dai, Rafal Jozefowicz, and Samy Bengio. Generating sentences from a continuous space. *arXiv preprint arXiv:1511.06349*, 2015.
- [157] Durk P Kingma, Shakir Mohamed, Danilo Jimenez Rezende, and Max Welling. Semi-supervised learning with deep generative models. In *Advances in neural information processing systems*, pages 3581–3589, 2014.
- [158] Kihyuk Sohn, Honglak Lee, and Xinchen Yan. Learning structured output representation using deep conditional generative models. In *Advances in neural information processing systems*, pages 3483–3491, 2015.
- [159] Jacob Walker, Carl Doersch, Abhinav Gupta, and Martial Hebert. An uncertain future: Forecasting from static images using variational autoencoders. In *European Conference on Computer Vision*, pages 835–851. Springer, 2016.
- [160] Maximilian Söлch, Justin Bayer, Marvin Ludersdorfer, and Patrick van der Smagt. Variational inference for on-line anomaly detection in high-dimensional time series. *arXiv preprint arXiv:1602.07109*, 2016.
- [161] Irina Higgins, Loic Matthey, Arka Pal, Christopher Burgess, Xavier Glorot, Matthew Botvinick, Shakir Mohamed, and Alexander Lerchner. beta-VAE: Learning Basic Visual Concepts with a Constrained Variational Framework. *ICLR*, 2(5):6, 2017.
- [162] Shengjia Zhao, Jiaming Song, and Stefano Ermon. Infovae: Information maximizing variational autoencoders. *arXiv:1706.02262 [cs]*, 2018.
- [163] Ilya Tolstikhin, Olivier Bousquet, Sylvain Gelly, and Bernhard Schoelkopf. Wasserstein auto-encoders. *arXiv:1711.01558 [stat]*, 2019.
- [164] Alireza Makhzani, Jonathon Shlens, Navdeep Jaitly, Ian Goodfellow, and Brendan Frey. Adversarial autoencoders. *arXiv:1511.05644 [cs]*, 2016.
- [165] Yuchen Pu, Weiyao Wang, Ricardo Henao, Liqun Chen, Zhe Gan, Chunyuan Li, and Lawrence Carin. Adversarial symmetric variational autoencoder. In *Advances in Neural Information Processing Systems*, pages 4330–4339, 2017.
- [166] Richard A Levine and George Casella. Implementations of the Monte Carlo EM algorithm. *Journal of Computational and Graphical Statistics*, 10(3):422–439, 2001.
- [167] Lars Mescheder, Sebastian Nowozin, and Andreas Geiger. Adversarial variational bayes: Unifying variational autoencoders and generative adversarial networks. In *Proceedings of the 34th International Conference on Machine Learning-Volume 70*, pages 2391–2400. JMLR.org, 2017.

-
- [168] Clark R Givens and Rae Michael Shortt. A class of Wasserstein metrics for probability distributions. *Michigan Mathematical Journal*, 31(2):231–240, 1984.
 - [169] V Barranco-Lopez, P Luque-Escamilla, and R Roman-Roldan. Texture Edge Detection by Using the Jenssen-Shannon Divergence. In *ISITA'94: International Symposium on Information Theory & Its Applications 1994; Proceedings: International Symposium on Information Theory & Its Applications 1994; Proceedings*, pages 1027–1030. Institution of Engineers, Australia Barton, ACT, 1994.
 - [170] Jakub Tomczak and Max Welling. VAE with a VampPrior. In *International Conference on Artificial Intelligence and Statistics*, pages 1214–1223, 2018.
 - [171] Stanislav Pidhorskyi, Ranya Almohsen, and Gianfranco Doretto. Generative probabilistic novelty detection with adversarial autoencoders. In *Advances in Neural Information Processing Systems*, pages 6822–6833, 2018.
 - [172] Bin Dai, Yu Wang, John Aston, Gang Hua, and David Wipf. Hidden talents of the variational autoencoder. *arXiv preprint arXiv:1706.05148*, 2017.
 - [173] Joao Pereira and Margarida Silveira. Unsupervised anomaly detection in energy time series data using variational recurrent autoencoders with attention. In *2018 17th IEEE International Conference on Machine Learning and Applications (ICMLA)*, pages 1275–1282. IEEE, 2018.
 - [174] Xuhong Wang, Ying Du, Shijie Lin, Ping Cui, Yuntian Shen, and Yupu Yang. adVAE: A self-adversarial variational autoencoder with Gaussian anomaly prior knowledge for anomaly detection. *Knowledge-Based Systems*, 190:105187, 2020.
 - [175] Ashish Vaswani, Noam Shazeer, Niki Parmar, Jakob Uszkoreit, Llion Jones, Aidan N Gomez, Łukasz Kaiser, and Illia Polosukhin. Attention is all you need. *Advances in neural information processing systems*, 30, 2017.
 - [176] Xiaoran Chen and Ender Konukoglu. Unsupervised Detection of Lesions in Brain MRI using constrained adversarial auto-encoders. *arXiv:1806.04972 [cs]*, 2018.
 - [177] Asimenia Dimokranitou. *Adversarial autoencoders for anomalous event detection in images*. PhD thesis, Purdue University, 2017.
 - [178] Samet Akcay, Amir Atapour-Abarghouei, and Toby P. Breckon. Gandomaly: Semi-supervised anomaly detection via adversarial training. In *Asian conference on computer vision*, pages 622–637. Springer, 2018.
 - [179] Hyojung Ahn, Dawoon Jung, and Han-Lim Choi. Deep generative models-based anomaly detection for spacecraft control systems. *Sensors*, 20:1991, 04 2020.
 - [180] Samet Akçay, Amir Atapour-Abarghouei, and Toby P Breckon. Skip-gandomaly: Skip connected and adversarially trained encoder-decoder anomaly detection. In *2019 International Joint Conference on Neural Networks (IJCNN)*, pages 1–8. IEEE, 2019.

Bibliography

- [181] Tolga Ergen and Suleyman Serdar Kozat. Unsupervised Anomaly Detection With LSTM Neural Networks. *IEEE Transactions on Neural Networks and Learning Systems*, 31(8):3127–3141, Aug 2020.
- [182] Rong Yao, Chongdang Liu, Linxuan Zhang, and Peng Peng. Unsupervised Anomaly Detection Using Variational Auto-Encoder based Feature Extraction. In *2019 IEEE International Conference on Prognostics and Health Management (ICPHM)*, pages 1–7, San Francisco, CA, USA, June 2019. IEEE.
- [183] Bin Dai and David Wipf. Diagnosing and Enhancing VAE Models. *arXiv:1903.05789 [cs]*, 2019.
- [184] Danilo Rezende and Shakir Mohamed. Variational inference with normalizing flows. In *International conference on machine learning*, pages 1530–1538. PMLR, 2015.
- [185] Durk P Kingma, Tim Salimans, Rafal Jozefowicz, Xi Chen, Ilya Sutskever, and Max Welling. Improved variational inference with inverse autoregressive flow. *Advances in neural information processing systems*, 29, 2016.
- [186] Xue-Bo Jin, Wen-Tao Gong, Jian-Lei Kong, Yu-Ting Bai, and Ting-Li Su. PFVAE: a planar flow-based variational auto-encoder prediction model for time series data. *Mathematics*, 10(4):610, 2022.
- [187] Madson L. D. Dias, César Lincoln C. Mattos, Ticiana L. C. da Silva, José Antônio F. de Macedo, and Wellington C. P. Silva. Anomaly Detection in Trajectory Data with Normalizing Flows. *arXiv:2004.05958 [cs, stat]*, April 2020.
- [188] Tomas Pevny, Vasek Smidl, Martin Trapp, Ondrej Polacek, and Tomas Oberhuber. Sum-Product-Transform Networks: Exploiting Symmetries using Invertible Transformations. *arXiv:2005.01297 [stat]*, 2020.
- [189] Marco Rudolph, Tom Wehrbein, Bodo Rosenhahn, and Bastian Wandt. Fully convolutional cross-scale-flows for image-based defect detection. In *Proceedings of the IEEE/CVF Winter Conference on Applications of Computer Vision*, pages 1088–1097, 2022.
- [190] Laurent Dinh, Jascha Sohl-Dickstein, and Samy Bengio. Density estimation using Real NVP. *arXiv:1605.08803 [cs]*, 2017.
- [191] Durk P. Kingma and Prafulla Dhariwal. Glow: Generative flow with invertible 1x1 convolutions. In *Advances in neural information processing systems*, pages 10215–10224, 2018.
- [192] George Papamakarios, Theo Pavlakou, and Iain Murray. Masked Autoregressive Flow for Density Estimation. *arXiv:1705.07057 [cs, stat]*, June 2018.
- [193] George Papamakarios, Eric Nalisnick, Danilo Jimenez Rezende, Shakir Mohamed, and Balaji Lakshminarayanan. Normalizing Flows for Probabilistic Modeling and Inference. *arXiv:1912.02762 [cs, stat]*, December 2019.

-
- [194] Ivan Kobyzev, Simon J. D. Prince, and Marcus A. Brubaker. Normalizing Flows: An Introduction and Review of Current Methods. *IEEE Transactions on Pattern Analysis and Machine Intelligence*, pages 1–1, 2020.
 - [195] Polina Kirichenko, Pavel Izmailov, and Andrew Gordon Wilson. Why Normalizing Flows Fail to Detect Out-of-Distribution Data. *arXiv:2006.08545 [stat]*, 2020.
 - [196] Madson LD Dias, César Lincoln C Mattos, Ticiana LC da Silva, José Antônio F de Macedo, and Wellington CP Silva. Anomaly detection in trajectory data with normalizing flows. In *2020 International Joint Conference on Neural Networks (IJCNN)*, pages 1–8. IEEE, 2020.
 - [197] Marco Rudolph, Bastian Wandt, and Bodo Rosenhahn. Same same but differnet: Semi-supervised defect detection with normalizing flows. In *Proceedings of the IEEE/CVF winter conference on applications of computer vision*, pages 1907–1916, 2021.
 - [198] Denis Gudovskiy, Shun Ishizaka, and Kazuki Kozuka. Cflow-ad: Real-time unsupervised anomaly detection with localization via conditional normalizing flows. In *Proceedings of the IEEE/CVF Winter Conference on Applications of Computer Vision*, pages 98–107, 2022.
 - [199] Ian Bird. Computing for the large hadron collider. *Annual Review of Nuclear and Particle Science*, 61:99–118, 2011.
 - [200] Nicholas M Ball and Robert J Brunner. Data mining and machine learning in astronomy. *International Journal of Modern Physics D*, 19(07):1049–1106, 2010.
 - [201] Norbert Holtkamp, ITER Project Team, et al. An overview of the ITER project. *Fusion Engineering and Design*, 82(5-14):427–434, 2007.
 - [202] R Panek, J Adámek, M Aftanas, P Bílková, P Böhm, F Brochard, P Cahyna, J Cavalier, R Dejarnac, M Dimitrova, et al. Status of the COMPASS Tokamak and Characterization of the First H-mode. *Plasma Physics and Controlled Fusion*, 58(1):014015, 2015.
 - [203] T Markovic, J Seidl, A Melnikov, P Haccek, J Havlicek, A Havranek, M Hron, O Hronova, M Imrisek, F Janky, et al. Alfvén-wave character oscillations in tokamak COMPASS plasma. In *Proc. 42nd EPS Conf. Plasma Physics*, pages 22–26, 2015.
 - [204] AV Melnikov, T Markovic, LG Eliseev, J Adámek, M Aftanas, P Bilkova, P Boehm, M Gryaznevich, M Imrisek, SE Lysenko, et al. Quasicoherent modes on the COMPASS tokamak. *Plasma Physics and Controlled Fusion*, 57(6):065006, 2015.
 - [205] T Markovic, A Melnikov, J Seidl, L Eliseev, J Havlicek, A Havránek, M Hron, M Imříšek, and K Kovářík. Alfvén-character oscillations in ohmic plasmas observed on the COMPASS tokamak. In *Proc. 44th EPS Conf. on Plasma Phys*, volume 5, 2017.
 - [206] RR Mett and SM Mahajan. Kinetic theory of toroidicity-induced Alfvén eigenmodes. *Physics of Fluids B: Plasma Physics*, 4(9):2885–2893, 1992.

Bibliography

- [207] Yann LeCun, Bernhard Boser, John S Denker, Donnie Henderson, Richard E Howard, Wayne Hubbard, and Lawrence D Jackel. Backpropagation applied to handwritten zip code recognition. *Neural computation*, 1(4):541–551, 1989.
- [208] Marc’Aurelio Ranzato, Christopher Poultney, Sumit Chopra, and Yann L Cun. Efficient learning of sparse representations with an energy-based model. In *Advances in neural information processing systems*, pages 1137–1144, 2007.
- [209] Manuel Fernández-Delgado, Eva Cernadas, Senén Barro, and Dinani Amorim. Do we need hundreds of classifiers to solve real world classification problems? *The journal of machine learning research*, 15(1):3133–3181, 2014.
- [210] B Ravi Kiran, Dilip Mathew Thomas, and Ranjith Parakkal. An overview of deep learning based methods for unsupervised and semi-supervised anomaly detection in videos. *Journal of Imaging*, 4(2):36, 2018.
- [211] Guansong Pang, Chunhua Shen, Longbing Cao, and Anton van den Hengel. Deep learning for anomaly detection: A review. *arXiv:2007.02500 [cs]*, 2020.
- [212] Vít Škvára, Tomáš Pevný, and Václav Šmídl. Are generative deep models for novelty detection truly better? *arXiv:1807.05027 [cs]*, 2018.
- [213] Vít Škvára, Jan Francou, Matěj Zorek, Tomáš Pevný, and Václav Šmídl. Comparison of Anomaly Detectors: Context Matters. *IEEE Transactions on Neural Networks and Learning Systems*, 2021.
- [214] James Bergstra and Yoshua Bengio. Random search for hyper-parameter optimization. *The Journal of Machine Learning Research*, 13(1):281–305, 2012.
- [215] Janez Demšar. Statistical comparisons of classifiers over multiple data sets. *Journal of Machine learning research*, 7(Jan):1–30, 2006.
- [216] Lucas Deecke, Robert Vandermeulen, Lukas Ruff, Stephan Mandt, and Marius Kloft. Image anomaly detection with generative adversarial networks. In *Joint european conference on machine learning and knowledge discovery in databases*, pages 3–17. Springer, 2018.
- [217] Diederik P Kingma and Max Welling. Auto-encoding variational bayes. *arXiv:1312.6114 [stat]*, 2014.
- [218] Raghavendra Chalapathy, Edward Toth, and Sanjay Chawla. Group Anomaly Detection using Deep Generative Models. *arXiv:1804.04876 [cs]*, April 2018.
- [219] Tomoharu Iwata and Yuki Yamanaka. Supervised Anomaly Detection based on Deep Autoregressive Density Estimators. *arXiv:1904.06034 [cs, stat]*, April 2019.
- [220] Alessio Ishizaka and Philippe Nemery. *Multi-criteria decision analysis: methods and software*. John Wiley & Sons, 2013.
- [221] Michael Gutmann and Aapo Hyvärinen. Noise-contrastive estimation: A new estimation principle for unnormalized statistical models. In *Proceedings of the thirteenth international conference on artificial intelligence and statistics*, pages 297–304. JMLR Workshop and Conference Proceedings, 2010.

-
- [222] Faruk Ahmed, Yoshua Bengio, Harm Van Seijen, and Aaron Courville. Systematic generalisation with group invariant predictions. In *International Conference on Learning Representations*, 2021.
 - [223] Orna Raz, Philip Koopman, and Mary Shaw. Semantic anomaly detection in online data sources. In *proceedings of the 24th International Conference on Software Engineering*, pages 302–312, 2002.
 - [224] Hans-Peter Kriegel, Peer Kröger, Erich Schubert, and Arthur Zimek. Outlier detection in axis-parallel subspaces of high dimensional data. In *Pacific-asia conference on knowledge discovery and data mining*, pages 831–838. Springer, 2009.
 - [225] Mostafa Rahmani and George K Atia. Randomized robust subspace recovery and outlier detection for high dimensional data matrices. *IEEE Transactions on Signal Processing*, 65(6):1580–1594, 2016.
 - [226] Christopher P Burgess, Irina Higgins, Arka Pal, Loic Matthey, Nick Watters, Guillaume Desjardins, and Alexander Lerchner. Understanding disentangling in beta-VAE. *arXiv preprint arXiv:1804.03599*, 2018.
 - [227] Hyunjik Kim and Andriy Mnih. Disentangling by factorising. In *International Conference on Machine Learning*, pages 2649–2658. PMLR, 2018.
 - [228] Babak Esmaeili, Hao Wu, Sarthak Jain, Alican Bozkurt, Narayanaswamy Sidharth, Brooks Paige, Dana H Brooks, Jennifer Dy, and Jan-Willem Meent. Structured disentangled representations. In *The 22nd International Conference on Artificial Intelligence and Statistics*, pages 2525–2534. PMLR, 2019.
 - [229] Michael Tschannen, Olivier Bachem, and Mario Lucic. Recent advances in autoencoder-based representation learning. *arXiv preprint arXiv:1812.05069*, 2018.
 - [230] Junwen Bai, Weiran Wang, and Carla P Gomes. Contrastively disentangled sequential variational autoencoder. *Advances in Neural Information Processing Systems*, 34:10105–10118, 2021.
 - [231] Minyoung Kim, Yuting Wang, Pritish Sahu, and Vladimir Pavlovic. Bayes-factorvae: Hierarchical bayesian deep auto-encoder models for factor disentanglement. In *Proceedings of the IEEE/CVF International Conference on Computer Vision*, pages 2979–2987, 2019.
 - [232] Lucas Deecke, Lukas Ruff, Robert A Vandermeulen, and Hakan Bilen. Transfer-based semantic anomaly detection. In *International Conference on Machine Learning*, pages 2546–2558. PMLR, 2021.
 - [233] Jakub M Tomczak and Max Welling. VAE with a VampPrior. *arXiv preprint arXiv:1705.07120*, 2017.
 - [234] Václav Šmíd, Jan Bím, and Tomáš Pevný. Anomaly scores for generative models. *arXiv:1905.11890 [stat]*, 2019.

Bibliography

- [235] Jaewoong Choi, Geonho Hwang, and Myungjoo Kang. Discond-VAE: disentangling continuous factors from the discrete. *arXiv preprint arXiv:2009.08039*, 2020.
- [236] Axel Sauer and Andreas Geiger. Counterfactual generative networks. *arXiv preprint arXiv:2101.06046*, 2021.
- [237] Yann LeCun, Corinna Cortes, and CJ Burges. MNIST handwritten digit database. *ATT Labs [Online]. Available: <http://yann.lecun.com/exdb/mnist>*, 2, 2010.
- [238] Mircea Cimpoi, Subhransu Maji, Iasonas Kokkinos, Sammy Mohamed, and Andrea Vedaldi. Describing textures in the wild. In *Proceedings of the IEEE conference on computer vision and pattern recognition*, pages 3606–3613, 2014.
- [239] Anders Boesen Lindbo Larsen, Søren Kaae Sønderby, Hugo Larochelle, and Ole Winther. Autoencoding beyond pixels using a learned similarity metric. In *International conference on machine learning*, pages 1558–1566. PMLR, 2016.
- [240] Justin Johnson, Alexandre Alahi, and Li Fei-Fei. Perceptual losses for real-time style transfer and super-resolution. In *European conference on computer vision*, pages 694–711. Springer, 2016.
- [241] Karen Simonyan and Andrew Zisserman. Very deep convolutional networks for large-scale image recognition. *arXiv preprint arXiv:1409.1556*, 2014.
- [242] Dong C Liu and Jorge Nocedal. On the limited memory BFGS method for large scale optimization. *Mathematical programming*, 45(1):503–528, 1989.
- [243] Janez Demšar. Statistical comparisons of classifiers over multiple data sets. *Journal of Machine learning research*, 7(Jan):1–30, 2006.
- [244] Dheeru Dua and Casey Graff. UCI machine learning repository, 2017.
- [245] Andrew F Emmott, Shubhomoy Das, Thomas Dietterich, Alan Fern, and Weng-Keen Wong. Systematic construction of anomaly detection benchmarks from real data. In *Proceedings of the ACM SIGKDD workshop on outlier detection and description*, pages 16–21. ACM, 2013.
- [246] Han Xiao, Kashif Rasul, and Roland Vollgraf. Fashion-MNIST: a Novel Image Dataset for Benchmarking Machine Learning Algorithms. *arXiv:1708.07747 [cs]*, 2017.
- [247] Yuval Netzer, Tao Wang, Adam Coates, Alessandro Bissacco, Bo Wu, and Andrew Y. Ng. Reading digits in natural images with unsupervised feature learning. In *NIPS Workshop on Deep Learning and Unsupervised Feature Learning 2011*, 2011.
- [248] Alex Krizhevsky and Geoffrey Hinton. Learning Multiple Layers of Features from Tiny Images. *University of Toronto*, 05 2012.
- [249] Norman Mu and Justin Gilmer. MNIST-C: A Robustness Benchmark for Computer Vision. *arXiv:1906.02337 [cs]*, June 2019.

- [250] Paul Bergmann, Michael Fauser, David Sattlegger, and Carsten Steger. MVTec AD—A comprehensive real-world dataset for unsupervised anomaly detection. In *Proceedings of the IEEE/CVF conference on computer vision and pattern recognition*, pages 9592–9600, 2019.
- [251] Tsung-Yi Lin, Michael Maire, Serge Belongie, James Hays, Pietro Perona, Deva Ramanan, Piotr Dollár, and C Lawrence Zitnick. Microsoft COCO: Common objects in context. In *European conference on computer vision*, pages 740–755. Springer, 2014.
- [252] Bolei Zhou, Agata Lapedriza, Aditya Khosla, Aude Oliva, and Antonio Torralba. Places: A 10 million Image Database for Scene Recognition. *IEEE Transactions on Pattern Analysis and Machine Intelligence*, 2017.
- [253] Jeff Bezanson, Alan Edelman, Stefan Karpinski, and Viral B Shah. Julia: A fresh approach to numerical computing. *SIAM Review*, 59(1):65–98, 2017.
- [254] Adam Paszke, Sam Gross, Francisco Massa, Adam Lerer, James Bradbury, Gregory Chanan, Trevor Killeen, Zeming Lin, Natalia Gimelshein, Luca Antiga, Alban Desmaison, Andreas Kopf, Edward Yang, Zachary DeVito, Martin Raison, Alykhan Tejani, Sasank Chilamkurthy, Benoit Steiner, Lu Fang, Junjie Bai, and Soumith Chintala. PyTorch: An Imperative Style, High-Performance Deep Learning Library. In *Advances in Neural Information Processing Systems 32*, pages 8024–8035. Curran Associates, Inc., 2019.